DESIGN AND ANALYIS OF BROADBAND SELF-BIASING STRUCTURES FOR MICROWAVE APPLICATIONS

by
Walter Scott Wall

A dissertation submitted to Johns Hopkins University in conformity with
the requirements for the degree of Doctor of Philosophy

Baltimore, Maryland
September, 2014

Intended to be blank

Abstract

For many high power microwave applications, it is desirable to modify the properties of radiating elements on a time-scale which is must faster than traditional active control circuits, to improve isolation and limiting. For these applications, self-biasing structures can be utilized to alter the propagation of an electromagnetic wave at microwave time-scales by dividing incident power among many high-speed nonlinear elements. These self-biasing structures have been previously implemented using nonlinear metamaterials, which consist of resonant subwavelength elements loaded with diodes. Due to the resonant nature of these structures, the bandwidth and consequently the activation time of these devices is inherently limited.

In the first part of this dissertation a nonlinear metamaterial is demonstrated which switches from a broadband reflective state at low power to a broadband transparent state at high power. Below the activation voltage, broadband reflectivity is created as a result of the effective permittivity and permeability having different signs. Above the activation voltage, reflection is suppressed by matching the relative permittivity and permeability. Both numerical simulations and experimental results are presented at S-band frequencies. To analyze the transient switching behavior of this structure a nonlinear multiconductor transmission line circuit is developed. Transient measurements of this structure conducted in WR-284 waveguide show excellent agreement with this model. Finally, this analysis is used to develop a varactor-loaded metamaterial which is capable of transitioning from a broadband transparent state at low power to a broadband reflective state at high power.

In the final chapter of this dissertation, a self-biasing switch is proposed to reduce the artifacts associated with time reversal based beamforming. This device consists of multiple diodes placed in series on a 50-Ω microstrip. At low incident voltages this device behaves like a high pass filter. Once the threshold voltage of these diodes is exceeded, the capacitive elements of this filter are shorted allowing energy to pass with significantly less attenuation. By preferentially attenuating low power transients this device can suppress the temporal artifacts associated with the time reversal process. An experimental demonstration of this device is performed using a reverberant cavity as a passive delay line network. Measured outputs from this cavity are used as inputs to a simulated array of Vivaldi antennas to demonstrate the proposed improvement in beamforming.

Primary Reader: Prof. Mark A. Foster

Secondary Reader: Prof. Jacob B. Khurgin

Acknowledgments

Foremost I would like to thank my friends and colleagues Dr. Scott Rudolph and Dr. Sun Hong for bringing the work presented in this dissertation to fruition. Without your help, I would not have been able to accomplish this major milestone in my life. Thank you for going above and beyond to give me the technical guidance I needed to do this research and the support I needed to not give up. In addition I would also like to thank a few of my many coworkers at the NRL, Kenny Morgan, Victor Mendez, and Tony Warren, as well as my supervisor Dr. Tim Andreadis and my Branch Head Mike Monsma. I would also like to thank the Office of Naval Research for providing the financial support required to carry out this work.

I would like to thank my advisor Prof. Mark Foster for guiding me through this process and showing me how to conduct high quality research. I would also like to acknowledge my dissertation committee members, Prof. Jacob B. Khurgin and Prof. Amy Foster for providing high caliber comments and feedback on this work, and my GBO committee Prof. James B. Spice, Prof. Peter Armitage, Prof. Alexander Kaplan, and Prof. Ted Poehler.

Finally I would like to thank my mother and family as well as my friends for supporting me through this process and giving me the encouragement I needed every step along the way.

Contents

List of Tables

List of Figures

Chapter 1 -Introduction

Microwave frequencies, which cover the portion of the electromagnetic spectrum from 300 MHz – 300 GHz [1], shape many aspects of the modern human experience. Wireless communication networks use these waves to transmit and receive data over large distances [2]. Due to the advent of high speed integrated processors, these networks now allow access to information from all over the world, revolutionizing the way in which people and societies interact with one another. Medical technologies such as MRI [3] employ electromagnetic frequencies just below the microwave regime to aid in the detection of disease and injury, increasing both the quality and duration of human life. Furthermore emerging techniques such as microwave thermotherapy [4] may even allow this same frequency range to target and destroy cancerous cells without invasive surgical procedures. Radars, which now operate throughout the microwave frequency range, have enabled humans to detect and image objects over vast distances [5]. This capability has allowed us to not only study remote parts of our planet but also view new and exotic worlds outside our own [6, 7]. Microwaves have even challenged our most fundamental views as a species, granting new and powerful insights into the dynamics of the universe through radio astronomy [8].

Composite Media

The ubiquitous nature of microwave frequencies in modern life and technology can largely be attributed to the way in which these waves interact with materials. Interactions of an electromagnetic wave with matter can primarily be characterized as electric or magnetic. For many materials, interactions with the magnetic portion of an incident wave are weak [9]. When an electric field is incident on a material, this interaction creates an induced polarization in the material which is characterized by the polarization vector field $\bar{P}$ [10]. Due to this polarization the total electric field inside a medium is the sum of the applied electric field $\bar{E}$ and the induced field due to the polarization. Therefore a quantity known as the electric displacement vector field $\bar{D}$ is used to describe this in situ field,

$$\boldsymbol{\bar{D}} = \boldsymbol{\varepsilon_0 \bar{E}} + \boldsymbol{\bar{P}} \tag{1.1}$$

where ε_0 is the permittivity of vacuum. Interactions with an applied magnetic field $\bar{H}$ are specified in a similar manner through the magnetization vector field $\bar{M}$, magnetic flux density $\bar{B}$, and the permeability of vacuum μ_0.

$$\boldsymbol{\bar{B}} = \boldsymbol{\mu_0}(\boldsymbol{\bar{H}} + \boldsymbol{\bar{M}}) \tag{1.2}$$

For linear, lossless, and isotropic media the electric displacement and magnetic flux density are directly proportional to their respective applied fields,

$$\boldsymbol{\bar{D}} = \boldsymbol{\varepsilon \bar{E}} \tag{1.3}$$

$$\boldsymbol{\bar{B}} = \boldsymbol{\mu \bar{H}} \tag{1.4}$$

where μ is defined as the permeability of the medium and ε is the permittivity of the medium.

For homogeneous media ε is due to interactions of the applied electric field with atoms and molecules. Due to the complexity which exists at the atomic level, there are a variety of mechanisms by which these interactions can give rise to observed permittivity values. In the microwave regime one of the primary mechanism by which an electric field interacts with a homogeneous media occurs through dipolar interactions [11]. These interactions are characterized by a time constant known as the relaxation time τ [10] which is related to the polarizability of the medium, α_d

$$\boldsymbol{\alpha_d = \frac{\alpha_0}{1+j\omega\tau} + C} \tag{1.5}$$

where C is the polarizability of the medium at asymptotically large frequencies. The permittivity of such media can be written in a complex form

$$\boldsymbol{\varepsilon = \varepsilon' - j\varepsilon'' = \varepsilon' - j\frac{\sigma}{\omega}} \tag{1.6}$$

where ε' is generally referred to as the dielectric constant of the medium and ε" is considered a measure of the dielectric losses. The imaginary portion of the permittivity can also be written in terms of the conductivity of the medium (σ). Both the real and imaginary components of this complex permittivity can be written in terms of the relaxation time τ,

$$\boldsymbol{\varepsilon' = \frac{\varepsilon_0-\varepsilon_\infty}{1+\omega^2\tau^2} + \varepsilon_\infty} \tag{1.7}$$

$$\boldsymbol{\varepsilon'' = \frac{(\varepsilon_0-\varepsilon_\infty)\omega\tau}{1+\omega^2\tau^2}} \tag{1.8}$$

where ε_0 and ε_∞ are the permittivity of the medium at asymptotically small and large values respectively. Media with relaxation times much larger than the period of the applied field are considered to be good insulators. Examples of insulators at microwave frequencies include many plastics and crystals. Those materials with very small relaxation times are considered good conductors such as copper and silver.

Metamaterials

Often the efficiency of a microwave device is dependent on the values of permittivity and permeability which can be realized for conductors and insulators. Due to the manner in which atoms and molecules are naturally arranged at the microscopic level desired values of ε or μ are often difficult to obtain simply by modifying the chemical composition of a material. This limitation can be overcome by creating composite materials which utilize a mixture of two different substances to achieve effective permittivity and permeability values which are distinct from either material in isolation. In 1892, Lord Rayleigh suggested that a periodic array of small spherical particles (smaller than the incident wavelength), could be used to create effective material properties due to interactions similar to those occurring at the atomic level [12]. This work was later demonstrated by W. E. Kock [13] who used a periodic array of small metal spheres to create a composite dielectric lens for microwave frequencies. When exposed to an applied electric field, alternating currents are induced on each sphere in this lattice, generating local dipoles which are similar to those induced at the atomic level. By engineering the elements and assembly of this lattice, the effective permittivity of this structure can be designed on a macroscopic scale.

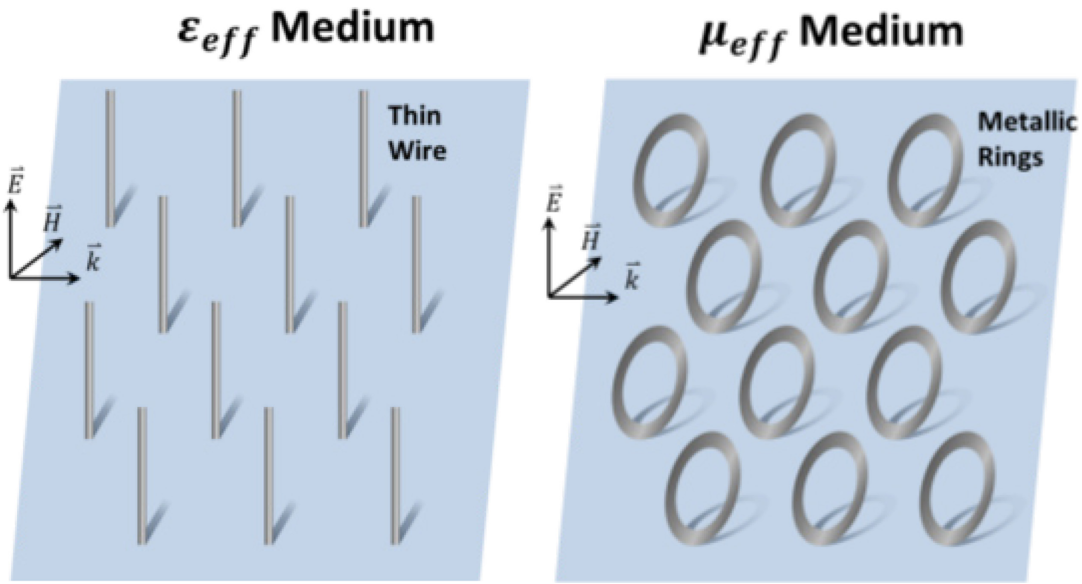

Figure 1.1- Cartoon depiction of a single layer of a thin wire medium typically used to create effective permittivity (left) and a ring structure typically used to create effective permeability (right).

This concept of creating bulk material properties on a macroscopic scale is a powerful tool in microwave engineering because it allows effective material properties to be created which are beyond those achievable in nature. For this reason, these structures are often referred to as metamaterials, borrowing from the Greek word for beyond, "μετα" or "meta". In general these metamaterials consist of subwavelength elements (i.e. unit cells), which are designed to interact with either the incident electric or magnetic field (Fig. 1.1). Unlike photonic crystals and electromagnetic band gap materials which utilize a Bragg resonance causing their unit cells to be greater than λ/2, metamaterials typically have unit cells smaller than λ/10. Typical magnetic elements for these structures consist of metallic loops. When under the influence of an applied magnetic field these loops experience an induced current which in turn creates an induced magnetization. This net magnetization creates a local magnetic field which adds to the applied one, thus modifying the effective permeability of the structure. Electric elements

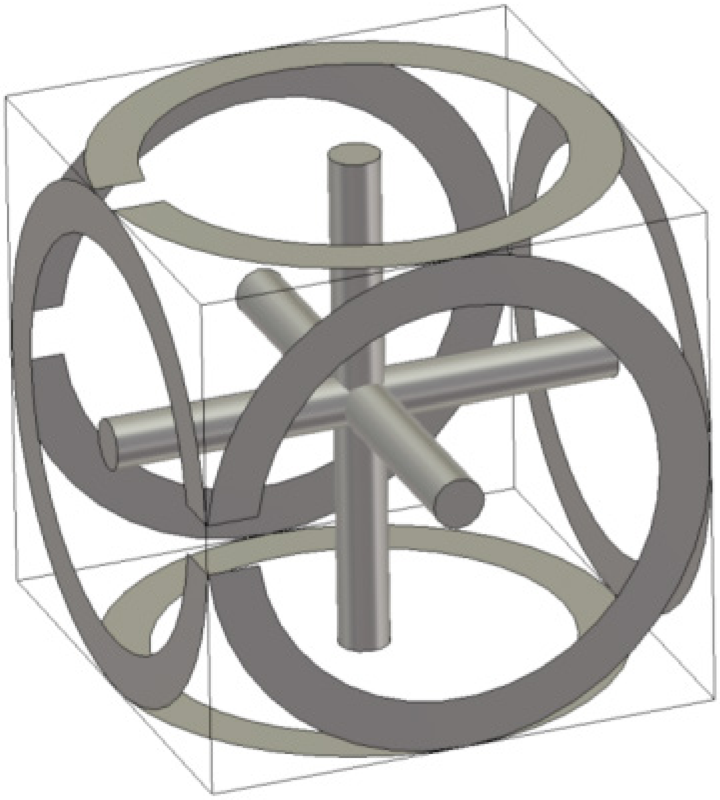

Figure 1.2-Computer rendering of a single isotropic metamaterial unit cell composed of ring resonators and thin wires.

are typically formed by thin wires, which like the spherical particles first demonstrated by Kock [13], become polarized when exposed to an incident electric field thus modifying the effective permittivity of the medium.

A typical configuration of these magnetic and electric elements in an isotropic unit cell is shown in Fig. 1.2. When oriented in a regular closely spaced lattice as shown in Figure 1.1, thin wire elements can be shown to exhibit a frequency dependent response similar to an electric plasma and following the well-known Drude model [14, 15],

$$\boldsymbol{\varepsilon_{eff} = \varepsilon_0 \left(1 - \frac{\omega_p{}^2}{\omega^2 + i\omega\Gamma}\right)} \tag{1.9}$$

where ω_p is known as the electric plasma frequency and Γ is a loss term corresponding to the inverse of the effective relaxation time (τ_{eff}) of the thin wire medium. For incident radiation with a frequency (ω) greater than the electric plasma frequency the effective permittivity of the medium is negative. Negative permeability can also be generated in this structure by introducing small gaps into the magnetic loops. The gaps in these split ring resonators (SRR) act as capacitive elements whereas the curved geometry of the loop creates inductance (Fig. 1.3). The combination of this capacitance and inductance creates an LC resonance which significantly increases the magnetization of the loop over a narrow bandwidth and modifies the effective permeability [16, 17]

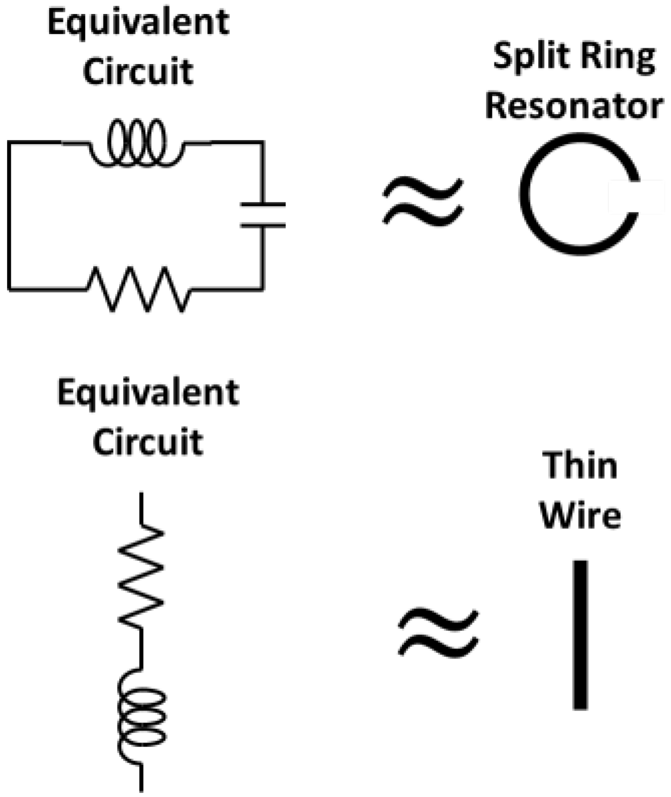

Figure 1.3- Circuit analog (left) and drawing (right) for magnetically coupled split ring resonator (top) and electrically coupled thin wire (wire).

$$\mu_{eff} = \mu_0 \left(1 - \frac{F\omega^2}{\omega^2 - {\omega_0}^2 + i\omega\Gamma}\right) \tag{1.10}$$

where F and Γ are the fill and dissipation factors respectively as specified by Smith et. al [16]. When the loss in the SRR is minimal, the effective permeability of the structure will be negative for a range of frequencies above the resonant frequency of the ring. In a pivotal paper Smith et. al. [16] demonstrated that by tuning the geometry of a unit cell similar to that shown in Fig. 1.2, a structure could be created which possessed simultaneously negative permittivity and permeability, thus allowing for negative refraction, a phenomenon previously thought to not exist in nature [18]. This demonstration successfully highlighted the potential of composite media to create new and exciting physical phenomena and thus largely popularized the field of metamaterials.

Since the work of Pendry and Smith in negative refractive index (NRI) media, the field of metamaterials has expanded into many new and exciting directions. Due to the negative effective refractive index created in these structures, the effective propagation constant through the media can also be negative allowing the effects of diffraction to effectively be “undone”. As first proposed by Veselago [19] and later expanded upon by Pendry [20], this unnatural property allows the evanescent modes of a source to be apparently amplified and transmitted to a remote image plane [21]. This phenomenon has been utilized by several authors to create sub-diffraction limited focusing which goes beyond the physical limit of traditional lenses [22]. Furthermore, because these structures can be used to engineer not only the direction but also the value of the propagation constant in the medium, several authors have demonstrated through a framework known as transformation electromagnetics, the ability of metamaterials to divert incident radiation and hide the aberrations of a known scatter effectively "cloaking" an object [23]. The exciting possibilities of these demonstration, have spurred the development of metamaterials far beyond the microwave regime into THz [24] and optical frequencies [25] and even into acoustics [26].

Tunable Metamaterials

One of the primary limitations of many metamaterial designs is the limited bandwidth over which desired effective material paramaters can be realized. In general, this limitation arises from the resonant elements loading the structure, which by nature respond most significantly over a fairly narrow bandwidth, determined by the quality factor of the resonator. Furthermore many applications demand material properties which are agile and can be changed depending on the situation. To address these issues, tunable metamaterials can be employed, which enable the effective material properties of the medium to be modified in response to some stimulus. Following the delineation outlined by Turpin et. al [27]., three basic categories of tuning mechanisms can be identified: material, geometry, and circuit. Material based methods of tuning generally attempt to modify the constituent material properties of the structure to induce a shift in the resonant characteristics of the unit cell. This effect can be achieved by modifying either the permittivity or permeability of the support material in the unit cell or by changing the conductivity of the resonant elements. Permittivity tuning has been demonstrated using a variety of materials including ferroelectric films [28], liquid-crystal [29] and phase-change materials [30], whereas permeability tuning has been achieved using ferrite materials and yttrium iron garnet [31]. Conductivity tuning is typically implemented using semiconductors [32].

A more complex yet potentially more drastic method of tuning the effective material properties of a metamaterial involves modifying the physical geometry of the unit cell. While this technique can often be challenging to implement due to the presence of actuated moving parts, it can be an effective mechanism for altering permittivity and permeability values at higher frequencies where biasing and surface mount components are not practical. At THz frequencies demonstrations of geometry tuning have been performed by modifying both the position [33] and orientation [34] of resonators and conductors within the unit cell. At optical frequencies gold nanorods [35] have been employed to modify the effective permittivity of an optical medium. Movement of the nanorods can occur either by self-assembly initiated by a local electric field or by movement of liquid crystals within the support material [36].

By far the most common method of tuning the effective material properties of a metamaterial in the microwave regime involves modifying the impedance or circuit parameters of the unit cell. This technique relies on the fact that both the magnetic and electric elements can be represented as equivalent circuits (Fig. 1.3). By inserting discrete elements into the unit cell of the metamaterial which can vary their impedance in response to an applied stimulus the frequency dependent impedance characteristics of the this equivalent circuit can be modified thus tuning the effective permittivity and permeability of the structure. This effect has been implemented through a variety of semiconductor mechanisms including varactor [37], PIN [38, 39], and Schottky [40, 41, 42] diodes as well as transistors [43]. MEMS devices have also been utilized in a similar fashion to implement a physical switch “On/Off” switch within the unit cell [33].

Self-Biasing Metamaterials

For many applications, such as high power limiting [38], field confinement [39], and harmonic generation [37], these tunable metamaterial structures need to change their material properties at a rate which is faster than traditional control circuits or respond in real-time to the incident wave. In these scenarios, actively controlled tuning mechanisms are not suitable and techniques for passively tuning the effective material properties are required. This passive modification of the effective material parameters can be achieved by inserting semiconductor devices into the electric or magnetic elements of the metamaterial structure such that the voltage induced in these elements nonlinearly modifies the impedance thus changing the resonant properties of the structure [38] [40]. One notable exception to these semiconductor based nonlinear switching mechanisms are the superconducting metamaterials [44].

In general semiconductor based self-biasing metamaterials can be divided into two classes, capacitively switched and resistively switched devices. Consider the SRR equivalent circuit shown in Fig. 3. This circuit consists of an inductive element which arises from the circular geometry of the SRR, a resistive element due to ohmic losses in the metal and support material, and a capacitor which for a single SRR is due to the gap in the ring (for the double SRR configuration this capacitance is primarily derived from the gap between the inner and outer ring [17]). When a semiconductor device is placed into the gap of the SRR, this device in effect becomes a load in parallel with the gap capacitance (Fig. 1.3). If the impedance of this load is much larger than that of the gap then the effect of this device will be negligible, otherwise the semiconductor impedance will dominate the gap capacitance and become the primary driver of resonant properties in the SRR. For resistively switched devices, the real part of this impedance generally transitions from large to small values as the voltage across the device increases, thus transitioning the loaded gap in the SRR from an open to a short. This effect reduces the quality factor of the SRR resonance without changing the resonant frequency. On the other hand capacitively switched devices generally transition from low to high impedance with increasing reverse biased voltage and because the real part of the impedance is generally constant, this change in impedance shifts the resonant frequency of the SRR without increasing loss. Thus we can modify the resonant properties of the metamaterial in two distinct ways depending on whether we load the structure with resistive or capacitive nonlinearites.

Resistive Switching

For the purpose of self-biasing the effective material properties of a metamaterial structure, resistive nonlinearities are typically achieved by using the forward bias properties of a semiconductor junction. Depending on the nature of this junction the manner in which this nonlinear resistance manifests itself can be quite varied in response to an incident change in voltage. For this reason it is critical to understand the behavior of these junctions in order to fully characterize their impact on the effective material properties of a metamaterial. In the proceeding sections, the theory associated with three common semiconductor devices (PN, PIN, and Schottky diodes) used in self-biasing

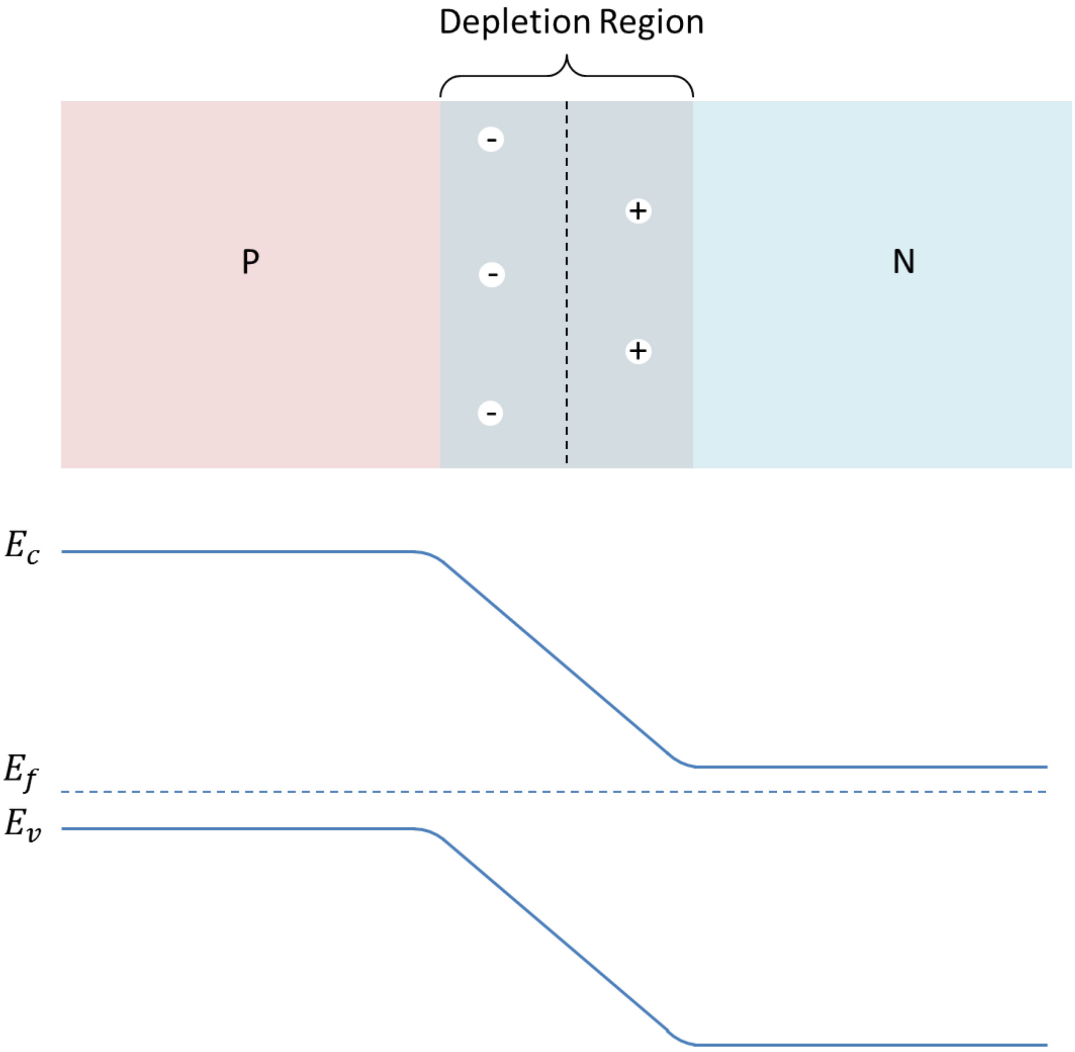

Figure 1.4- Illustration of PN junction at zero bias with the associated energy band diagram, where $\boldsymbol{E_c}$ and $\boldsymbol{E_v}$ are the energy of the conduction and valence band respectively and $\boldsymbol{E_f}$ is the Fermi energy.

metamaterials will be outlined to illuminate the voltage dependent impedance properties of these devices. Specific examples from literature of their implementation will also be provided where appropriate.

PN-Junction Diode

One of the most commonly employed semiconductor devices is the PN junction diode [45]. This device consists of P-type and N-type semiconductors in physical contact (Fig. 1.4). At this junction "holes" in the valence band of the P-type semiconductor diffuse into the N-type material and electrons in the conduction band of the N-type diffuse into the P-type material. As electrons vacate the N-type region, they leave behind ionized donor atoms which are bound to the crystal lattice. These ionized atoms create a net force on the electrons which is balanced by diffusive forces, thus creating an equilibrium region known as the depletion region. A similar effect occurs with the holes leaving the P-type region creating a second depletion region in the P-type material. This redistribution of charges within the depletion region creates a net potential which is known as the junction potential of the diode and prevents further diffusion in the semiconductor junction. If an external bias voltage is applied to this junction such that it opposes the junction potential than the potential across the depletion region will be lower than its equilibrium value thus allowing charges to diffuse and current to flow across the junction. This condition is known as forward bias and is can be described by the ideal diode equation,

$$\mathbf{I} = \mathbf{I_s}\left(\mathbf{e}^{\left(\frac{\mathbf{eV}}{\mathbf{kT}}\right)} - \mathbf{1}\right) \tag{1.11}$$

where I_s is the saturation current, e is the electronic charge, V is applied voltage, k is Boltzman's constant, and T is the temperature of the junction. However, if on the other hand a bias is applied in the same direction as the equilibrium then the junction potential will be increased beyond its equilibrium value and diffusion of charge carriers will be reduced. This process generates some current in the junction but it is small due to the fact that it is supported by minority carriers. Therefore there is a non-reciprocal and nonlinear current voltage relationship present in a PN semiconductor junction.

PIN-Junction Diode

A simple yet powerful modification which can be made to the PN junction is the addition of a lightly doped semiconductor region in between the P-type and N-type regions, known as the "intrinsic region" hence these junctions are known as PIN diode (Fig 1.5). Charges from the P-type and N-type regions diffuse into this intrinsic layer and recombine leaving thin charged regions on either side of the intrinsic later [46]. Unlike the PN junction, the electric field created by these two separated charge regions is uniform throughout the intrinsic layer. By adjusting the width of this of this intrinsic region the breakdown voltage of these diodes can be increased. This property makes them ideal candidates for high power RF limiting circuits.

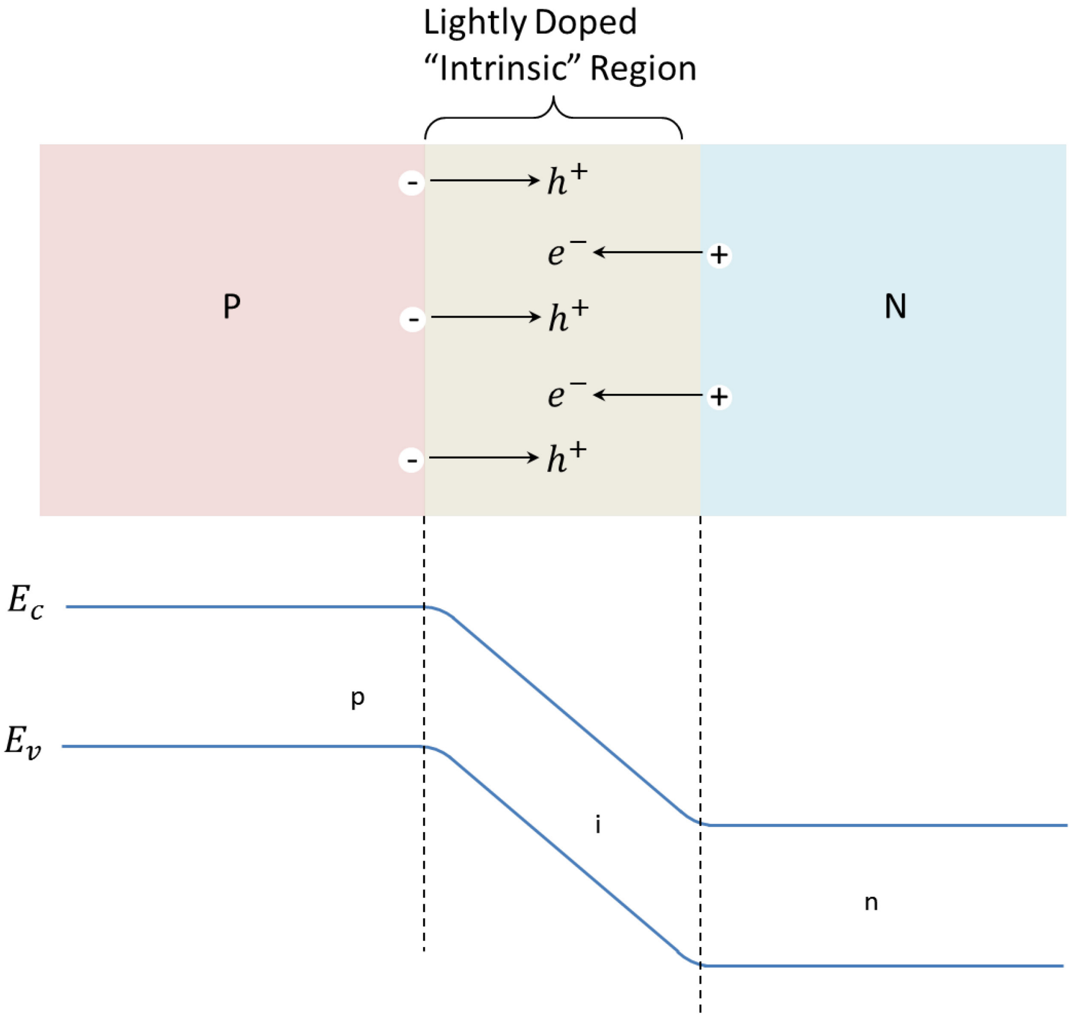

Figure 1.5- Illustration of PIN junction at zero bias with the associated energy band diagram.

Due to their unique high power and frequency capabilities, PIN diodes have been successfully employed in various self-biasing metamaterial demonstrations. Katko et. al. [38] were the first to utilize high speed PIN diodes to passively switch the effective material parameters of a metamaterial structure under the influence of a high power RF wave. In this demonstration a complementary electrically coupled split ring resonator structure was loaded with PIN diodes and used to demonstrate microwave limiting at S-band frequencies. A 3-dB reduction in transmitted amplitude was observed over an 18%

bandwidth centered in S-band frequency range with a maximum change in transmission of 6 dB. Following this work, Lopez et. al. [39], utilized a PIN diode loaded split ring resonator array to improve the signal to noise ratio of an MRI coil. This was done by creating a metamaterial structure which possessed an effective permeability close to one for low incident power levels. Once exposed to high power the effective permeability of this structure decreased significantly to something close to zero, thus rejecting fields at high power and allowing the SNR of the system to be increased.

Schottky Diode

One of the primary issues associated with both PN and PIN junctions for RF applications is the so-called reverse recovery time. As these junctions become forward biased, minority carriers are stored both in the depletion region and the adjacent charge neutral regions [45]. For time varying RF signals which both forward and reverse bias these junctions, these stored charges can be problematic as they allow current to flow in reverse bias. A quantity known as the transient time is used to describe this effect and

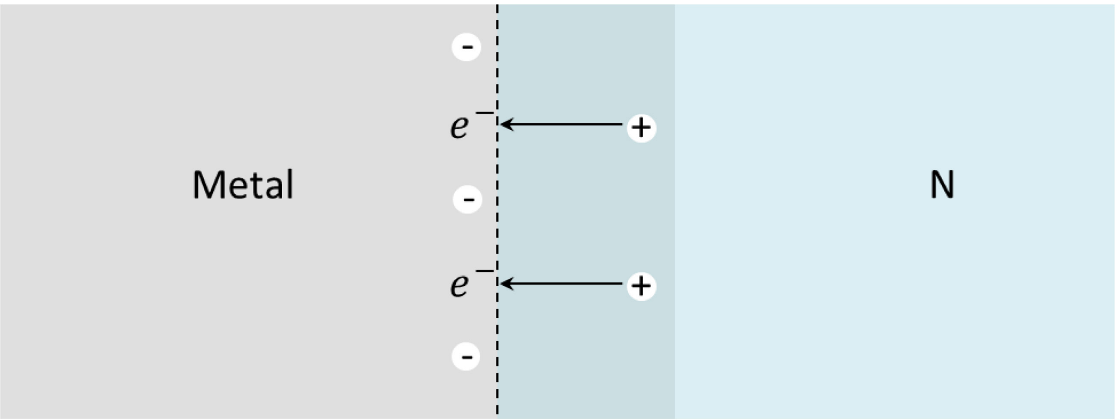

Figure 1.6- Illustration of Schottky barrier junction at zero bias.

corresponds to the time required for the junction current to drop to 10% of the initial reverse current [46]. For efficient operation this transient time needs to be significantly less than any transient applied to the diode. In the case of PN junction diodes, the transient time can be quite high limiting the operation of these diodes at microwave frequencies. For high frequency applications Schottky barrier diodes are often used instead of PN diodes. These Schottky diodes typically consist of an N-type semiconductor bonded to a metal [45] (Fig. 1.6). When in contact with a perfectly conducting metal, electrons from the N-type region are transferred into the metal, leaving behind a region of positively charged donor impurity atoms. A negatively charged sheet forms at the surface of the metal to balance this positively charged region, which suppresses the flow of electrons and causes the system to reach equilibrium. This distribution of charges forms a potential barrier, which like the PN and PIN diodes can be overcome with sufficient forward biasing. However unlike these diodes, conduction occurs through majority carriers, which limits the switching time of the junction by the thermalization of hot carriers and not the recombination time. This decreased recovery time allows Schottky diodes to function at significantly higher frequency ranges.

Due to their low activation voltage and transient times, Schottky diodes have been employed in various self-biasing metamaterial applications. One of the first such demonstrations was performed by Sievenpiper et. al. [41] using a ground metasurface. In this demonstration high-speed Schottky diodes were used to connect the metal patches of the so-called “mushroom” or “Sievenpiper” surface. At low power these diodes act like high impedance devices and allow a surface mode to propagate along the structure. Once activated at high power the diodes become lossy absorbing incident energy and preventing the flow of current along the structure protecting sensitive electronics from damage. This work was later extended to create waveform selective absorbers which selectively attenuate depending on the pulsewidth of the incident waveform [42]. More recently a broadband nonlinear switching metamaterial structure was demonstrated by Wall et. al. [40], using a traveling metamaterial structure loaded with high speed Schottky diodes.

Capacitive Switching

For many applications such as harmonic generation and tunable filtering [37] the resonant frequency of a metamaterial structure needs to shift in frequency in response to a change in incident power. In these cases, the magnetic and/or electric elements of the structure are loaded with capacitive nonlinearities instead of the resistive nonlinearities previously discussed. Because these nonlinearities primarily modify the reactive part of the impedance, the transition from the material properties at low power to those at high power is not necessarily marked by Ohmic losses as is the case with resistive switching.

Varactor Diode

For most microwave applications nonlinear capacitance is achieved through the use of varactor diodes. Under reverse bias, the junction potential of these diodes is increased causing the width of the depletion region to grow (Fig. 1.7). This effect decreases the capacitance thus creating a capacitance which is described by an inverse relationship with the applied voltage

Figure 1.7- Illustration of varactor effect in PN junction.

$$\boldsymbol{C(V)} = \boldsymbol{C_0}\left(\frac{\mathbf{1}}{\mathbf{1}-\frac{\boldsymbol{V}}{\boldsymbol{V_j}}}\right)^{\boldsymbol{M}}, \qquad -\infty < V < 0 \tag{1.12}$$

where C_0 is the zero-bias capacitance, M is grading coefficient, and V_j is the junction potential [47]. For an ideal varactor the grading coefficient has a value close 0.5, but with specific doping profiles this value can be increased significantly which is the case for hyperabrupt varactors [48]. These hyperabrupt diodes are capable of significantly more abrupt changes in capacitance in response to applied voltage and thus can behave more nonlinear over certain tuning ranges.

Due to their unique reactive tuning properties, varactor diodes have been successfully utilized in nonlinear and self-biasing metamaterial structures. Initial demonstrations of varactor loaded metamaterial structures utilized split resonators loaded with hyperabrupt varactor diodes to create tunable resonances and high order harmonics [37]. Later work demonstrated that these resonances exhibited bistable properties [49, 50] which resulted in abrupt changes in effective material parameters. Furthermore in the case where two opposing varactor diodes were used to load the resonant elements of the metamaterial significant hysteric effects were observed.

Chapter 2 –Imaginary Impedance Metamaterials

Metamaterials have the ability to engineer not only the magnitude of permittivity and permeability values but also the sign of these quantities. Over the past decade, this feature has been the subject of much research: often focused on the development of simultaneously negative permittivity and permeability media. However the ability to create non-overlapping spectral regions of negative permittivity and permeability can also be of great utility. As will be discussed in this chapter, such effective permittivity and permeability combinations create media with imaginary impedance or refractive index. Materials with imaginary refractive indices are generally strong reflectors of electromagnetic energy such as metals. However, unlike naturally occurring reflective media, the characteristics of a metamaterial can effectively be switched on or off depending on the power in an incident wave. This effect can be achieved through the insertion of resistive or capacitive switching mechanisms, such as those discussed in Chapter 1. In this chapter the transmission of electromagnetic waves through imaginary impedance media will be discussed as well as a metamaterial structure for achieving such material properties.

Imaginary Impedance Media

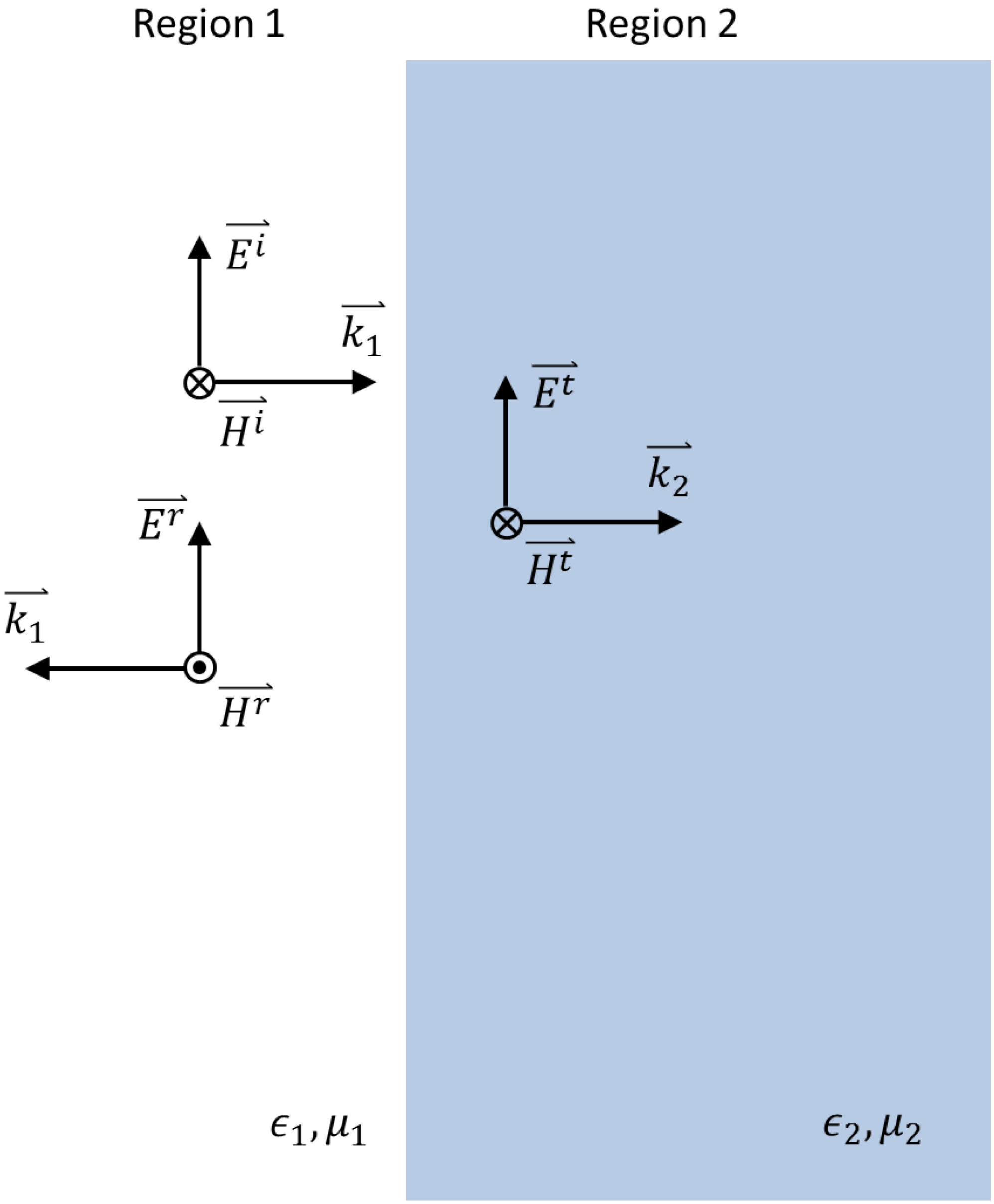

Figure 2.1- Illustration showing field orientation for incident, reflected, and transmitted waves at the boundary between two dielectric media.

Consider a plane electromagnetic wave propagating in a purely real dielectric medium. Following the analysis in [51], solutions for the electric and magnetic fields of this wave can be written in the following phasor notation

$$\vec{\boldsymbol{E}} = \boldsymbol{E} e^{-jkz} \hat{\boldsymbol{x}} \tag{2.1}$$

$$\vec{H} = He^{-jkz}\hat{y} \tag{2.2}$$

where k is the propagation constant in the medium specified as $k = \omega\sqrt{\varepsilon\mu}/c$. The orientation of the Cartesian coordinates x,y, and z are shown in Fig. 2.1. Substituting $H = E/Z$ into Eq. 2.2, where Z is the characteristic impedance of the medium defined as $Z = \sqrt{\mu/\varepsilon}$, the magnetic field vector can be written in terms of the electric field magnitude.

$$\vec{H} = \frac{E}{Z}e^{-jkz}\hat{y} \tag{2.3}$$

When this propagating wave encounters the boundary of a dissimilar medium having infinite extent in both the transverse (i.e. $\hat{x}\&\hat{y}$) and longitudinal (i.e. $\hat{z}$) directions the solutions at the boundary can be decomposed into 3 distinct waves: an incident wave, a reflected wave, and a transmitted wave (Fig 2.1)

$$\vec{E^i} = E_1^i e^{-jk_1z}\hat{x} \tag{2.4}$$

$$\vec{E^r} = E_1^r e^{jk_1z}\hat{x} \tag{2.5}$$

$$\vec{E^t} = E_2 e^{-jk_2z}\hat{x} \tag{2.6}$$

$$\vec{H^i} = \frac{E_1^i}{Z_1}e^{-jk_1z}\hat{y} \tag{2.7}$$

$$\vec{H^r} = -\frac{E_1^r}{Z_1}e^{jk_1z}\hat{y} \tag{2.8}$$

$$\vec{H^t} = \frac{E_2}{Z_2}e^{-jk_2z}\hat{y} \tag{2.9}$$

Assuming negligible surface current, Gauss' Law and Ampere's Law specify continuity of the tangential magnetic and electric fields across the boundary. Substituting Eqs 2.4-2.9 into these boundary conditions the incident and reflected waves can be related to the transmitted wave.

$$\frac{\boldsymbol{E}_1^i}{\boldsymbol{Z}_1} - \frac{\boldsymbol{E}_1^r}{\boldsymbol{Z}_1} = \frac{\boldsymbol{E}_2}{\boldsymbol{Z}_2} \tag{2.10}$$

$$\boldsymbol{E}_1^i + \boldsymbol{E}_1^r = \boldsymbol{E}_2 \tag{2.11}$$

From these equations, the reflected field in medium 1 and the transmitted field in medium 2 can be normalized to the incident field, thus yielding the reflection (r) and transmission (t) coefficients.

$$\boldsymbol{r} = \frac{\boldsymbol{E}_1^r}{\boldsymbol{E}_1^i} = \frac{\boldsymbol{Z}_2 - \boldsymbol{Z}_1}{\boldsymbol{Z}_2 + \boldsymbol{Z}_1} \tag{2.12}$$

$$\boldsymbol{t} = \frac{\boldsymbol{E}_2}{\boldsymbol{E}_1^i} = \frac{2\boldsymbol{Z}_2}{\boldsymbol{Z}_2 + \boldsymbol{Z}_1} \tag{2.13}$$

Consider the case where the impedance of medium 2 is purely imaginary and the impedance of medium 1 is purely real, which occurs when the permittivity is negative and the permeability is positive or vice versa. In this scenario the impedance of medium 2 can be written as a purely real quantity times the imaginary unit, j, yielding the following equation for the reflection coefficient.

$$\boldsymbol{r} = \frac{\boldsymbol{E}_1^r}{\boldsymbol{E}_1^i} = \frac{\boldsymbol{j}|\boldsymbol{Z}_2| - \boldsymbol{Z}_1}{\boldsymbol{j}|\boldsymbol{Z}_2| + \boldsymbol{Z}_1} \tag{2.14}$$

Rewriting the reflection coefficient as a function of reflected and incident power, it can be seen that all of the power incident on medium 2 is reflected back into medium 1.

$$\boldsymbol{R = |r|^2 = rr^* = \frac{j|Z_2|-Z_1}{j|Z_2|+Z_1} \cdot \frac{-j|Z_2|-Z_1}{-j|Z_2|+Z_1} = 1} \tag{2.15}$$

Since this medium is lossless conservation of energy guarantees that no power is transferred to medium 2 regardless of the magnitude of the impedance in either medium. In the case where this medium does have some loss or conductivity there is a finite penetration into the medium known as the skin depth effect.

Finite Imaginary Slab

For a medium possessing purely imaginary impedance the propagation constant in the medium is also imaginary. Therefore if this imaginary propagation constant is substituted into Eqs. 2.6 and 2.9, it can be seen that the fields inside the imaginary-impedance medium are not propagating but rather decay exponentially.

$$\boldsymbol{\overrightarrow{E^t} = E_2 e^{-|k_2|z} \hat{x}} \tag{2.16}$$

$$\boldsymbol{\overrightarrow{H^t} = \frac{E_2}{Z_2} e^{-|k_2|z} \hat{y}} \tag{2.17}$$

These non-propagating waves are known as evanescent fields and if the thickness of the medium is small enough these fields can penetrate through the medium creating propagating waves on the other side.

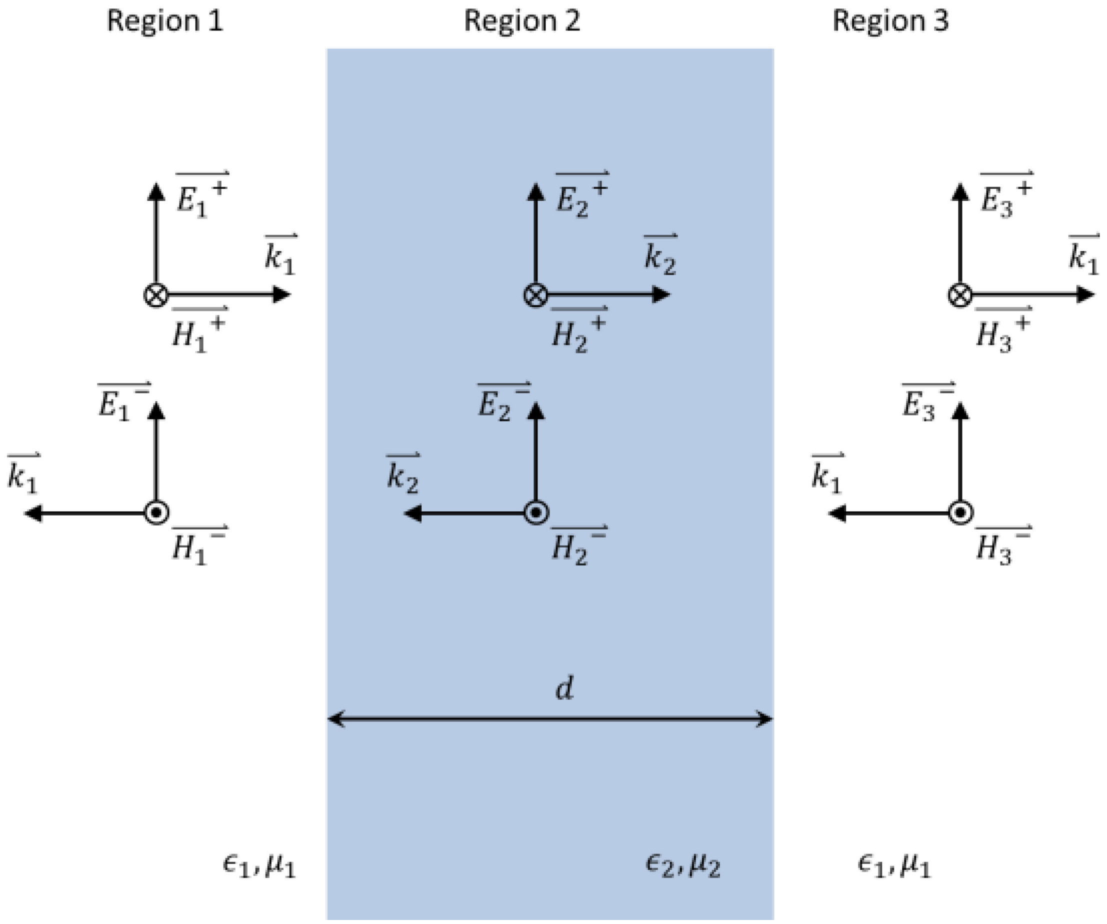

Figure 2.2- Illustration showing fields orientations inside and outside a dielectric slab of finite thickness d.

To analyze this problem consider a plane normally incident on a purely imaginary dielectric medium of finite thickness, d, in the axial direction but infinite extent in the transverse direction (Fig. 2.2). This problem can be divided into three distinct regions: before (region 1) and after (region 3) the imaginary slab and inside the slab (region 2). Following the matrix propagation method outlined in Orfanidis [52], the forward E_+^3 and backward E_-^3 propagating fields in region 3 can be written in terms of the forward E_+^1 and backward E_-^1 propagating fields in region 1,

$$\begin{pmatrix} E_1^+ \\ E_1^- \end{pmatrix} = \frac{1}{t_1}\begin{pmatrix} 1 & r_1 \\ r_1 & 1 \end{pmatrix}\begin{pmatrix} e^{jk_2d} & 0 \\ 0 & e^{-jk_2d} \end{pmatrix}\frac{1}{t_2}\begin{pmatrix} 1 & r_2 \\ r_2 & 1 \end{pmatrix}\begin{pmatrix} E_3^+ \\ E_3^- \end{pmatrix} \tag{2.18}$$

$$\begin{pmatrix} E_1^+ \\ E_1^- \end{pmatrix} = \frac{1}{t_1t_2}\begin{pmatrix} e^{jk_2d} + r_1r_2e^{-jk_2d} & r_1e^{-jk_2d} + r_2e^{jk_2d} \\ r_2e^{-jk_2d} + r_1e^{jk_2d} & e^{-jk_2d} + r_1r_2e^{jk_2d} \end{pmatrix}\begin{pmatrix} E_3^+ \\ E_3^- \end{pmatrix}$$

where r_1 and t_1 are the reflection and transmission coefficients at the first boundary and r_2 & t_2 are the reflection and transmission coefficients at the second boundary, where $r_1 = r_2 = r$. Assuming that no additional boundaries are encountered by the propagating wave after the imaginary slab, the backward propagating wave in region 3 can be set to zero yielding the following equation for the total reflection and transmission coefficients through the slab.

$$S_{11} = \frac{r - re^{-2|k_2|d}}{1 - r^2e^{-2|k_2|d}} \tag{2.19}$$

$$S_{21} = \frac{t_1t_2e^{-|k_2|d}}{1 - r^2e^{-2|k_2|d}} \tag{2.20}$$

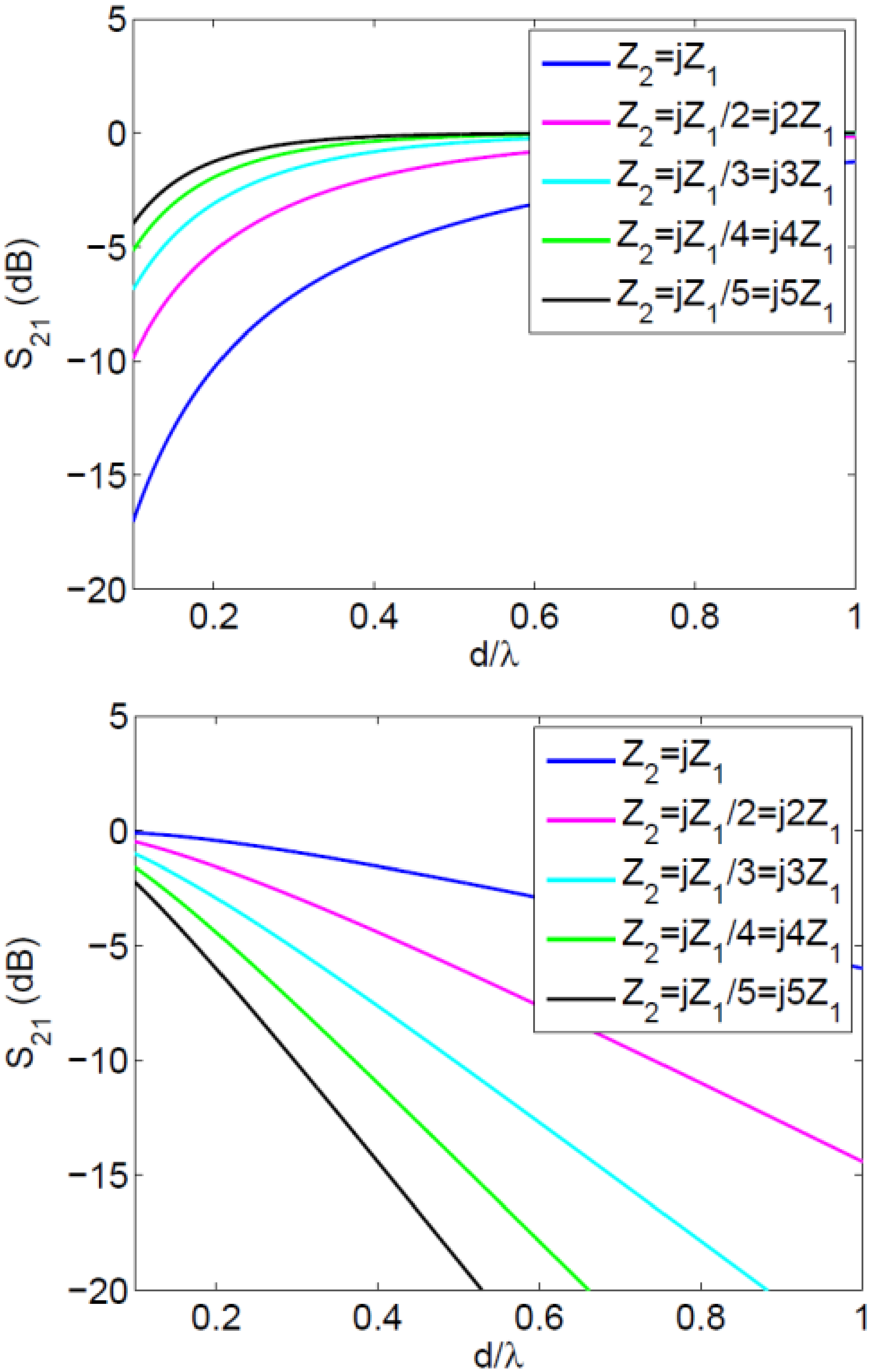

Figure 2.3- Plot of reflection (top) and transmission (bottom) for a semi-infinite dielectric slab having imaginary impedance.

Eqs. 2.19 &2.20 were evaluated for a normally incident plane wave propagating through an imaginary slab from free space. This calculation was performed for various slab thicknesses (d/λ) and relative impedance values (Fig. 2.3). For infinitely large slab thickness, all of the incident energy is reflected as expected from Eq. 2.15. As the thickness of the slab is decreased more and more energy is transmitted through to region 3. However even for relatively small slab thicknesses ($d < \lambda$), a significant portion of the incident energy is reflected even when the magnitude of the slab impedance is equal to the free space impedance. Therefore even a very thin slab of an imaginary impedance medium can be a highly effective reflector. For example a gold slab of thickness λ/10, which has a $\varepsilon' = -1678$ [53] at 1 GHz will reflect approximately 99.94% of the energy in a plane wave incident from free space.

Broadband Switching Imaginary Metamaterial

In general there are two ways in which imaginary impedances can arise in metamaterials. First thin wire media can exhibit negative permittivity at frequencies below the electric plasma frequency (Eq. 1.5). Second resonant structures such as the split ring resonators discussed in Chapter 1 can exhibit negative permeability above the resonant frequency of the SRR (Eq. 1.6), which persist up to the magnetic plasma frequency. If the properties of these elements are carefully tuned such that the electric plasma frequency of the thin wire structure is exactly equal to the magnetic resonant frequency of the SRR, then this medium will now possess two non-overlapping yet adjacent regions of imaginary impedance (Fig. 2.4). Furthermore, unlike its constituents in isolation this hybrid thin wire SRR unit cell will now have significantly larger

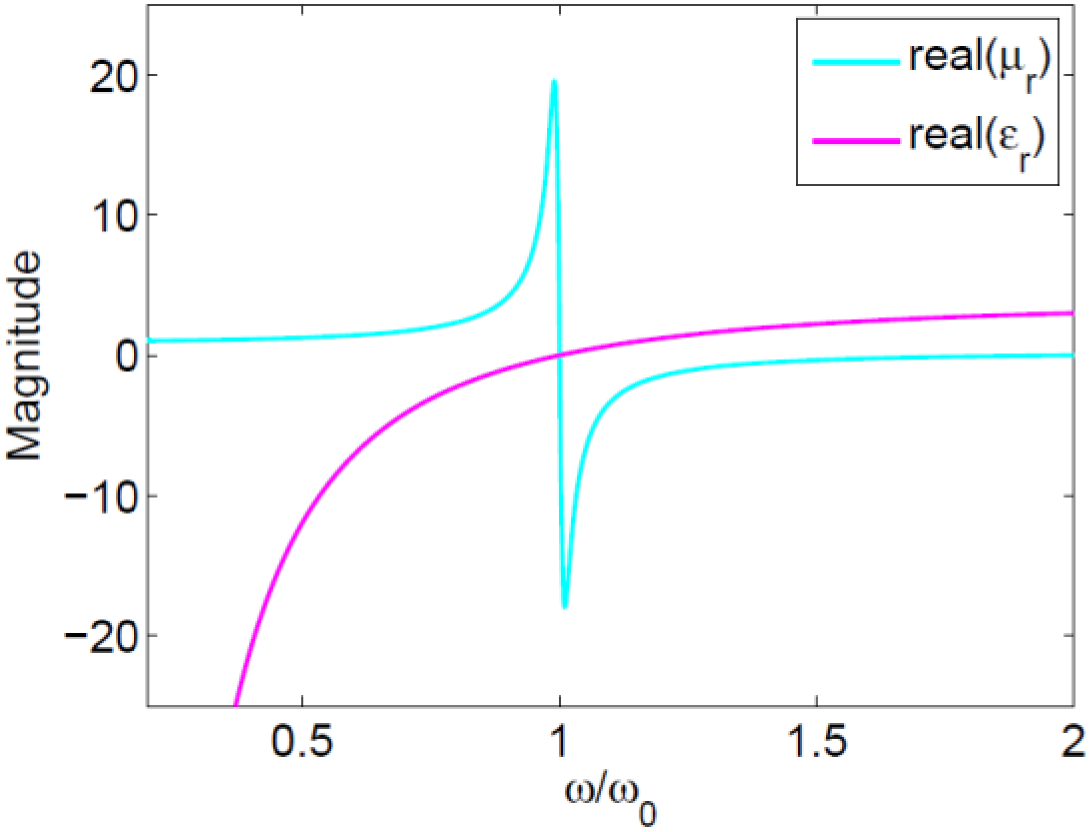

Figure 2.4- Plot of effective material parameters for a hybrid thin wire/SRR unit cell generating broadband imaginary impedance.

imaginary impedance bandwidth covering both the negative permittivity region of the thin wire medium and the negative permeability medium of the SRR medium.

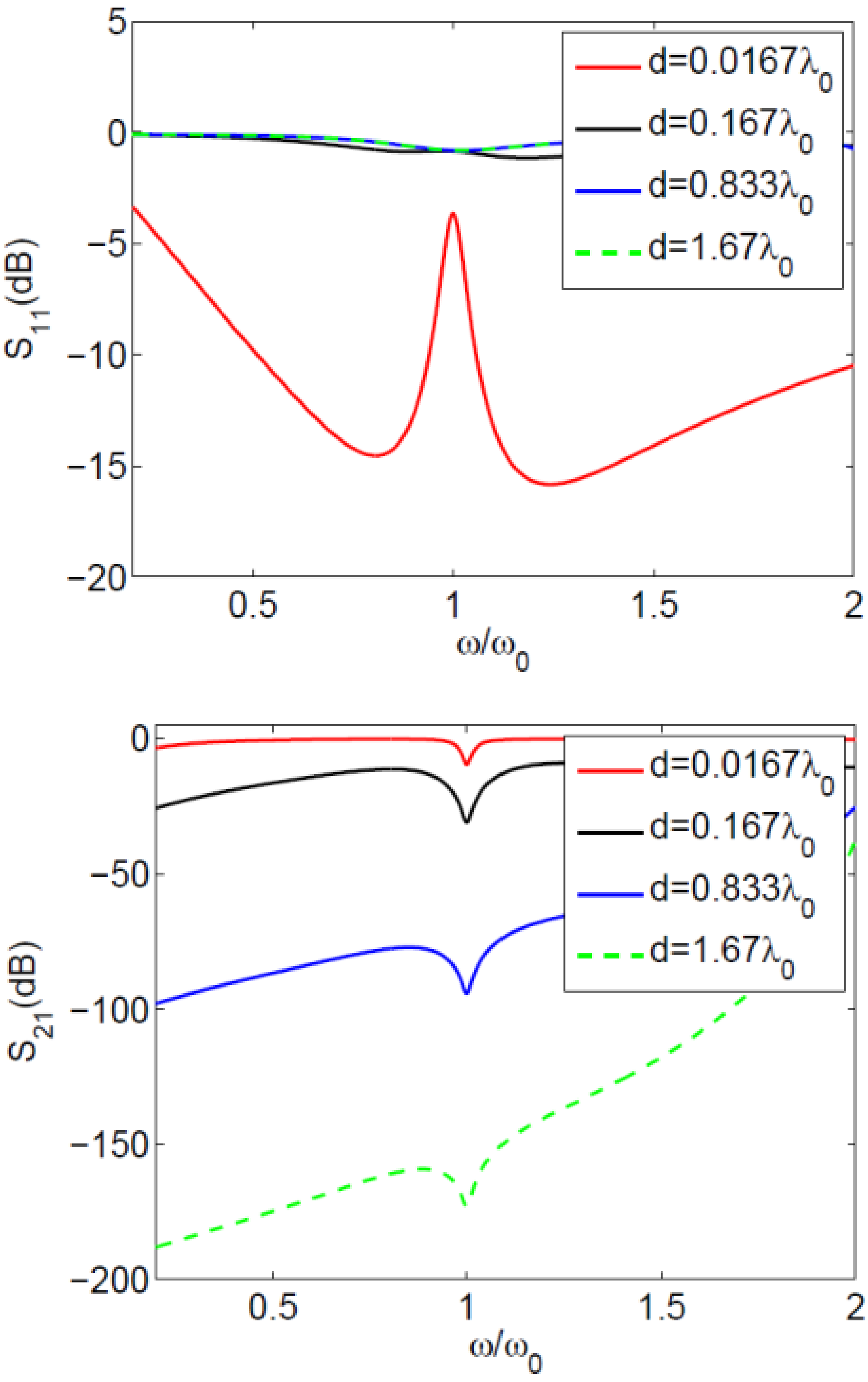

Figure 2.5- Plot of reflection (top) and transmission (bottom) for a semi-infinite metamaterial slab having broadband imaginary impedance. Several slab thicknesses are shown in the axial direction.

Using the equations for the effective permittivity and permeability of a homogenized media, frequency dependent reflection and transmission coefficients can be computed for this hybrid structure.

$$\varepsilon_{eff} = \frac{\varepsilon_0}{(1-F)}\left(1 - \frac{{\omega_p}^2}{\omega^2 + i\omega\Gamma}\right) \tag{2.21}$$

$$\mu_{eff} = \mu_0\left(1 - \frac{F\omega^2}{\omega^2 - {\omega_0}^2 + i\omega\Gamma}\right) \tag{2.22}$$

Due to causality, the index of refraction ($n = \sqrt{\varepsilon_{eff}\mu_{eff}}$) must be greater than 1 as the frequency goes to infinity. Therefore an additional factor inversely proportional to 1-F must be added to the permittivity. In order for Eqs. 2.21 & 2.22 to be valid for the geometry under investigation the following assumptions need to hold. First, the size of the metamaterial unit cell needs to be small enough that the homogenization limit is valid over the frequency range being investigated. Second, the mutual coupling between the elements in the unit cell should be negligible causing their combined response to be the same as the superposition of the isolated responses. Due to the complex nature of Eqs. 2.21 and 2.22, Eq. 2.19 is no longer valid as it assumes that the effective permittivity and permeability are purely real. Therefore it is rewritten below in its more general form.

$$S_{11} = \frac{r - re^{-2jk_2d}}{1 - r^2e^{-2jk_2d}} \tag{2.23}$$

$$S_{21} = \frac{t_1t_2e^{-jk_2d}}{1 - r^2e^{-2jk_2d}} \tag{2.24}$$

Substituting Eqs. 2.21 & 2.22 into Eq. 2.23, frequency dependent transmission and reflection coefficients were computed in MATLAB for a plane wave normally incident from free space on an ideal broadband imaginary metamaterial structure of various

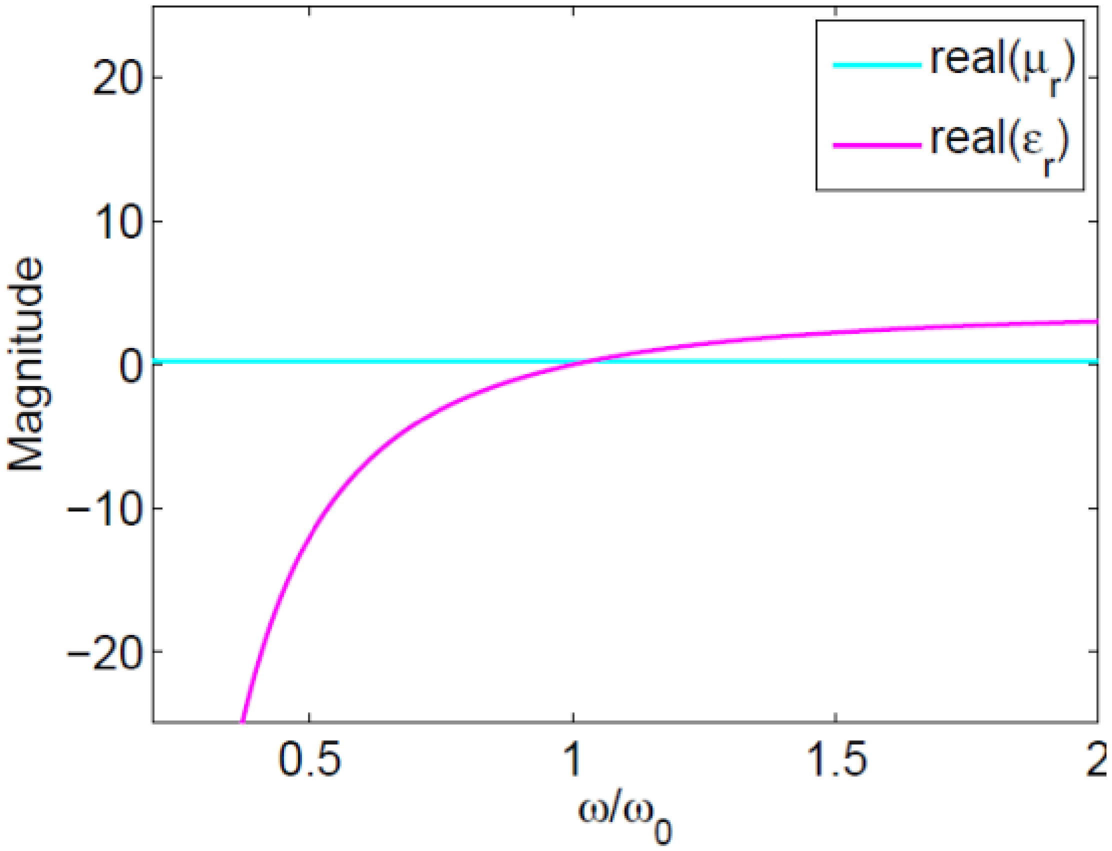

Figure 2.6- Plot of effective material parameters for a hybrid thin wire and shorted SRR unit cell.

thicknesses (Fig. 2.5). A nominal fill factor of 0.75 and dissipation factor of 1.25e-9 ω_0 were used. For exceedingly small thicknesses (d<$\lambda_0/100$) the medium is essentially transparent throughout the bandwidth investigated. This is expected as evanescent modes inside the slab have not sufficiently decayed at this depth, thus allowing waves to pass through the medium. As thickness is increased evanescent modes decay substantially more before reaching the second boundary at z=d, thus reflecting significantly more power at z=0. At a thickness of 0.167λ_0 more than 86% of the incident energy is reflected back into region 1 on average.

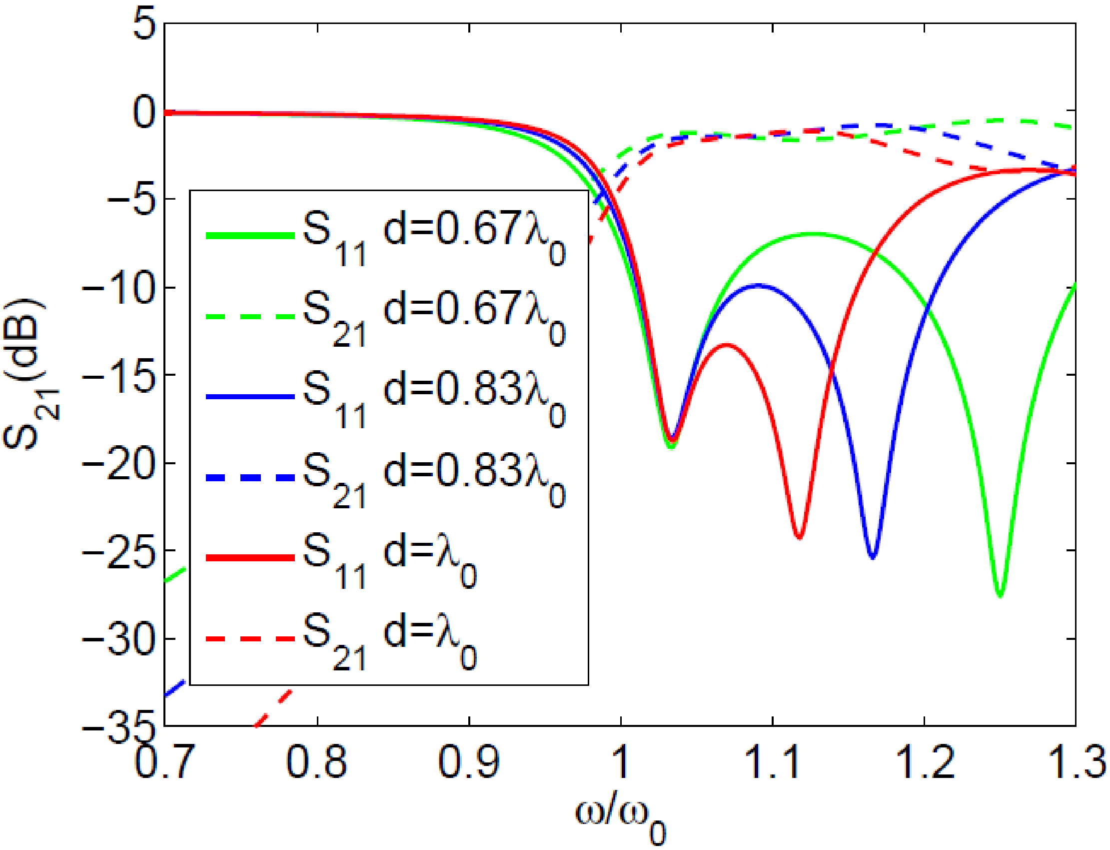

Figure 2.7- Plot of reflection (solid) and transmission (dashed) for a semi-infinite metamaterial slab composed of thin wires and shorted split ring resonators. Slab thicknesses of 4cm (green), 5cm (blue), and 6cm (red) are shown.

Unlike natural materials exhibiting imaginary impedance characteristics such as metals, metamaterials can drastically change their effective material properties in response to the power of an incident wave. Possibly the simplest way to achieve this effect, is to simply short the resonance in the metamaterial. In the case of the aforementioned structure this would involve putting a power dependent load in the gap of the SRR such that under some condition the switch would close, shorting the capacitance in the ring, destroying the LC resonance. In terms of the magnetic properties of the structure, this shorting of the SRR resonance would now render the effective permeability essentially frequency independent and less than 1 [17], whereas the effective permittivity would be essentially unaffected (Fig. 2.6).

$$\mu_{\boldsymbol{eff}} = \mu_{\mathbf{0}}(\mathbf{1} - \boldsymbol{F}) \tag{2.25}$$

Using Eqs. 2.23 & 2.24 reflection and transmission coefficients were computed using Eq. 2.25 for the effective permeability of the medium (Fig. 2.7). For a $0.83\lambda_0$ thick slab it can be seen that a substantial portion of the incident energy (> -3 dB) is transmitted through the slab over a 21% bandwidth centered at $1.28\omega_0$. Therefore simply by shorting the magnetic resonance in the metamaterial, the effective material properties can be changed from highly reflective to highly transparent over a broad bandwidth. While the broad nature of this bandwidth in the reflecting case is due to the overlap of the imaginary impedance regions present in the thin wire and SRR structure, the transparent case it is due to proximity of an impedance matched feature at $1.03\omega_0$ to a Fabry-Perot resonance. By adjusting the thickness of the slab the frequency at which this resonance occurs can be changed allowing the magnitude and width of this transmission region to be adjusted (Fig. 2.7).

Design

To implement the broadband imaginary metamaterial structure discussed in the previous section, a unit cell loaded with surface mount diodes was designed and demonstrated [40]. The broadband switching behavior of this metamaterial is achieved by creating two distinct sets of effective material parameters which are dependent on the variable resistance values of the diodes that load the structure. These effective material properties are controlled by a metamaterial unit cell (Fig. 1) consisting of two separate

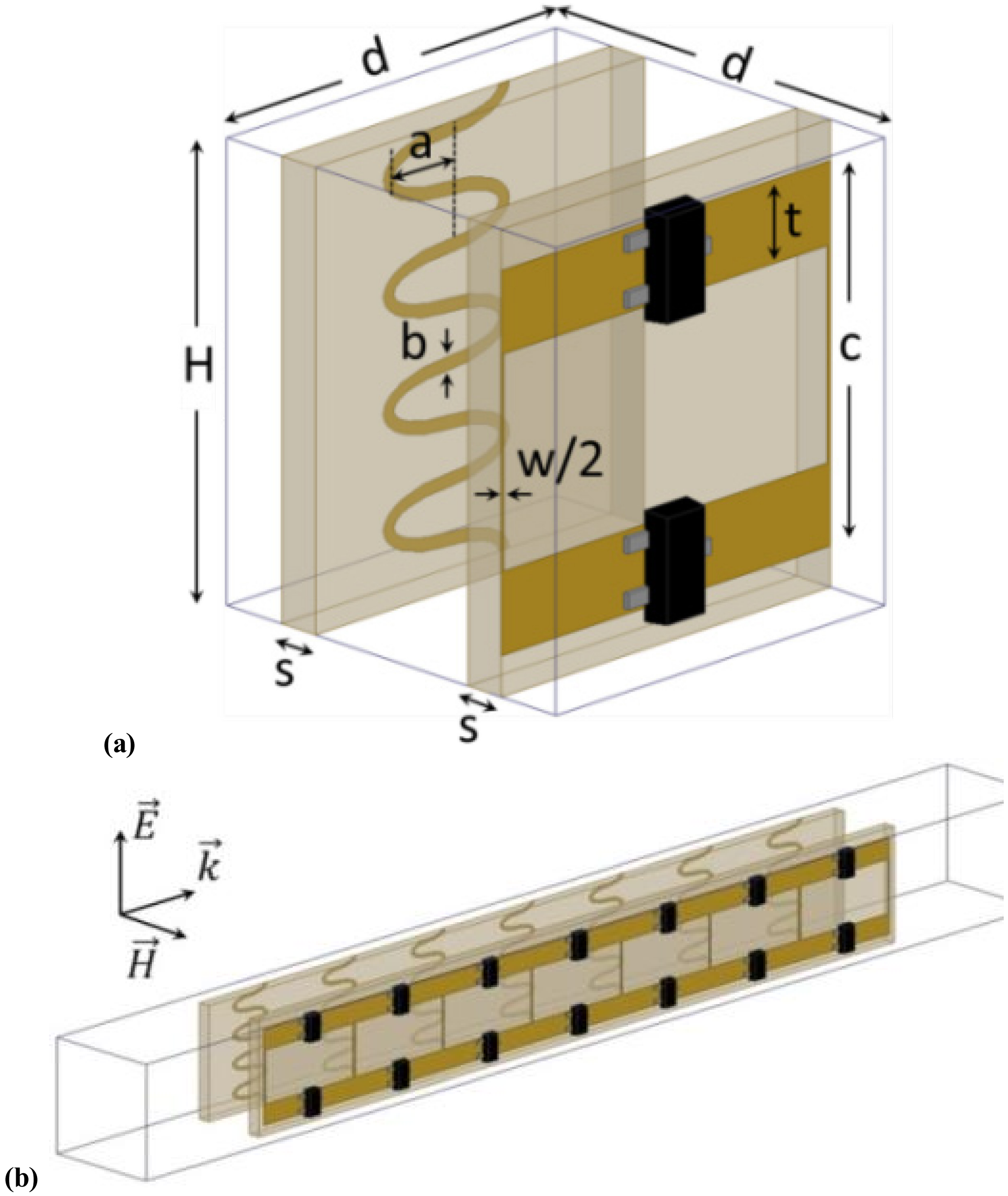

Figure 2.8- (a) CAD drawing of basic unit cell for broadband switching metamaterial structure. This design uses two basic elements: magnetic rings loaded with Schottky diodes (illustrated as black surface mount components) and inductive traces. (b) By connecting these basic elements together a traveling wave configuration is created.

components: an inductive element that provides an exclusively electric response and a magnetic element which exhibits both electric and magnetic effects. The inductive elements are formed by meandered copper traces oriented parallel to the electric field.

The meandering shape of these elements increases the inductance while allowing the linewidth of the traces to remain large enough to be fabricated using standard printed circuit lithography techniques. The magnetic elements are manifested as a series of linked metallic loops, the axes of which are oriented along the direction of the magnetic field vector. Fig. 2.8b shows seven loops connected to each other in the direction of propagation to create a traveling-wave structure [53]. Each individual loop is broken in two places (top and bottom) allowing an antiparallel diode pair to be inserted into each gap (each pair is contained in a single package, Fig. 2.8a).

Parameter	**Value**
H	8.5 mm
d	8 mm
c	7 mm
b	10 mil
a	1.4 mm
w	5 mil
t	60 mil
s	32 mil

Table 2.1-Design parameters for unit cell in Fig. 2.8

When excited with a transverse-electric wave, where the electric field is oriented parallel to the electric field vector shown in Fig. 2.8, the response of this structure can be described by one of two limiting cases: broadband reflective and broadband non-reflective. In the reflective case, which occurs at power levels too low to activate the diodes, the impedances in the gaps of the rings are dominated by the diode capacitance and these elements behave similar to split-ring resonators (SRRs). Unlike traditional

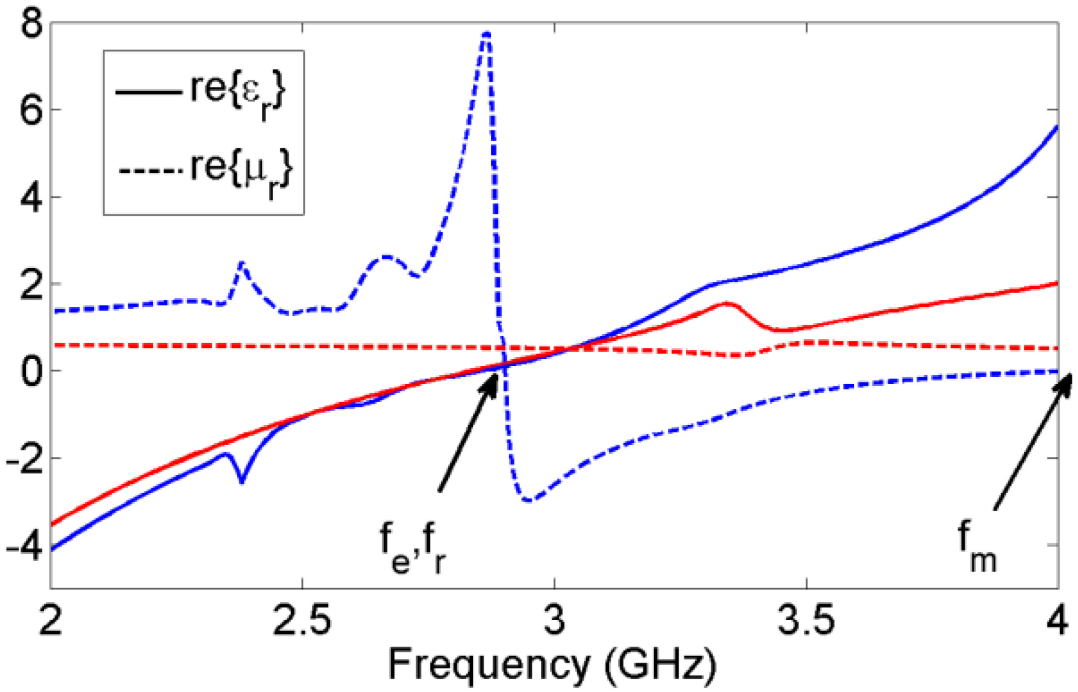

Figure 2.9- Effective material parameters in the low power state (blue) and high power state (red) configuration. These material parameters were extracted from the simulated S-parameters shown in Fig. 2.10.

SRRs, these loops are electrically coupled in a traveling-wave configuration to increase the bandwidth over which a negative permeability can be achieved [54].

When induced voltages in the loops are above the activation voltage of the diodes, the diode capacitance is shorted, destroying the magnetic resonance. Without the resonance, the permeability of the structure is positive for all frequencies. Consequently, the wider the negative permeability bandwidth is in the low power state, the greater the bandwidth of the switching performance. The magnitude of the relative permeability can be tuned through iterative optimization to match the existing relative permittivity created by the inductive elements, resulting in an impedance match at a designed frequency (Fig 2.9).

Simulations of this metamaterial were performed using ANSYS' HFSS. Fig. 2.8b shows the geometry for the design under investigation. Both magnetic and electric elements are printed on a RO4003C substrate with ε_r=3.55 and tan δ=0.0027. Periodic boundary conditions are used to simulate an infinite array excited by a normally incident plane wave. Lumped element ports are placed into the gaps of rings to simulate the effective impedance of the Skyworks SMS7621 Schottky diode in its conducting and non-conducting states. A capacitance value of 0.31 pF and an off-state parallel resistance of 5 kΩ for these elements were obtained by reflection measurements at 0 dBm of a 50-Ω microstrip transmission line terminated with two antiparallel diodes connected to ground. Accurate impedance extraction could not be performed at a power high enough to fully turn on the diodes, so a parallel resistance of 12 Ω was taken from the manufacturer's specification sheet [55]. Across an 810-MHz bandwidth centered at 3.4 GHz a nearly -10-dB reduction in reflected power is observed between small (12 Ω) and large (5 kΩ) resistance values (Fig. 2.10). Furthermore, it can be seen from the corresponding S_{21} values that a large portion of the energy at high power is transmitted.

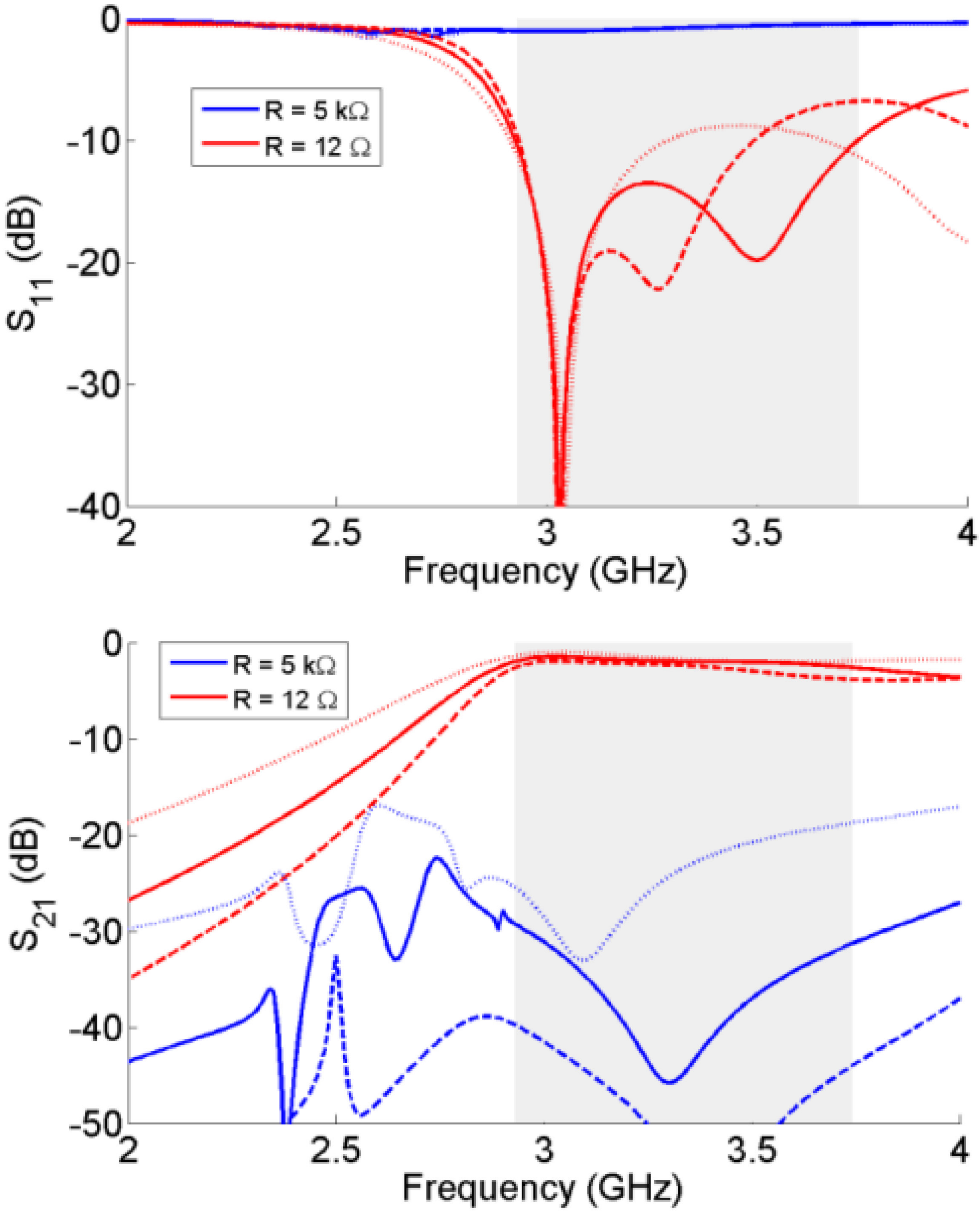

Figure 2.10- Simulated reflection (top) and transmission (bottom) spectra for the seven-cell-thick design (solid) as well as for five (dotted) and nine (dashed) cells. Blue lines show low power excitation and red lines show high power excitation. The 10dB bandwidth of the seven-cell structure is highlighted in gray.

Fig. 2.10 also shows how changing the number of cells in the direction of propagation affects the impedance match of the metamaterial slab. The frequency at which the electrical thickness of the slab is 180° will have a reflection null. Increasing the thickness of the slab brings this frequency closer to the design frequency (where there is a reflection null due to the impedance match) and allows the reflection coefficient to be minimized over a wide bandwidth. We chose a thickness of seven cells to maximize the 10-dB bandwidth.

Chapter 3 -Nonlinear Multiconductor Transmission Line Analysis of Broadband Switching Metamaterials

In the previous chapter a broadband nonlinear metamaterial structure was proposed and investigated in numerical electromagnetic simulation. This structure consisted of two separate components: an inductive element that provides an exclusively electric response and a magnetic element which exhibits both electric and magnetic effects. By loading the magnetic elements of this structure with a nonlinear impedance, such as a diode, the transmission characteristics of the device can be switched between two broadband states. When the impedance of this nonlinear load is high, this structure exhibits broadband reflective characteristics due to its imaginary impedance. However when this impedance is low the structure becomes impedance matched over a broad bandwidth, passing incident radiation.

This passive switching behavior is particularly useful for applications such as high power limiting and field confinement. In these applications, powerful electromagnetic fields may exist near sensitive equipment and consequently need to be suppressed before they can cause damage or saturate sensors. For these applications the manner in which these self-biasing metamaterials switch from one state to another as a function of time is particularly important. While the steady state performance of such structures are easily modeled in full wave simulation by replacing diodes with their lumped element equivalents, transient analysis requires modeling the time-varying and nonlinear I-V characteristics of the diode as well as their interaction with the induced current. Therefore in this chapter a nonlinear multiconductor transmission line analysis is proposed to analyze the transient behavior of this broadband switching metamaterial structure. Because this model can be implemented in commercial microwave circuit simulators such as Agilent's Advanced Design System (ADS), manufacturer specified diode models can be implemented allowing for rapid evaluation of a wide variety of configurations.

In this chapter, a multiconductor transmission line framework will be developed to analyze the transient behavior of this structure. Following a brief introduction to multiconductor transmission line analysis, an equivalent circuit representation will be developed for symmetric nonlinearities. Simulations of this configuration will be performed in ADS for dual-anti parallel Schottky. This initial multiconductor framework will then be extended into a more general 4-conductor framework which can handle both symmetric and non-symmetric nonlinearities. Simulations for single hyperabrupt varactor diodes will be provided.

Multiconductor Transmission Line Analysis

At microwave frequencies, the wavelength of the signals being transmitted is often on the same order of or smaller than the lengths of conductors. In these scenarios,

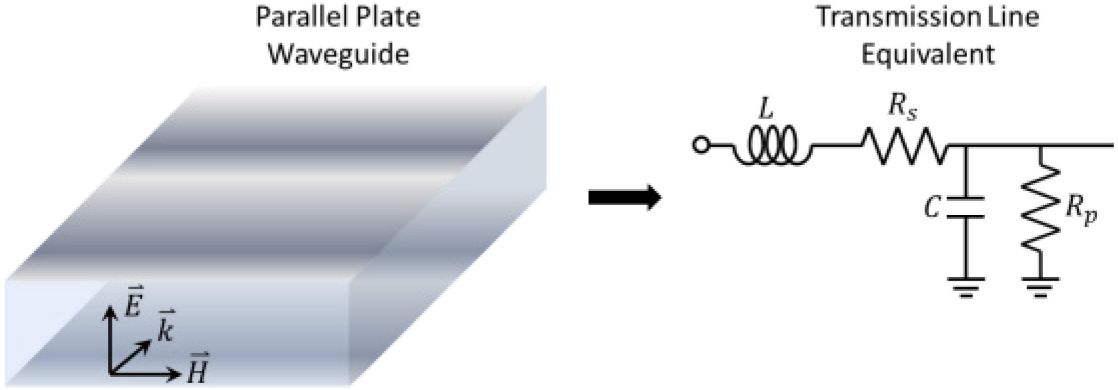

Figure 3.1- Illustration of a parallel plate waveguide and its transmission line equivalent.

guided mode structures are required for efficient transmission. Common examples include striplines, microstriplines, coaxial lines, and. In general all of these structures operate by confining an alternating field between two conductors with transverse electric and magnetic components, also known as a TEM-mode. Electromagnetic waves propagating in this mode are generally well modeled by equivalent circuits known as transmission lines. A canonical transmission line is shown in Fig. 3.1. This circuit consists of a serial inductor and resistor in parallel with a resistor and capacitor. Propagation of an alternating voltage (V) and current (I) along this transmission line is described by the telegrapher's equations [53],

$$-\frac{d\boldsymbol{V}}{d\boldsymbol{x}} = \boldsymbol{ZI} \tag{3.1}$$

$$-\frac{d\boldsymbol{I}}{d\boldsymbol{x}} = \boldsymbol{YV} \tag{3.2}$$

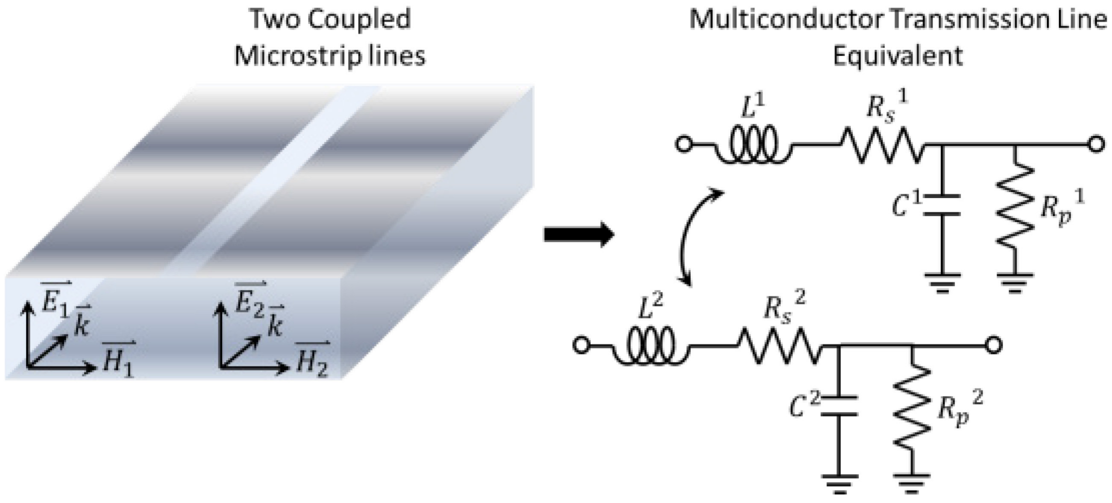

Figure 3.2- Illustration of two coupled microstrip lines and their transmission line equivalent.

where Z is the characteristic impedance of the transmission line defined as $Z = R_s + j\omega L$ and Y is the characteristic admittance defined as $Y = G + j\omega C$. By substituting Eq. 3.2 into Eq. 3.1 a single second order differential equation can be obtained assuming the admittance of the line does not vary along its length (x).

$$\boldsymbol{\frac{d^2V}{dx^2} = ZYV} \qquad (3.3)$$

Solutions to Eq. 3.3 are forward and backward propagating waves with the propagation constant $\beta = \sqrt{ZY}$.

$$\boldsymbol{V = Ae^{-\sqrt{ZY}x} + Be^{+\sqrt{ZY}x} = Ae^{-\beta x} + Be^{+\beta x}} \qquad (3.4)$$

By inspection Eq. 3.4 is mathematically similar to solutions for the electric field of a guided wave. Therefore by choosing appropriate values of inductance, capacitance, and resistance, accurate transmission line equivalents can be developed for waves propagating through these structures.

In the case where two or more guided modes are closely spaced, energy and information from one guiding structure can be transferred to the other. For these scenarios a coupled transmission line theory is required. This coupled analysis is commonly accomplished through a framework known as multiconductor transmission line analysis [56]. For N coupled transmission lines, this theory proposes the voltage on the i^{th} transmission line V_i can be found replacing the scalar quantities in Eq. 3.1 and 3.2 (i.e. Y and Z), with matrices [53].

$$-\frac{d}{dx}\begin{bmatrix} V_1 \\ \vdots \\ V_N \end{bmatrix} = \begin{pmatrix} Z_{11} & \cdots & Z_{1N} \\ \vdots & \ddots & \vdots \\ Z_{N1} & \cdots & Z_{NN} \end{pmatrix} \begin{bmatrix} I_1 \\ \vdots \\ I_N \end{bmatrix} \rightarrow -\frac{d}{dx}\boldsymbol{V} = \boldsymbol{ZI} \qquad (3.5)$$

$$-\frac{d}{dx}\begin{bmatrix} I_1 \\ \vdots \\ I_N \end{bmatrix} = \begin{pmatrix} Y_{11} & \cdots & Y_{1N} \\ \vdots & \ddots & \vdots \\ Y_{N1} & \cdots & Y_{NN} \end{pmatrix} \begin{bmatrix} V_1 \\ \vdots \\ V_N \end{bmatrix} \rightarrow -\frac{d}{dx}\boldsymbol{I} = \boldsymbol{YV} \qquad (3.6)$$

Diagonal elements of the **Y** and **Z** matrices correspond to the characteristic impedance on each individual transmission line and the off-diagonal elements correspond to the mutual coupling terms. As before solutions to equations 3.5 & 3.6 are backward and forward propagating waves, except the propagation constant **β** and coefficients **A** and **B** are matrices instead of scalars.

$$\boldsymbol{V} = \boldsymbol{A}\boldsymbol{e}^{-\boldsymbol{\beta x}} + \boldsymbol{B}\boldsymbol{e}^{+\boldsymbol{\beta x}} \qquad (3.7)$$

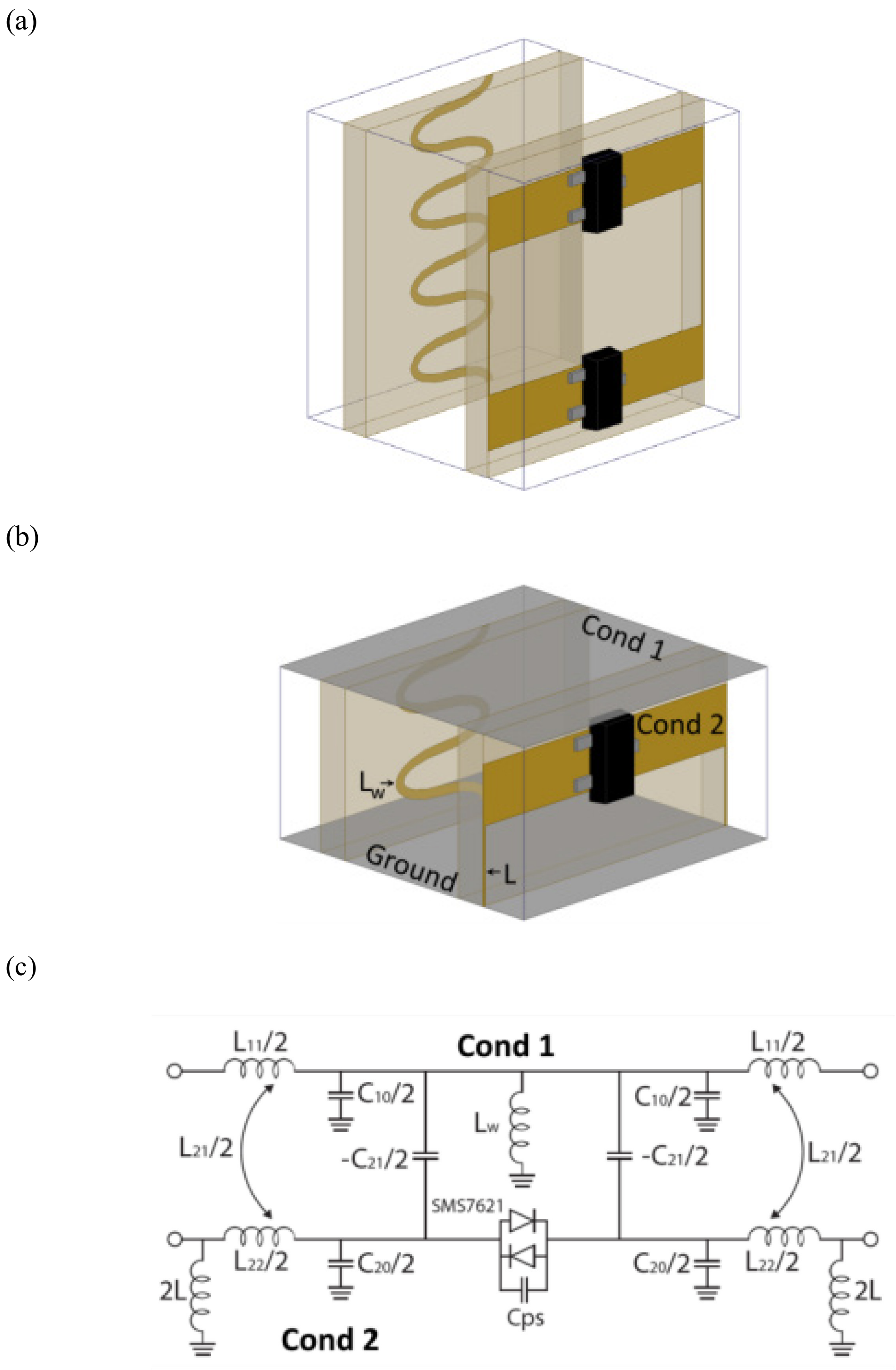

Figure 3.3 –a.) Basic unit cell for the Schottky loaded broadband switching metamaterial. b..) Due to its electric symmetry, the top and half plane of this unit cell can be replaced with PEC boundaries. c.) Nonlinear multiconductor transmission line equivalent of the half cell in (b).

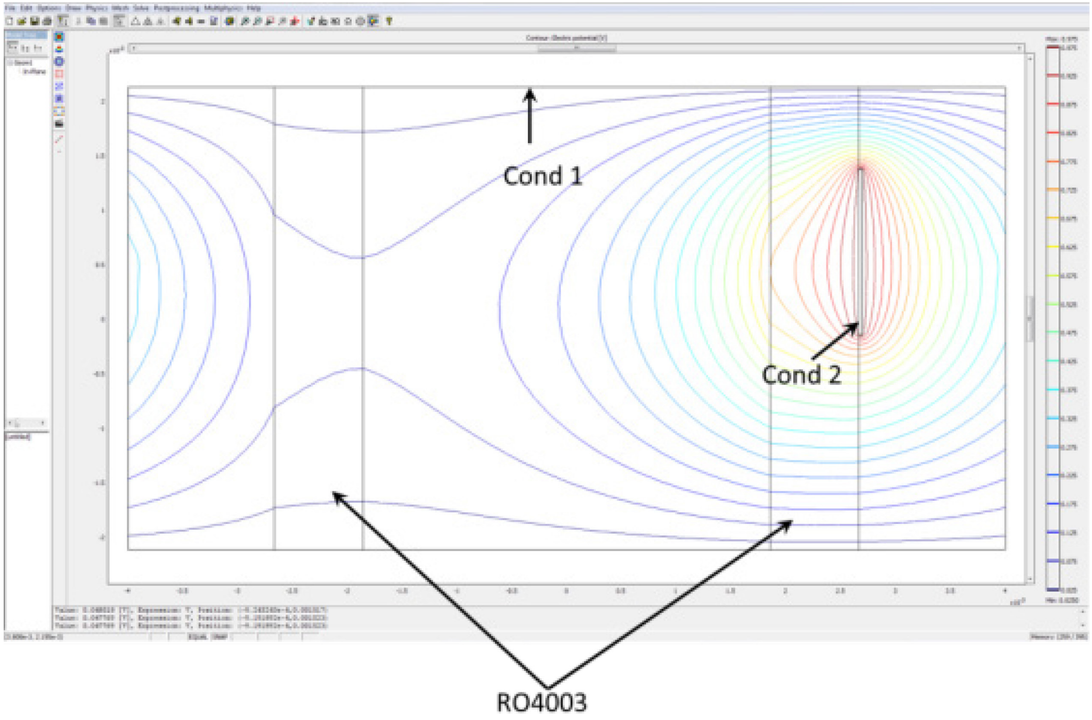

Figure 3.4- Screenshot of COMSOL simulation used to compute inductance and capacitance matrices. Streamlines show variation of electric potential throughout the transverse cross section of the unit cell.

For the broadband switching metamaterial structure discussed in the previous chapter this multiconductor transmission line analysis provides a convenient tool for analyzing the transient behavior of these structures. This transmission line analysis is ideally suited, both for its numerical efficiency and its ability to handle discrete nonlinear circuit elements. Previous authors have demonstrated the utility of multiconductor transmission line analysis for simulating broadband traveling wave metamaterial structures. In particular Rudolph et. al [57], showed that this analysis provided a close facsimile to full-wave FEM analysis for a broadband negative refractive index metamaterial structure. In the following chapters this foundational work in traveling-wave NRI structures will be expanded to analyze the transient behavior of the broadband switching metamaterial.

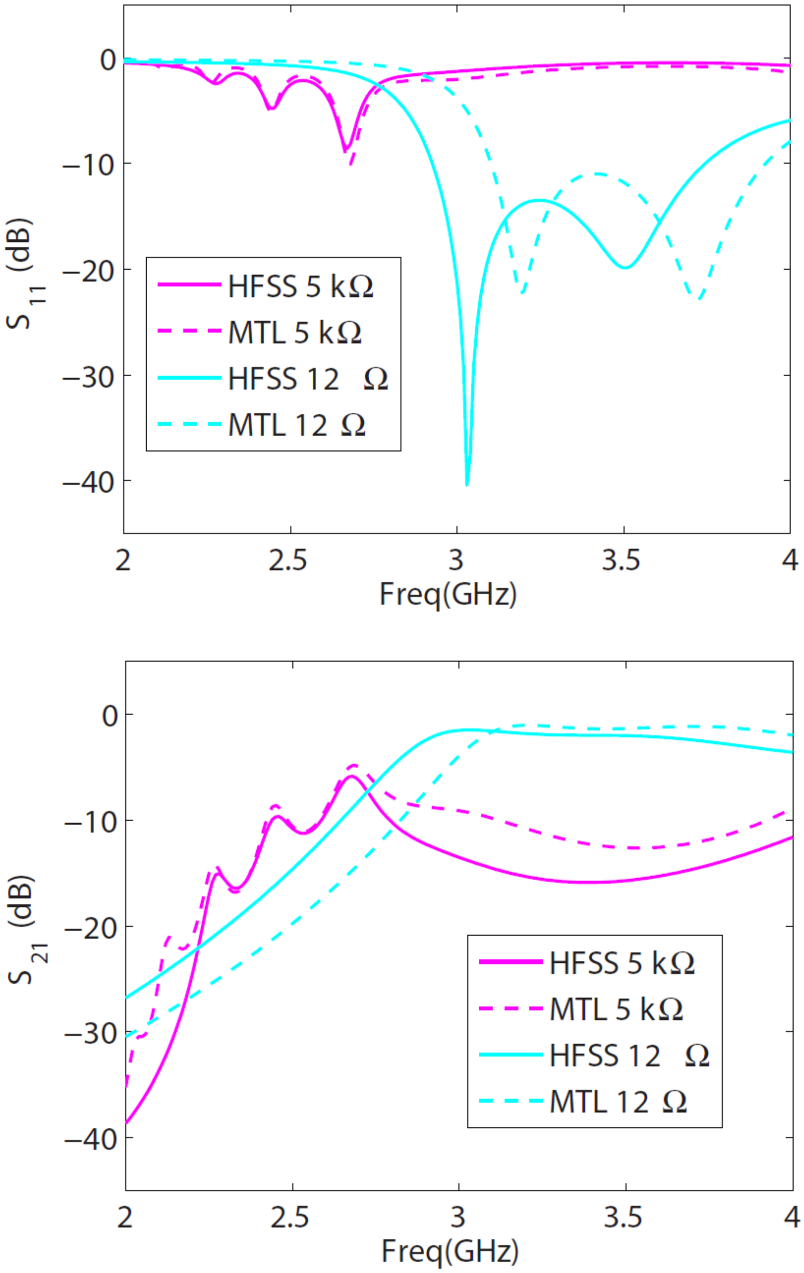

Figure 3.5- Comparison between simulated high power (cyan) and low power (magenta) reflection spectra for the Schottky loaded broadband switching nonlinear metamaterial structure shown in Fig. 1. Results obtained from HFSS (solid) show good agreement with those obtained from multiconductor transmission line analysis.

Two Conductor Transmission Line Analysis

The basic unit cell for the broadband switching metamaterial structure is shown in Fig. 3.3a. For vertically polarized waves the top and bottom of the unit cell can be terminated with perfect electric conductors (PEC) to simulate infinite periodicity in the vertical dimension due to image theory. Assuming this structure is loaded with a symmetric nonlinearity such as two anti-parallel diodes, the impedance in the gaps of the rings will vary equally to forward and reverse current. Thus it can be observed that this unit cell possesses electric symmetry allowing the half plane to be terminated as well with PEC (Fig. 3.3b). This reduced unit cell now consists of an inductor connecting the two conducting boundaries and transmission line structure (Cond 1) connected to the bottom conductor through the inductive elements L. The top conducting boundary in Fig. 3.3b is connected to the bottom conducting boundary through the inductive element L_w, yielding a second transmission line which is analogous to the free-space wave propagating through the structure (Fig. 3.3c).

Coupling between these two transmission lines, which represents the coupling between the broadband switching metamaterial and an incident TEM wave, occurs through a combination of inductive and capacitive coupling, which is described by the capacitance and inductance matrices between Cond 1 & Cond 2. These matrices can be found by considering the 2-conductor network formed by Cond 1 & Cond 2. Since the unit cell is much smaller than the wavelength range of interest this 2-port network analysis can be performed in the quasi-static regime [57]. To extract impedance and admittance matrices, simulations of the transverse cross section of the unit cell in Fig. 1 were performed in COMSOL using the AC/DC module (Fig. 3.4). Since these transmission lines are assumed to be lossless the impedance and admittance can be written in terms of their reactive components leading to the inductance and capacitance matrices [53].

$$\begin{pmatrix} Z_{11} & Z_{12} \\ Z_{21} & Z_{22} \end{pmatrix} = j\omega \begin{pmatrix} L_{11} & L_{12} \\ L_{21} & L_{22} \end{pmatrix} \tag{3.8}$$

$$\begin{pmatrix} Y_{11} & Y_{12} \\ Y_{21} & Y_{22} \end{pmatrix} = j\omega \begin{pmatrix} C_{11} & C_{12} \\ C_{21} & C_{22} \end{pmatrix} \tag{3.9}$$

C_{10} and C_{20} are the same as [57], such that $C_{10} = C_{11} + C_{21}$ and $C_{20} = C_{22} + C_{21}$. The loading inductors (L & L_w) are extracted from full wave simulations. To compute the value for L_w, broadband S-parameter simulations of electric element on the left of Fig. 3.3a are performed in the absence of the magnetic elements. Once the ports in this simulation have been de-embedded, the resulting S-parameters can be used to compute the shunt inductance using ABCD analysis [1]. A similar analysis is performed for the inductor connecting the top and bottom conductors of the rings in Fig. 3.3a. The frequency dependence of these values was found to be negligible over the bandwidth of interest. The values for all of these elements are tabulated in Table 3.1.

Parameter	**Value**
L_{11}	0.264 nH
L_{22}	0.244 nH
L_{21}	0.176 nH
L	2.92 nH
L_w	4.73 nH
C_{10}	5.47 fF
C_{20}	7.80 fF
C_{21}	15.6 fF

C_{ps}	0.17 pF
C_{pv}	0.44 pF
L_{pv}	0.7 nH

Table 3.1-Values for circuits in Fig. 3.3 and 3.8

Transient simulations of these coupled nonlinear transmission lines were performed using Agilent's Advanced Design System (ADS). The Skyworks SMS7621-075LF diodes loading the unit cell in Fig. 3.3a consist of a pair of anti-parallel Schottky diodes placed in a single package. In ADS this diode combination was modeled using two PN junction diodes and a single parallel capacitance. Spice parameters for each

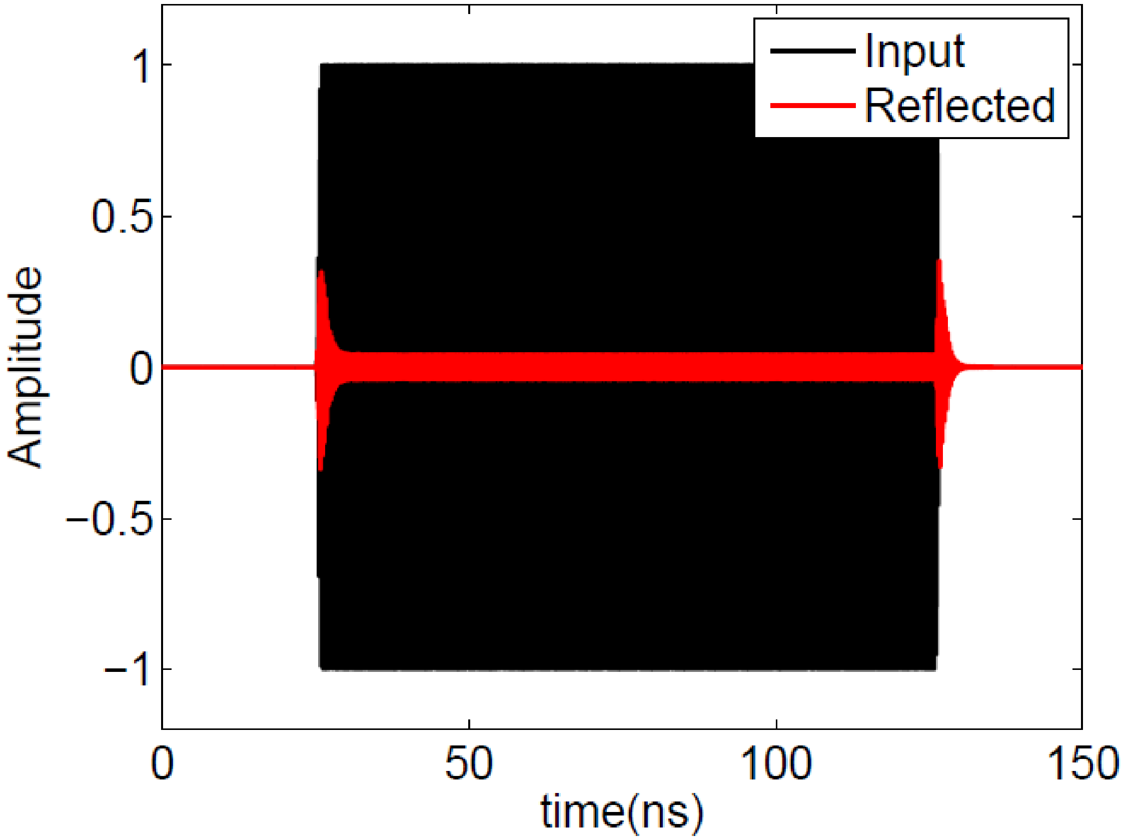

Figure 3.6- Simulated response of broadband switching metamaterial loaded with Schottky diodes to an input 100 ns RF pulse at 3.2 GHz, with a 1 ns rise/fall time.

diode were taken from the manufacturer's specification sheet [55]. The parallel capacitor, accounting for the package reactance, was found to be approximately 0.45 pF from measurements of the structure [40]. Once the loading elements in this structure have been applied the number of unit cells along the direction of propagation can be set by connecting the top and bottom transmission lines in series to their respective facsimile. For this demonstration seven transmission lines were simulated in series to model the seven unit cells in the physical structure. For the bottom transmission line, the first and last element in this series combination are terminated to ground with an additional loading inductor having the same value as L [57]. The top transmission line, which acts as the input and output port of the simulation is terminated with a 200.14-Ω load, which corresponds to the free space impedance scaled by the height-to-width ratio of the unit cell in Fig. 3.3b.

To validate this nonlinear transmission line analysis, S-parameters of the unit cell shown in Fig. 3.3a, were obtained using Ansoft's HFSS and compared at both high and low incident power levels. For the full wave simulation, the response of the diodes at low power levels was simulated using a lumped element equivalent consisting of a parallel 0.45-pF capacitor and 5-kΩ resistor. At high power levels this combination was changed to a 12-Ω resistor. These resistance values were found from measurements of this diode, made on a 50-Ω microstrip [40]. Comparing the S-parameters obtained from full wave simulation and those obtained from the nonlinear transmission line analysis we see good agreement from 2 to 4 GHz (Fig. 3.5). A slight shift in frequency is observed between these two models in the case of the 12 Ω simulations.

Using this nonlinear multiconductor transmission line analysis the transient response of this structure can be investigated for arbitrary excitations. The response time, or the amount time required for the structure to transition from one state to another once sufficient voltage has been applied, is of particular interest for applications which require fast transients. The characteristic response time of this structure was investigated using a 100ns pulsed RF signal at 3.2 GHz with a 1ns rise/fall time. For this demonstration the center frequency of 3.2 GHz was chosen to coincide with the impedance matched frequency of the structure in the high power state and thus ensure a large variation between high and low power states. For an input waveform with peak voltage of 10 V,

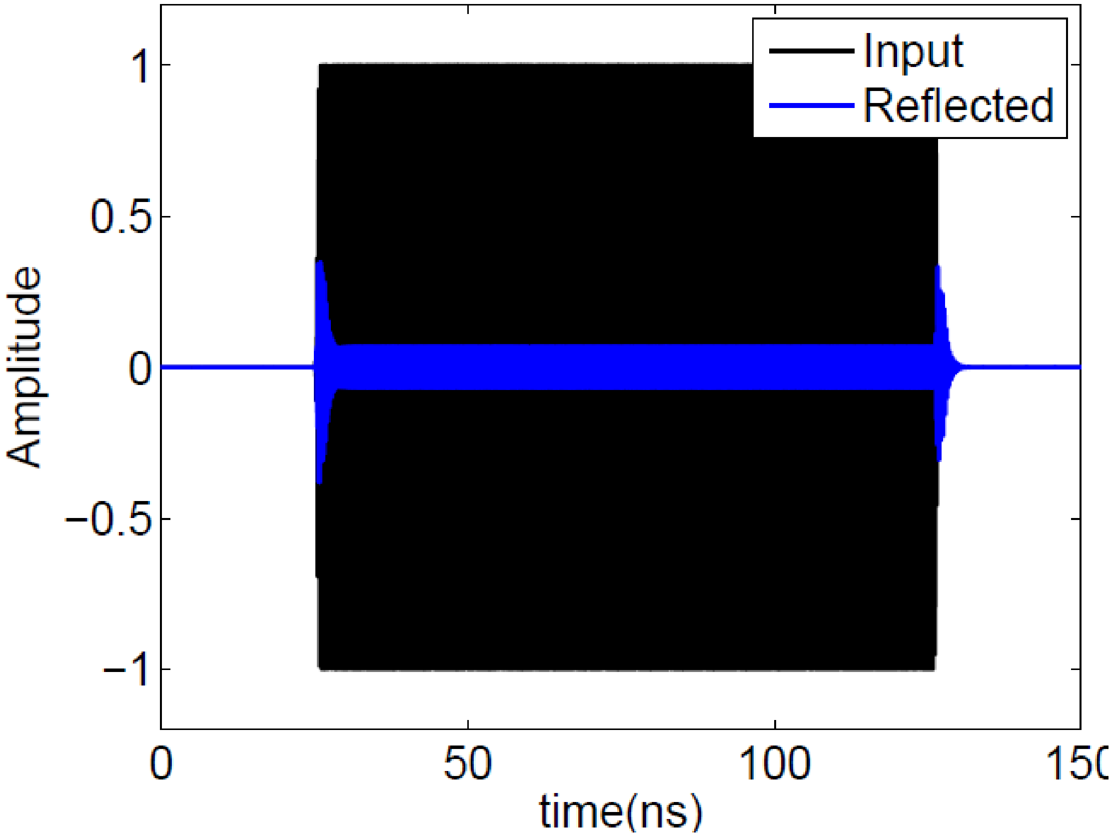

Figure 3.7- Simulated response of broadband switching metamaterial loaded with 12 Ω resistors to an input 100 ns RF pulse at 3.2 GHz, with a 1ns rise/fall time.

reflected and transmitted signals can be observed to exhibit transient behavior over 4ns time window before reaching steady state (Fig 3.6).

This response is primarily due to the response time associated with the bandwidth of the pass band in the high power state and not due to the considerably shorter (~10 ps) transit time of the diodes. The effect of this can be seen replacing the diodes in the structure with a series resistance of 12 Ω which is equivalent to resistance of the diodes in the high power state. Transient simulations of this linear structure generate a similar reflected pulse shape, although with slight higher amplitude due to the absence of loss in the diodes during the transitional voltage range. This similarity confirms that the response time of the structure is not limited by the switching time of the diodes and in fact that this concept should work at considerably higher frequency before the transient time of the diodes becomes a limiting factor.

Four-Conductor Transmission Line Analysis

At low incident power levels the dual anti-parallel Schottky diodes loading the metamaterial structure exhibit high impedance preventing the circulation of current in the magnetic elements and thus creating a magnetic resonance. By setting this magnetic resonance equal to the electric plasma frequency, an imaginary impedance can be created over a broadband which strongly reflects incident radiation. At high power levels the impedance of these diodes is significantly reduced shorting the magnetic resonance and allowing the structure to be impedance matched over a broad bandwidth, thus reducing significantly reducing the reflected radiation. By changing the response of these diodes to the induced voltage, the response of the structure to incident radiation can be drastically altered. Unlike Schottky diodes, varactor diodes can exhibit large decreases in capacitance as a function of reverse bias thus causing these diodes to transition from low to high impedance. Therefore by interchanging the Schottky diodes with suitable varactor diodes, the response of this broadband switching metamaterial structure to incident power can effectively be inverted.

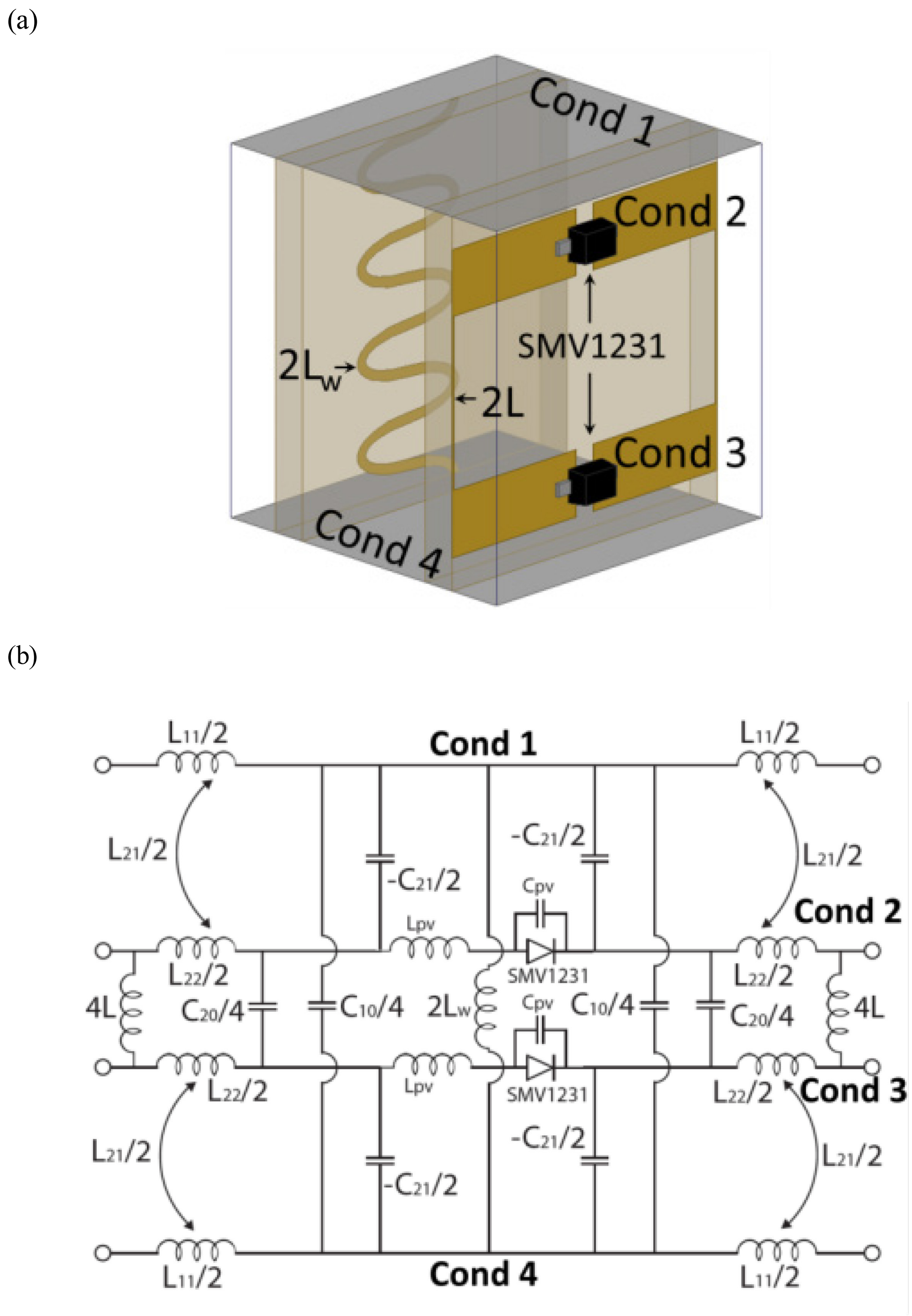

Figure 3.8 - Basic unit cell for the varactor loaded broadband switching metamaterial and its nonlinear multiconductor transmission line equivalent. Values for the elements of the multiconductor transmission line model are tabulated in table 3.1.

To demonstrate this concept the Skyworks SMV1231-079LF varactor diode, was chosen for its large zero-bias capacitance of 2.35 pF and its small package capacitance of 0.44 pF [58]. Using a lumped element equivalent to simulate the response of this diode at low incident voltages, the dual anti-parallel Schottky diodes shown in Fig. 3.3 were replaced with a series 2.5-Ω resistor, 0.7-Ω inductor, and 2.35-pF capacitor. Due to the large capacitance S_{21} and S_{11} values for this structure closely match those obtained for the Schottky diode loaded structure at high power levels (Fig. 3.5). According to the manufacturer's specification sheet [58], the capacitance of the SMV1231 diode decreases to the minimum value of 0.44 pF at a reverse bias voltage of 8 V. This decrease in capacitance causes the magnetic resonance of the structure to occur near the electric plasma frequency largely reflecting incident radiation similar to the Schottky loaded structure at low power. Furthermore these results show good agreement with simulations performed in HFSS using identical lumped elements (Fig. 3.9).

The transient response of this structure can be investigated by replacing these lumped element equivalents with a single PN junction diode model having SPICE parameters given by the manufacturer's specification sheet. A parallel capacitance of 0.44 pF, as well as a series resistance of 2.5 Ω and an inductance of 0.7 nH is added to this diode to account for Ohmic losses and package parasitics. Because the nonlinearity loading the magnetic elements of the structure is now comprised of a single semiconductor junction as opposed to two anti-parallel junctions, the response of this device to positive and negative induced voltages are different. In the case where the diodes loading the top and bottom half of the unit cell are oriented in the same direction as shown in Fig. 3.8, the electric symmetry in the unit cell is broken preventing the use of a PEC boundary at the half plane of the unit cell. Therefore to properly simulate the response of this structure a four conductor MTL simulation is required, where the two transmission lines shown in Fig. 3.3c, are mirrored and subsequently grounded to their mirror images as shown in Fig. 3.8b. The first and last elements are connected to their image through a 400.28-Ω load for the top and bottom lines and a 2-L inductor for the middle lines.

Through this four conductor transmission line model, the transient switching of this varactor loaded structure can be observed. Using a continuous wave (CW) input signal at 3.4 GHz, transmitted signals were monitored for various input voltages (Figs. 3.10-3.13). At low power levels, below the forward-bias threshold of the diode, this structure primarily passes incident radiation similar to the Schottky-loaded structure at high incident power levels. When the induced voltage exceeds the threshold voltage of the diodes under forward bias, induced signals in the structure are rectified by the diodes causing a reverse DC bias to build up across the diodes on the top and bottom half of the unit cell (bottom of Fig. 3.11). This reverse bias decreases the capacitance, which in turn shifts the magnetic resonance up in frequency reducing the transmission through the structure (top of Fig. 3.11). As the induced voltage is increased further a sudden decrease in transmission is observed as a function of applied voltage (Fig. 3.12). This effect is similar to the bistability in varactor-loaded split-ring resonators, reported by several authors [49, 50]. Initially this transition is limited to the first few layers of the structure, which is evidenced in the significantly smaller voltage drop across the diode in the seventh cell (bottom of Fig. 3.12). Significantly higher voltage is then required to induce this transition in the remaining layers (Fig. 3.13) and allow the structure to reach the transmission minimum predicted in Fig. 3.9. This effect can be evidenced by the larger relative voltage drop in cell 7, compared to cells 1 and 4 (bottom of Fig. 3.13). Therefore simply by changing the diodes loading the structure the response of this metamaterial to incident power can effectively be inverted, without any additional modifications.

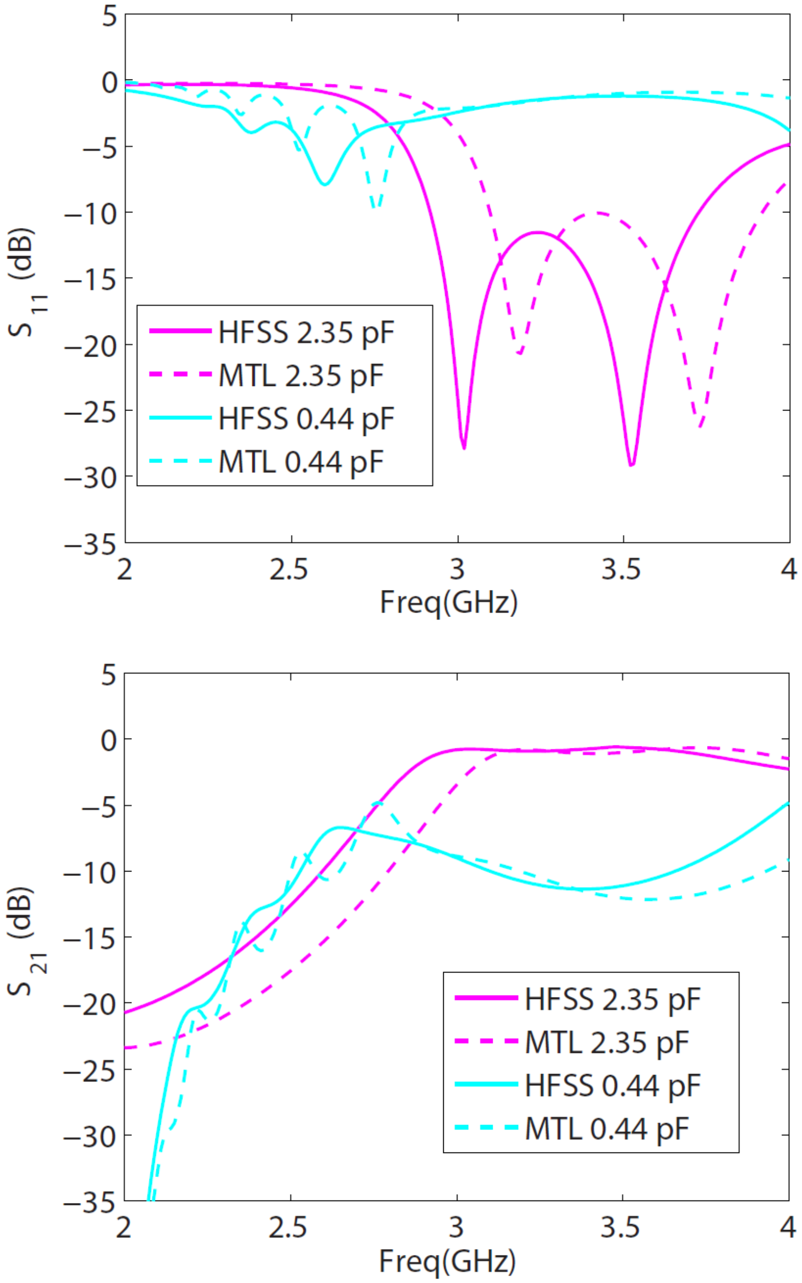

Figure 3.9- Comparison between simulated high power (cyan) and low power (magenta) reflection spectra for the varactor loaded broadband switching nonlinear metamaterial structure shown in Fig.5. Results obtained from HFSS (solid) show good agreement with those obtained from multiconductor transmission line analysis.

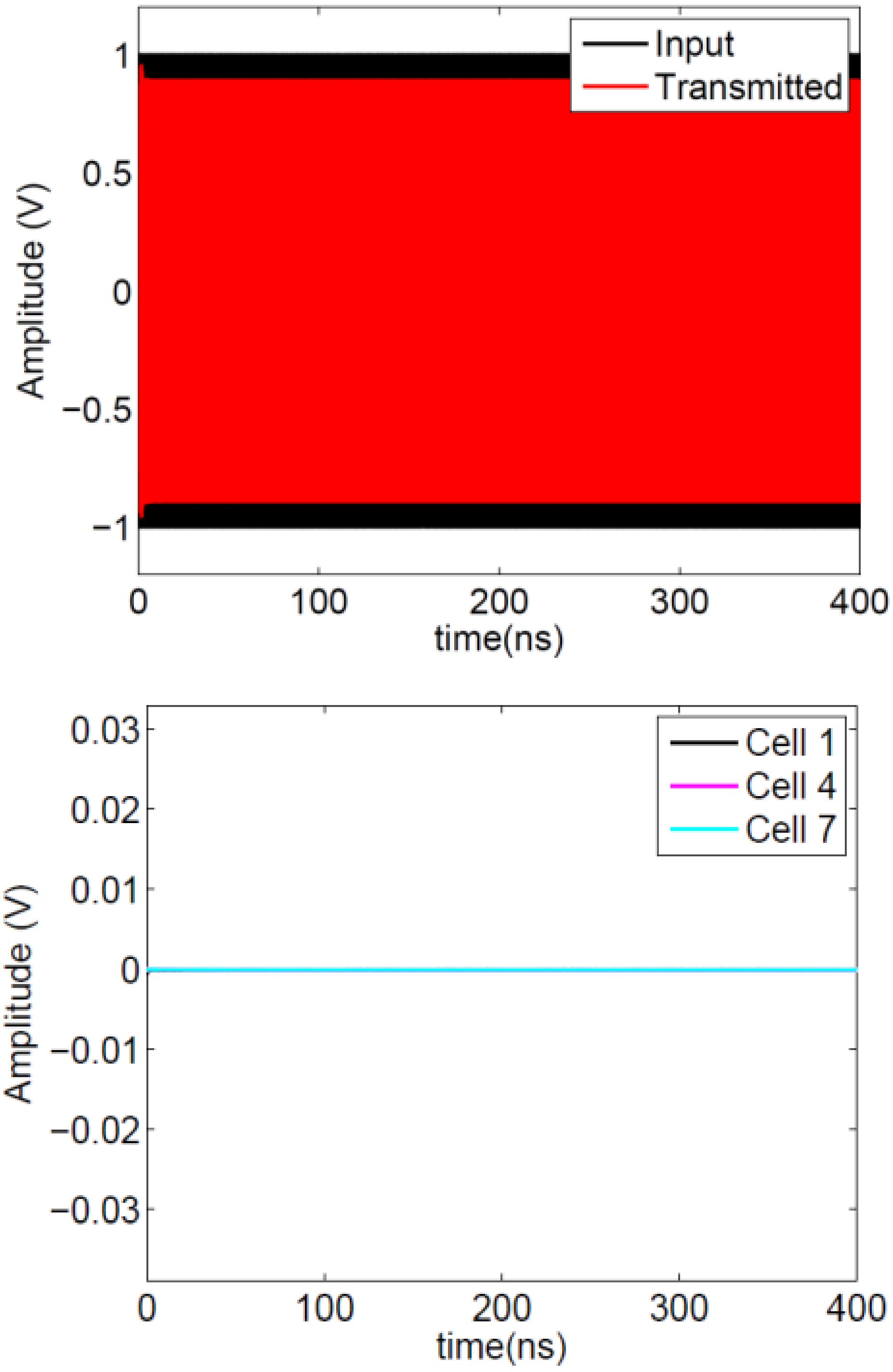

Figure 3.10- Simulated time domain response of varactor loaded broadband switching metamaterial obtained using nonlinear multiconductor transmission line analysis. Top shows transmitted (red) signals for a 3.4 GHz input (black) signal at 4 dBm. The low pass filtered voltage drop across a single diode is also shown (left) at each power level in the first (black), fourth (magenta), and seventh (cyan) element in the transmission line.

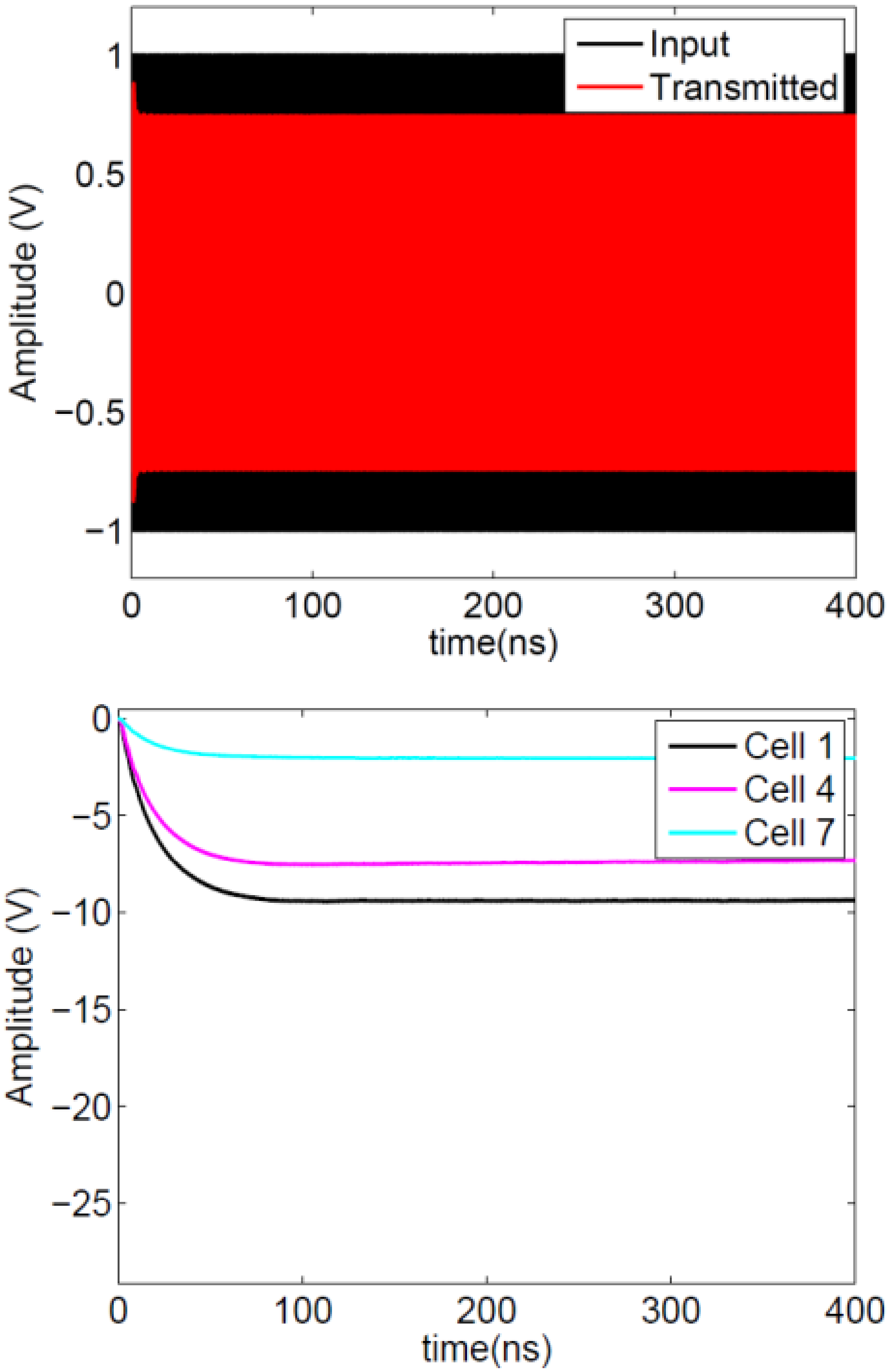

Figure 3.11- Simulated time domain response of varactor loaded broadband switching metamaterial obtained using nonlinear multiconductor transmission line analysis. Top shows transmitted (red) signals for a 3.4 GHz input (black) signal at 39.5 dBm. The low pass filtered voltage drop across a single diode is also shown (left) at each power level in the first (black), fourth (magenta), and seventh (cyan) element in the transmission line.

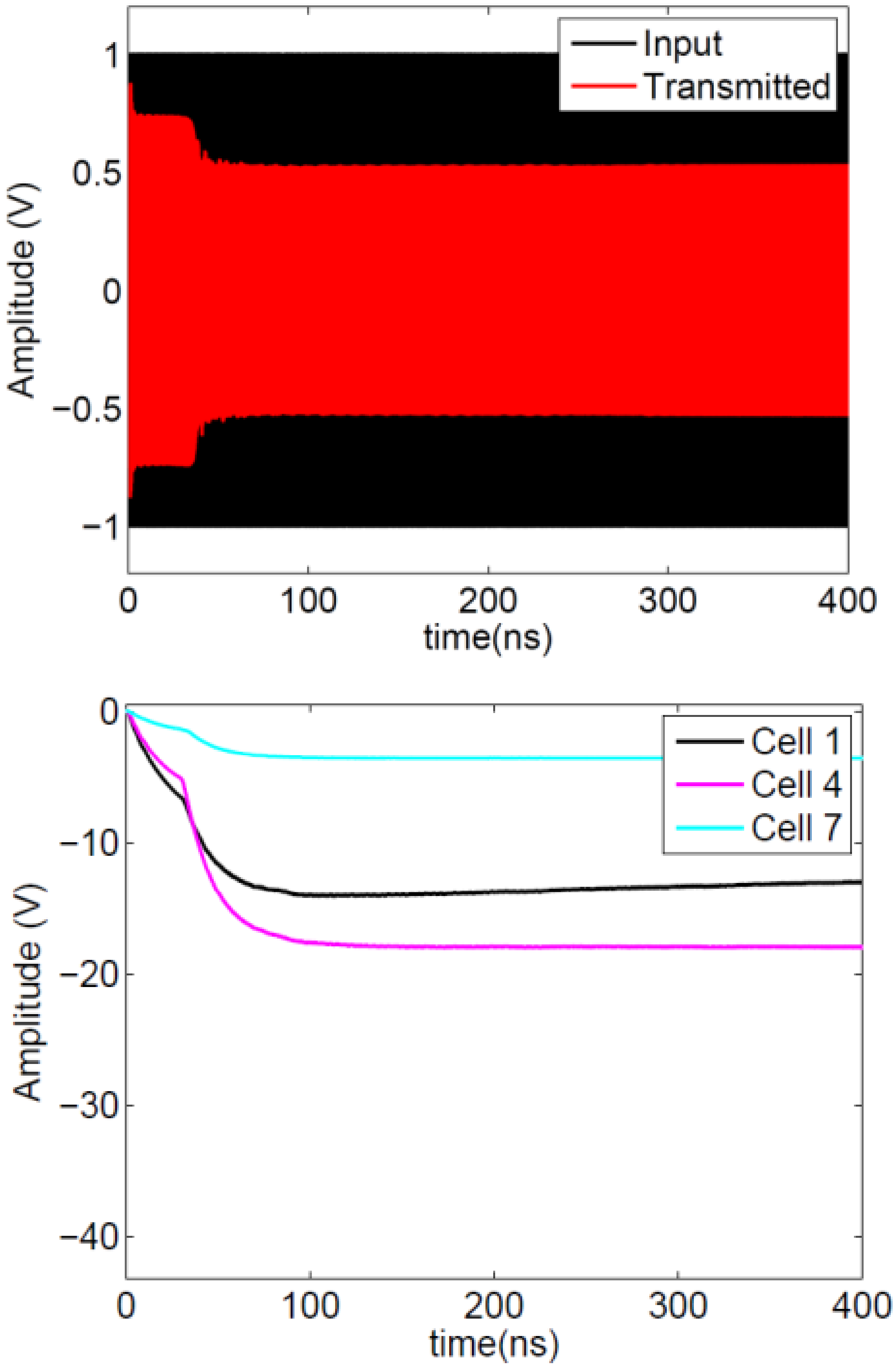

Figure 3.12- Simulated time domain response of varactor loaded broadband switching metamaterial obtained using nonlinear multiconductor transmission line analysis. Top shows transmitted (red) signals for a 3.4 GHz input (black) signal at 39.7 dBm. The low pass filtered voltage drop across a single diode is also shown (left) at each power level in the first (black), fourth (magenta), and seventh (cyan) element in the transmission line.

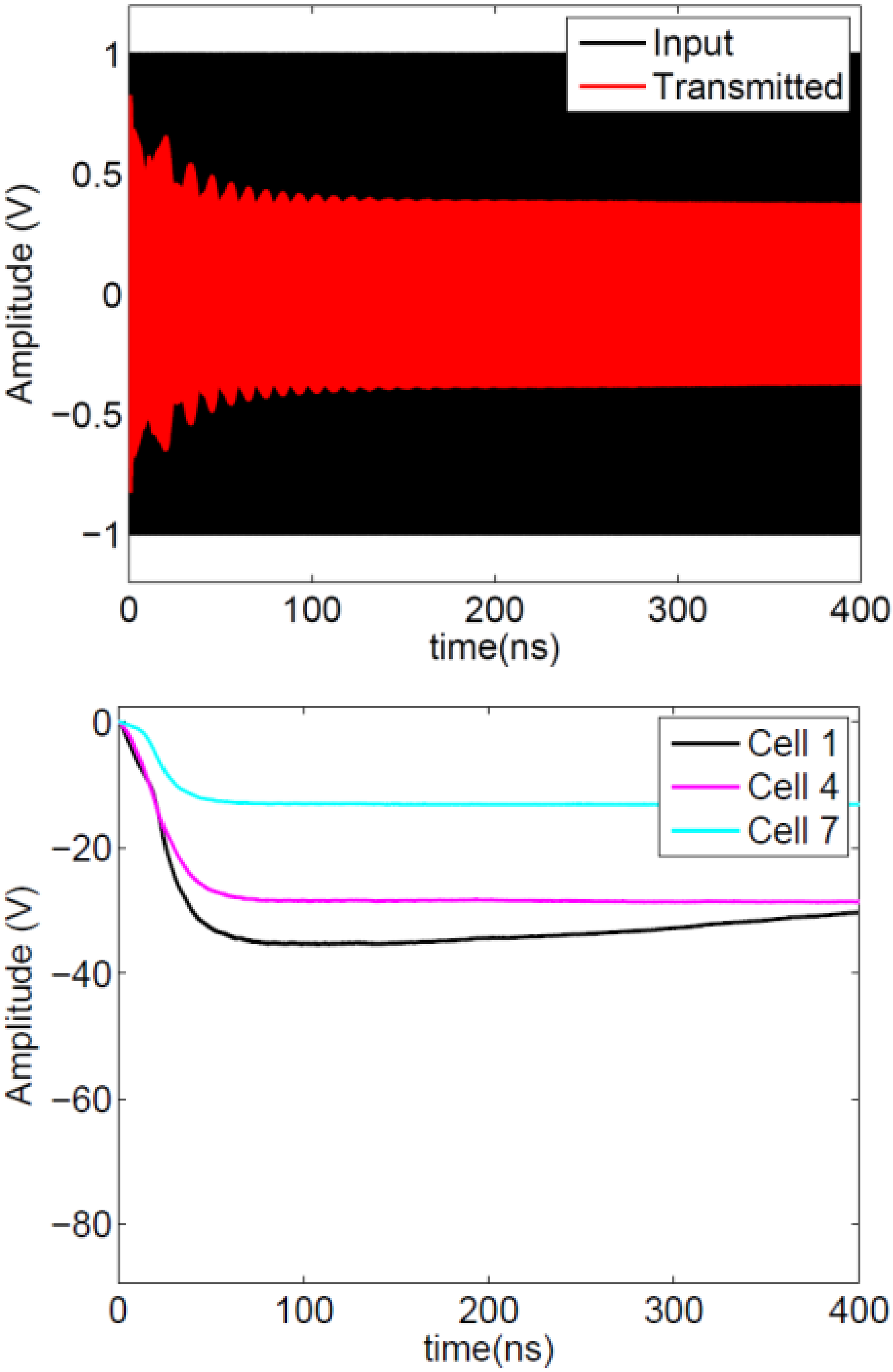

Figure 3.13- Simulated time domain response of varactor loaded broadband switching metamaterial obtained using nonlinear multiconductor transmission line analysis. Top shows transmitted (red) signals for a 3.4 GHz input (black) signal at 42 dBm. The low pass filtered voltage drop across a single diode is also shown (left) at each power level in the first (black), fourth (magenta), and seventh (cyan) element in the transmission line.

Chapter 4 -Experimental Demonstration of Broadband Switching Metamaterials

The broadband switching metamaterial structures discussed in the previous chapter enable the effective material parameters of a composite medium to be changed from broadband reflectivity to broadband transparency depending on the power in the incident wave. In practice, these structures would be implemented by arraying the fundamental unit cell into a large lattice spanning many wavelengths (Fig. 4.1). Because this lattice must be finite in size, both the coverage and the boundary conditions at the edges of the structure are important in determining how the characteristics of this structure affect the propagation of an incident wave. For these reasons, as well as economy, many authors have previously demonstrated self-biasing metamaterial structures on a relatively small scale using parallel plate waveguide [59, 43]. As seen in the previous chapter, terminating the top and bottom of the metamaterial unit cell can be an effective way of simulating infinite periodicity in the direction of the electric field. The primary issue with metamaterial experiments performed in parallel plate waveguide, is that field is not confined in horizontal (i.e. magnetic) direction creating spreading and

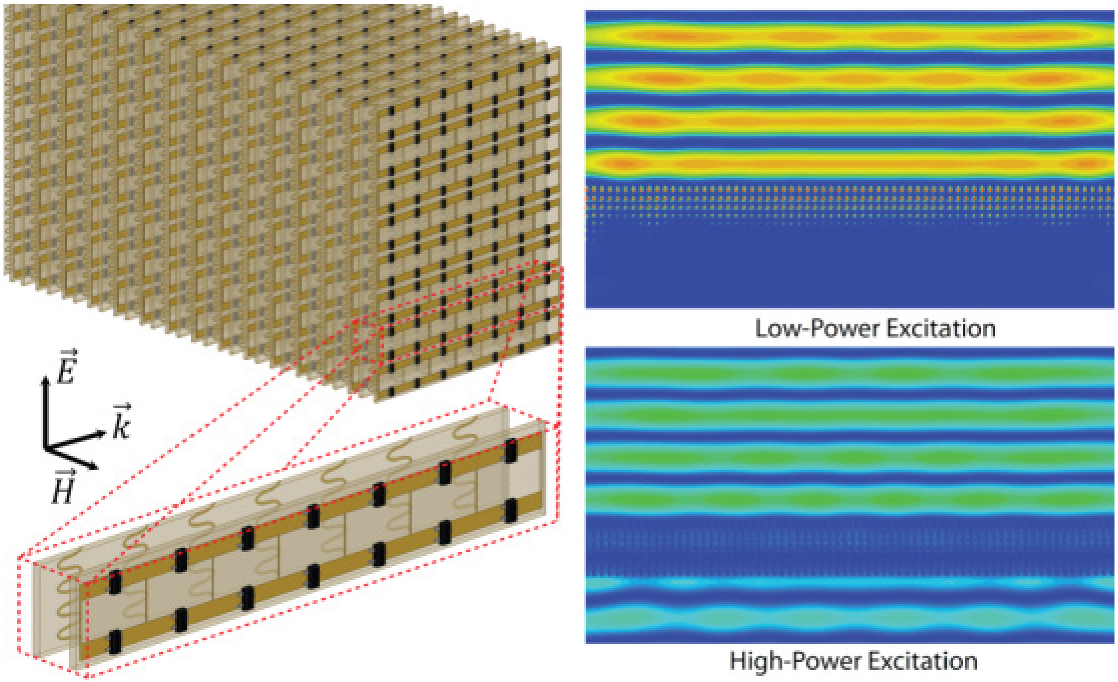

Figure 4.1- A cartoon representation of a semi-infinite broadband switching metamaterial slab is shown on the left with a single row enlarged to show detail. The resulting fields maps on the right depict low- and high-power excitations (top and bottom, respectively) normalized to their incident amplitude.

diffraction of the incident wave, which requires a substantially large lattice for many experiments. To circumvent this complication, measurements can be performed in rectangular waveguide which places conducting boundary conditions on both the vertical and horizontal planes [38, 40]. While propagation in a rectangular waveguide is by definition a different mode of propagation than the TEM mode realized in free space, for many structures, measurements made in rectangular waveguide are comparable to those in free space over some range of frequencies. In this chapter, waveguide measurements of two broadband switching metamaterials which were introduced in the previous chapter, one loaded with dual anti-parallel Schottky diodes and one loaded with single varactor diodes will be discussed.

Schottky-Loaded Broadband Switching Metamaterial Experiments

When loaded with dual anti-parallel Schottky diodes, the broadband switching metamaterial discussed in Chapters 2&3 is capable of switching from a broadband reflective state for low power incident radiation to a broadband transparent state for high power incident radiation. To validate the performance predicted in the full wave simulation and multiconductor transmission line analysis an experimental demonstration of this wideband nonlinear metamaterial slab was conducted in S-band waveguide (Fig. 4.2). A custom section of WR-284 waveguide (bottom of Fig. 4.3) was built to hold nine magnetic and nine electric boards in the waveguide's cross section. The top of Fig. 4.3 shows the wideband nonlinear metamaterial placed inside of this S-band waveguide apparatus. Transmission measurements of the slab were made by connecting 6in waveguide straight sections followed by waveguide-to-coax adapters to the part and measuring S_{21} using a vector network analyzer (VNA) and external amplifier. For reflection measurements, one of the waveguide straight sections was replaced with a directional coupler where port 2 of the VNA was connected to the coupled port. A 50-Ω waveguide load was placed after the metamaterial structure to ensure proper termination. All boards were etched on a 1E/1E copper laminate of RO4003 (left-side of Fig. 4.4). Once etched Skyworks SMS7621-075LF diodes were placed in the gaps of the magnetic elements using solder paste and a reflow oven (right-side of Fig. 4.4). These diodes were chosen for their low capacitance and high resistance in the off state and its low on-state resistance. The electric elements were grounded to the waveguide. This was achieved by adding metal fingers to the inductive traces which extended above the waveguide and were grounded using copper tape.

(a) Transmission Setup

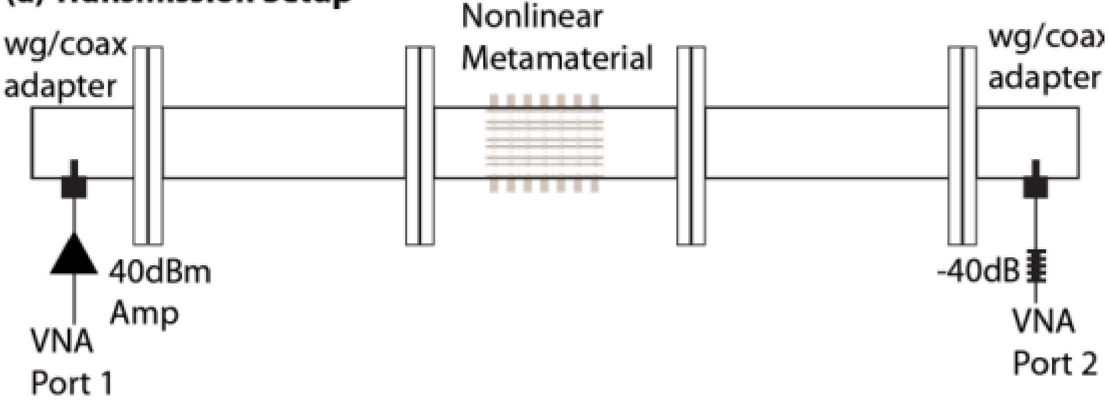

(b) Reflection Setup

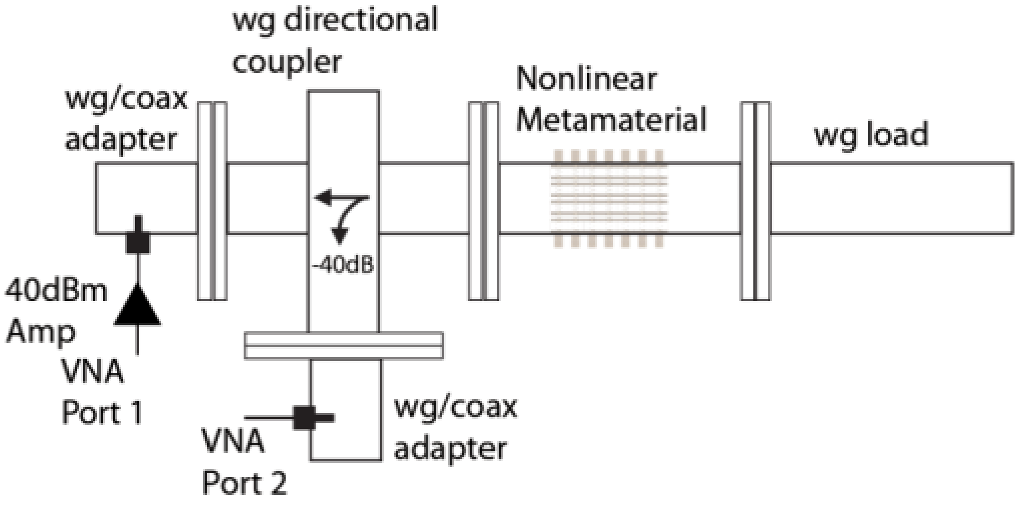

Figure 4.2- Schematic diagram of experimental setup used to measure (a) transmission and (b) reflection characteristics of broadband nonlinear metamaterial structure.

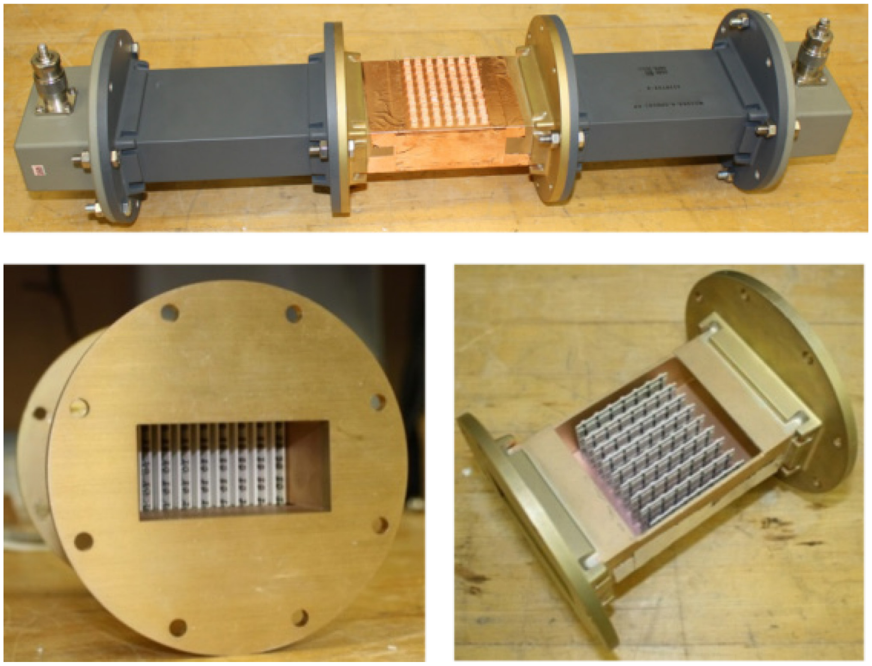

Figure 4.3- Photograph of Schottky-loaded broadband switching metamaterial in waveguide measurement apparatus (top). Bottom shows the metamaterial in the custom section of WR-284 from a front side view (left) and a top view of magnetic boards only with top plate remove (right).

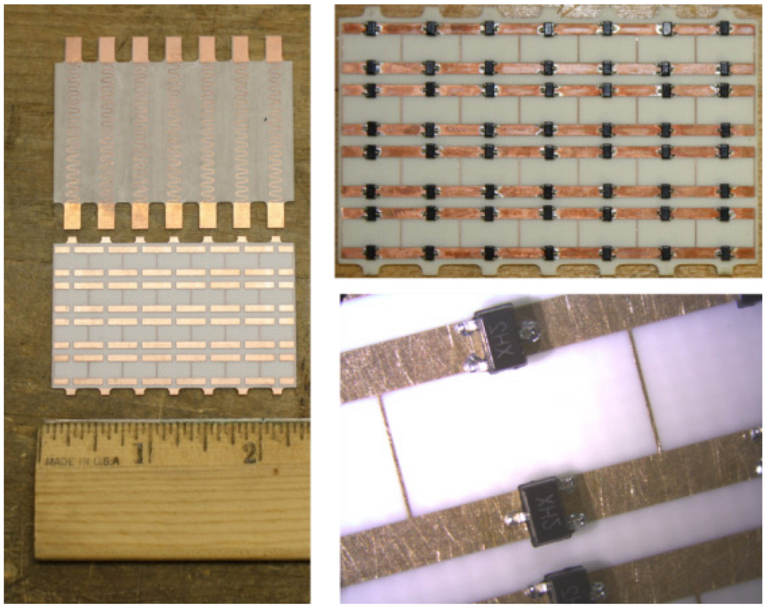

Figure 4.4- Photograph of electric and magnetic boards before (left) and after (right) diode placement. A zoomed in view of magnetic boards showing the configuration of the Skyworks SMS7621-075LF diodes.

Using the aforementioned measurement apparatus, reflection and transmission measurements were made at incident powers of 0 dBm, 10 dBm, 20 dBm, 30 dBm, and 40 dBm (Fig. 4.5). At low incident powers (<10 dBm) this structure exhibited broadband reflectivity (S_{11}>-1 dB) from 3.1 GHz-4 GHz. When excited with high power (40 dBm) this broadband reflectivity dropped by approximately 10 dB over a 625-MHz (18%) bandwidth centered at 3.43 GHz and by 3 dB over a > 30% bandwidth centered at 3.6 GHz with a maximum decrease of 42.9 dB at 3.166 GHz (Fig. 4.5). Furthermore, at 40 dBm the maximum power loss in the slab is 1.1 dB with an average loss of 0.7 dB and a minimum of 0.55 dB across the 10 dB bandwidth (Fig. 4.6). These values suggest that once the diodes are fully conducting, the majority of the reduction in reflected amplitude is due to transmission and not to absorption. Contrarily above 10 dBm and below 40 dBm the structure can exhibit significant absorption with an average value of 6.5 dB and 4.8 dB observed at 20 dBm and 30 dBm incident powers, respectively.

Since the waveguide used in this experiment supports TE_{10}propagation rather than TEM, Fig. 4.5 cannot be directly compared to Fig. 2.10. As a result, new simulations were performed in CST with the boundary conditions modified to represent a WR-284 waveguide. Additionally, we used two diodes packaged in a single SC-70 package, rather the two antiparallel SC-79 packages which we had originally measured. Unfortunately, the larger SC-70 package increased the total capacitance of the diodes to 0.45 pF. The updated results of these simulations are compared to the measurements in Fig. 4.7 and the agreement is quite good.

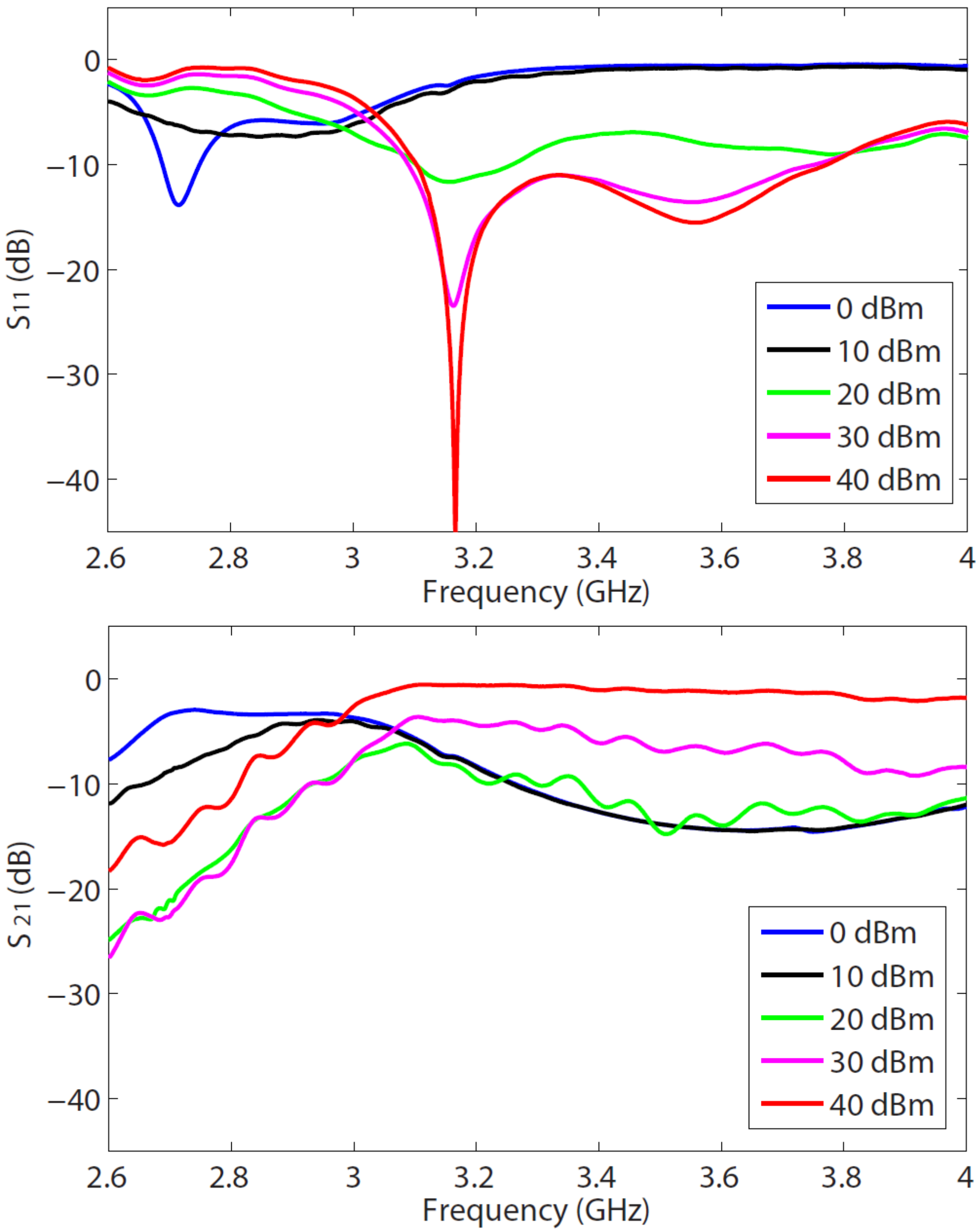

Figure 4.5- Reflection (top) and transmission (bottom) measurements of the broadband nonlinear metamaterial structure measured in S-band waveguide at various power levels.

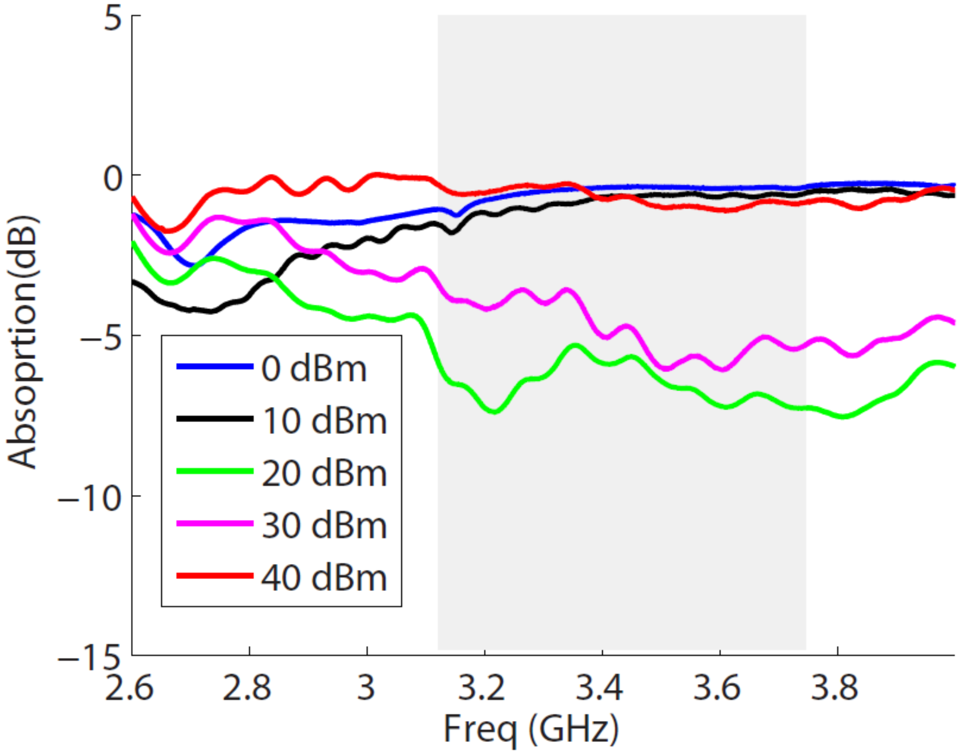

Figure 4.6- Plot of measured loss through Schottky loaded broadband switching metamaterial at various power levels. The 10 dB bandwidth of this structure is highlighted in gray.

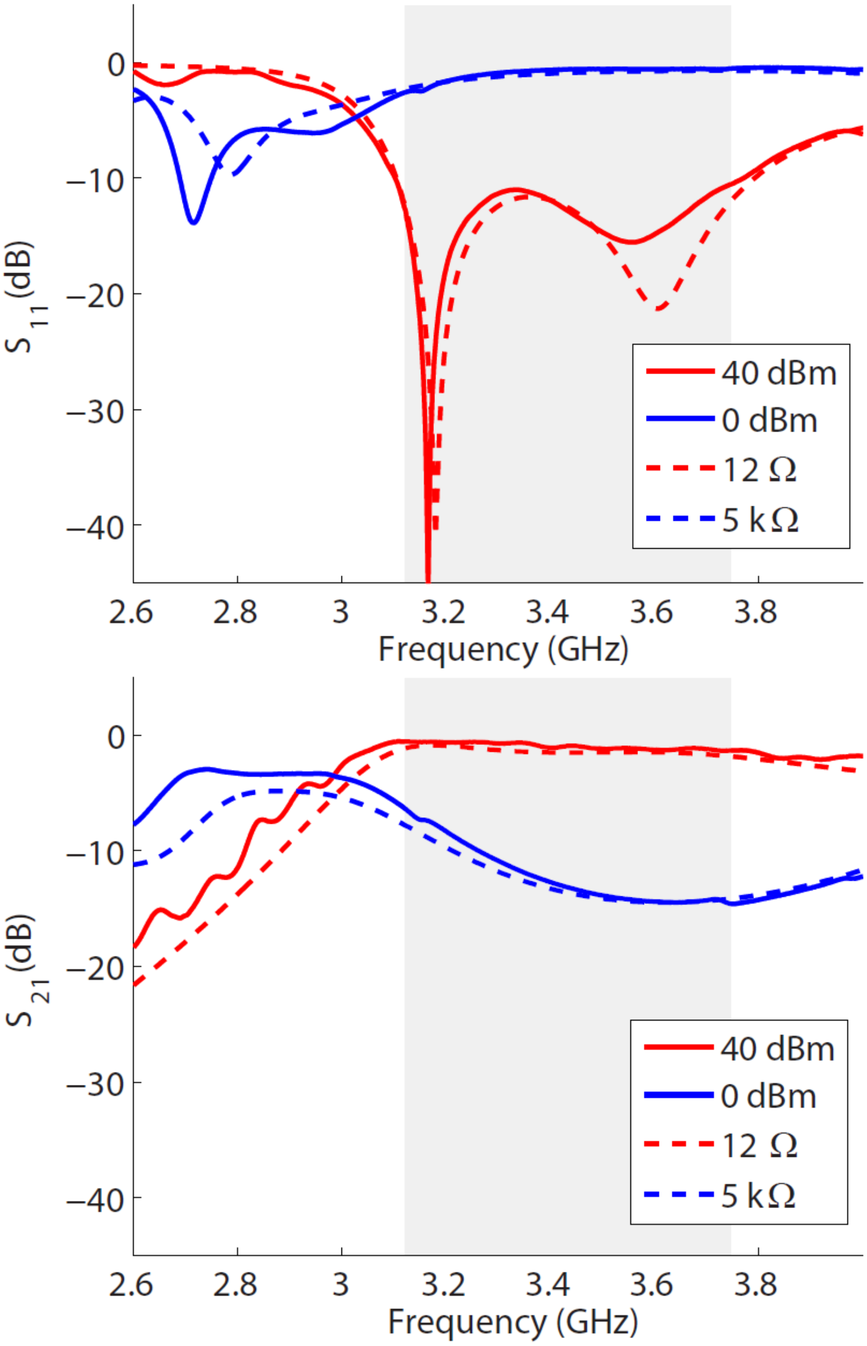

Figure 4.7- Simulated (dashed lines) and measured (solid lines) reflection (top) and transmission (bottom) coefficients of the wideband seven cell nonlinear metamaterial structure placed inside a WR-284 waveguide. The high and low power states of the diodes were simulated by changing the resistance values. The 10 dB bandwidth of this structure is highlighted in gray.

Pulsed Measurements

In addition to the frequency domain measurements discussed above, pulsed time-domain measurements of this Schottky-loaded broadband switching metamaterial structure were made to validate the temporal switching dynamics predicted by the nonlinear multiconductor analysis shown in Fig. 3.6. As before these measurements were made in WR-284 waveguide using a similar measurement setup (Fig. 4.8). A 25-GS/s Tektronix 70002 arbitrary waveform generator connected to a 54-dBm amplifier, was used to generate a 100-ns pulsed RF signal at 3.2 GHz with a 1ns rise/fall time at one port of the waveguide. The transmitted signal through this structure was measured at the opposite port of the waveguide using a Tektronix DPO70604 25-GS/s oscilloscope. A circulator with a 50-Ω load was used at the input port of the waveguide to isolate the amplifier. Reflected signals were measured by interchanging the 50-Ω load on the circulator and the oscilloscope. Figure 4.9 shows the signal measured from this experiment compared with results obtained from the nonlinear multiconductor transmission line analysis. Signals measured from this experiment demonstrate a 3-4 ns response time, which is in good agreement with the values predicted from simulation.

(a) Transmission Setup

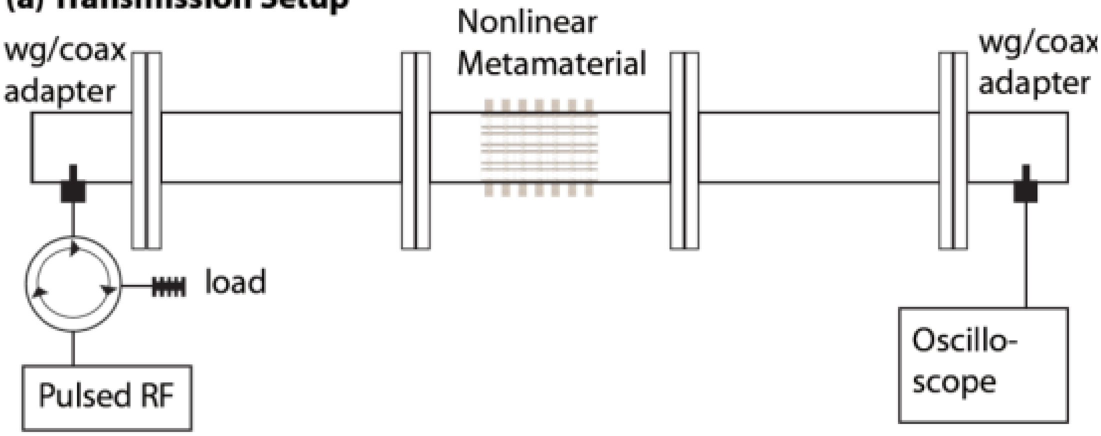

(b) Reflection Setup

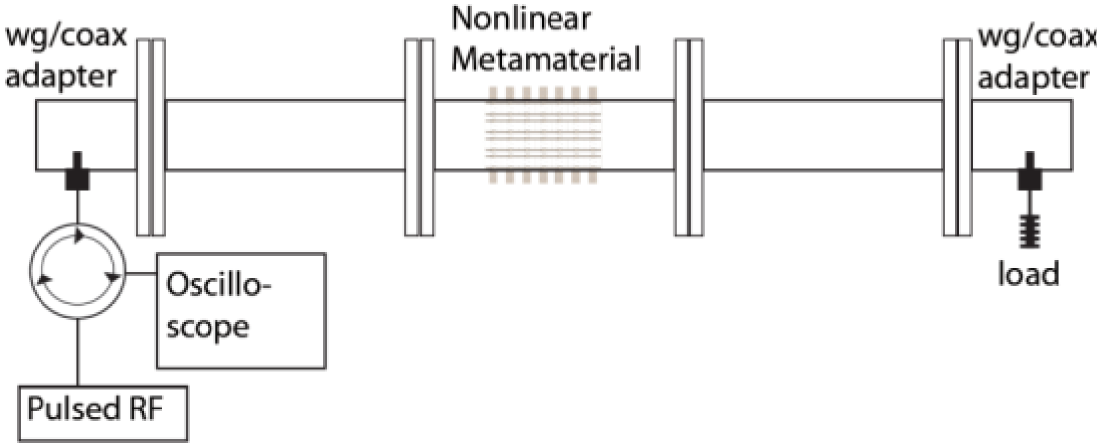

Figure 4.8- Schematic diagram of experimental setup used to measure transient (a) transmission and (b) reflection characteristics of broadband nonlinear metamaterial structure.

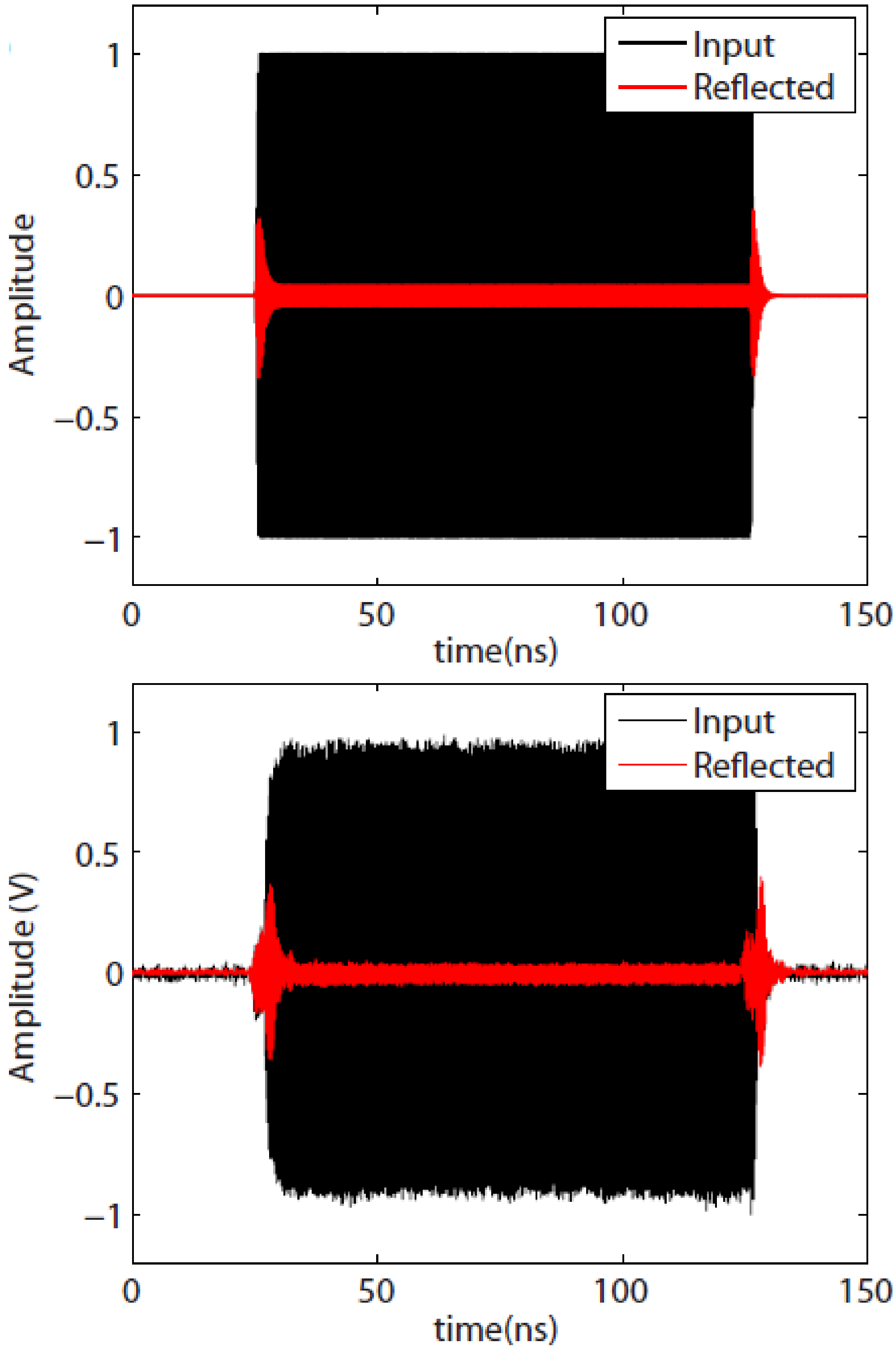

Figure 4.9- Simulated (top) and measured (bottom) response of broadband switching metamaterial to an input 100-ns RF pulse at 3.2 GHz, with a 1-ns rise/fall time.

Varactor-Loaded Broadband Switching Metamaterial Experiments

When loaded with varactor diodes this broadband switching metamaterial is capable of switching from a broadband transparent state for low power incident radiation to a broadband reflective state for high power incident radiation. This response to incident power is exactly opposite to that demonstrated in the previous section for the Schottky loaded structure. Furthermore as suggested in Chapter 3, the non-symmetric nature of the nonlinearity loading this device causes it to switch in response to a DC bias accumulated between the diodes in the top and bottom of the magnetic elements and not due to the instantaneously induced current. For this reason the transient characteristics of this structure as well as its response to incident power are significantly more complex.

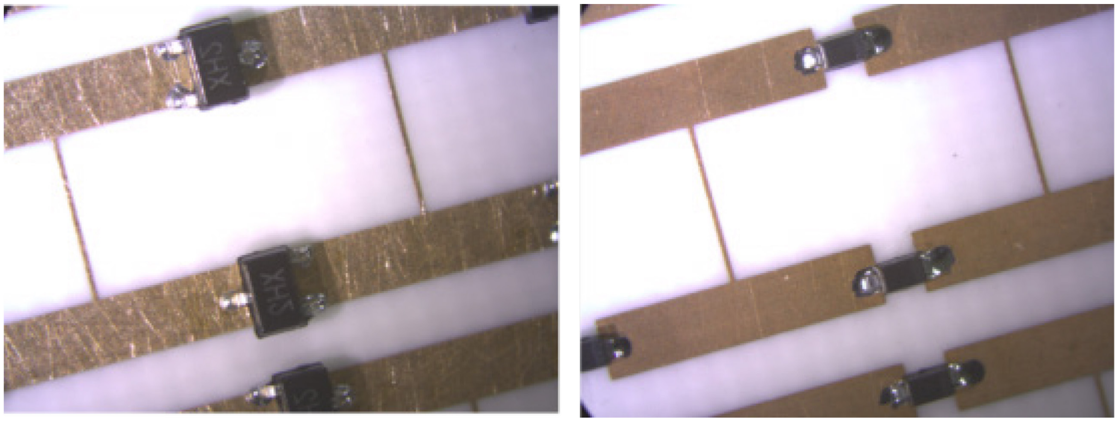

Figure 4.10- Photograph of the Skyworks SMS7621-075LF and SMV1231-079LF diodes mounted on the magnetic elements of the broadband switching metamaterial.

To validate the transient behavior predicted in the last section of Chapter 3, an experimental demonstration of this varactor loaded broadband switching metamaterial was conducted in WR-284 waveguide. The fabrication process for these boards was the same as that described in the previous section except the SMS7621-075LF diodes were exchanged with the SMV1231-079LF model (Fig. 4.10). Each of these diodes was oriented in the same direction in the top and bottom half of the unit cell. Boards were then mounted in a custom section of WR-284 which was connected on either end to waveguide straight sections and coaxial transitions. Using a vector network analyzer with an output power of 0 dBm, S_{11} and S_{21} for this structure were measured from 3-4 GHz. For comparison, additional simulations were run in CST Microwave Studio using waveguide boundary conditions and the low power lumped element equivalents for the SMV1231 discussed earlier in this section. These measurements show generally good agreement with simulation (Fig. 4.11).

The transient switching behavior of this structure was investigated using the same experimental setup shown in Fig. 4.8. Figures 4.12-4.15 show the measured signals transmitted through the broadband switching metamaterial for a pulsed RF input centered at 3.4 GHz at four different power levels. For low input powers, good transmission is observed throughout the duration of the pulse, with an insertion loss of 1.15 dB. As the incident power is increased a slight reduction in transmission of 0.8 dB is observed, this is similar to the intermediate switching behavior observed in Fig. 3.11. At 43.6 dBm an abrupt decrease in transmission is observed. This abrupt drop in transmission most likely corresponds to scenario where all seven cells of the structure have been activated (Fig. 3.13) and not the significantly more abrupt transition observed in Fig. 3.12 which occurs when just the initial cells in the structure activate. This effect can be further evidenced by the minimal drop in power (0.2dB) observed at 46 dBm (Fig. 4.15).

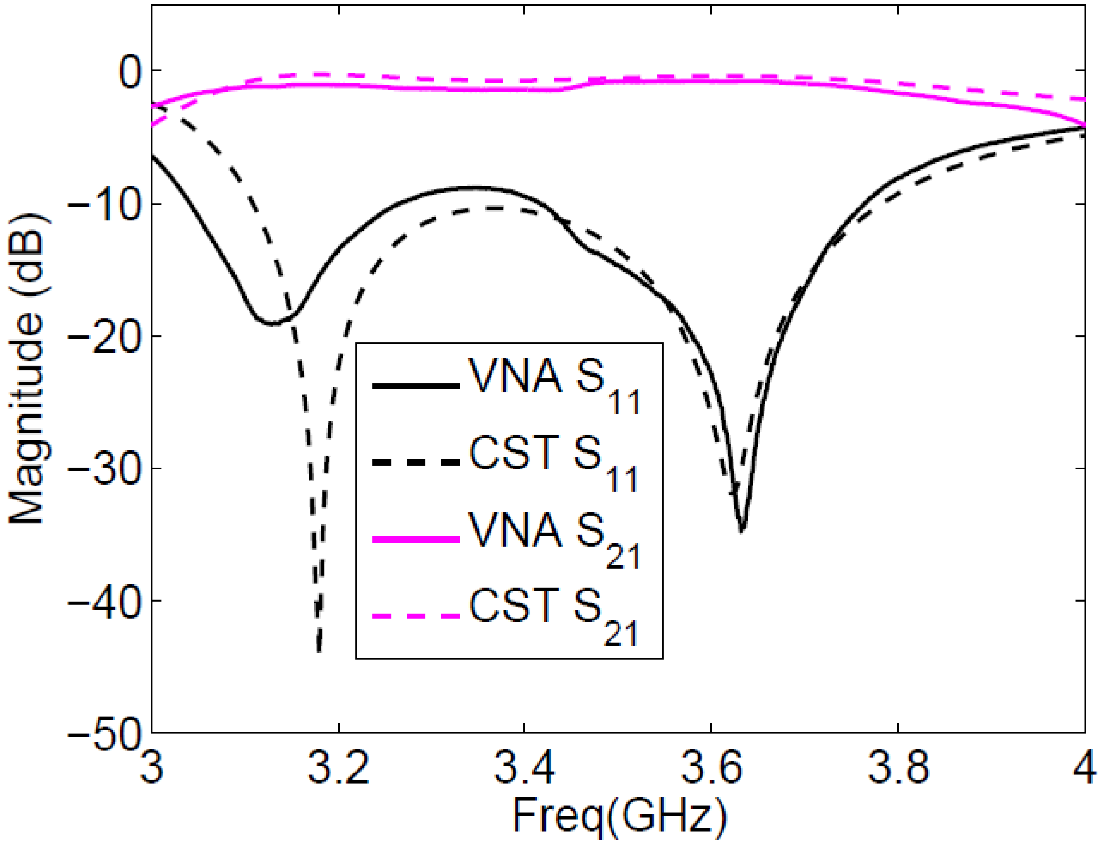

Figure 4.11- Comparison between measured (solid) and simulated (dashed) S-parameters for the varactor-loaded broadband switching nonlinear metamaterial structure at low power. Results obtained from CST (solid) show good agreement with those obtained from measurements performed in WR-284.

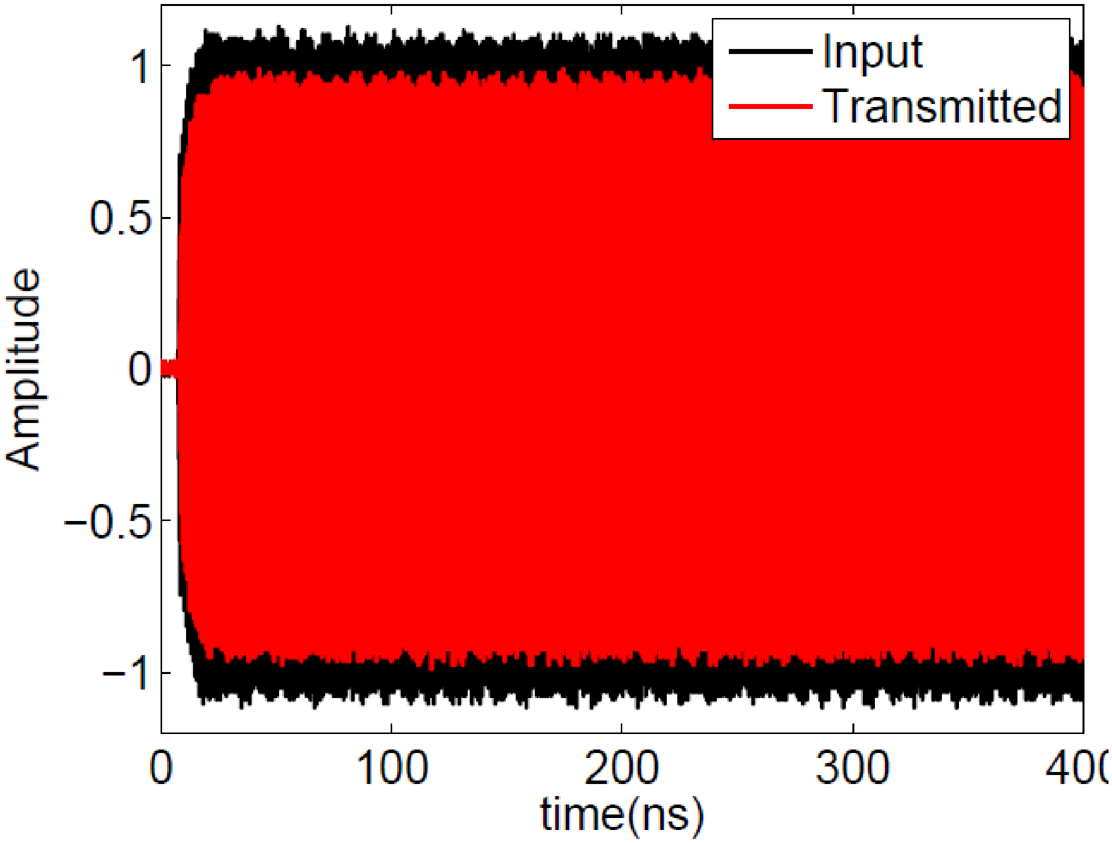

Figure 4.12- Measured time domain response of varactor loaded broadband switching metamaterial in WR-284 waveguide. A transmitted (red) signal for a 3.4 GHz input (black) signal at -5 dBm is shown. Both input and transmitted waveforms are normalized to the peak input voltage.

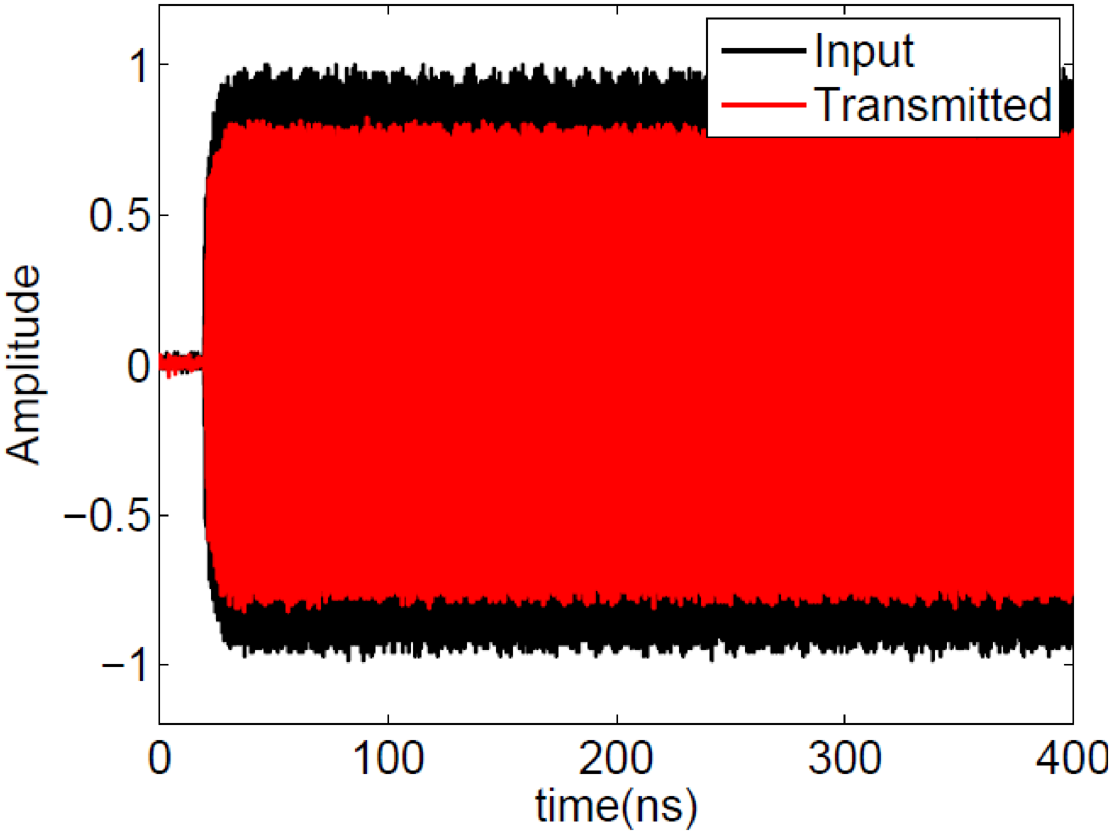

Figure 4.13- Measured time domain response of varactor loaded broadband switching metamaterial in WR-284 waveguide. A transmitted (red) signal for a 3.4 GHz input (black) signal at 39.2 dBm is shown. Both input and transmitted waveforms are normalized to the peak input voltage.

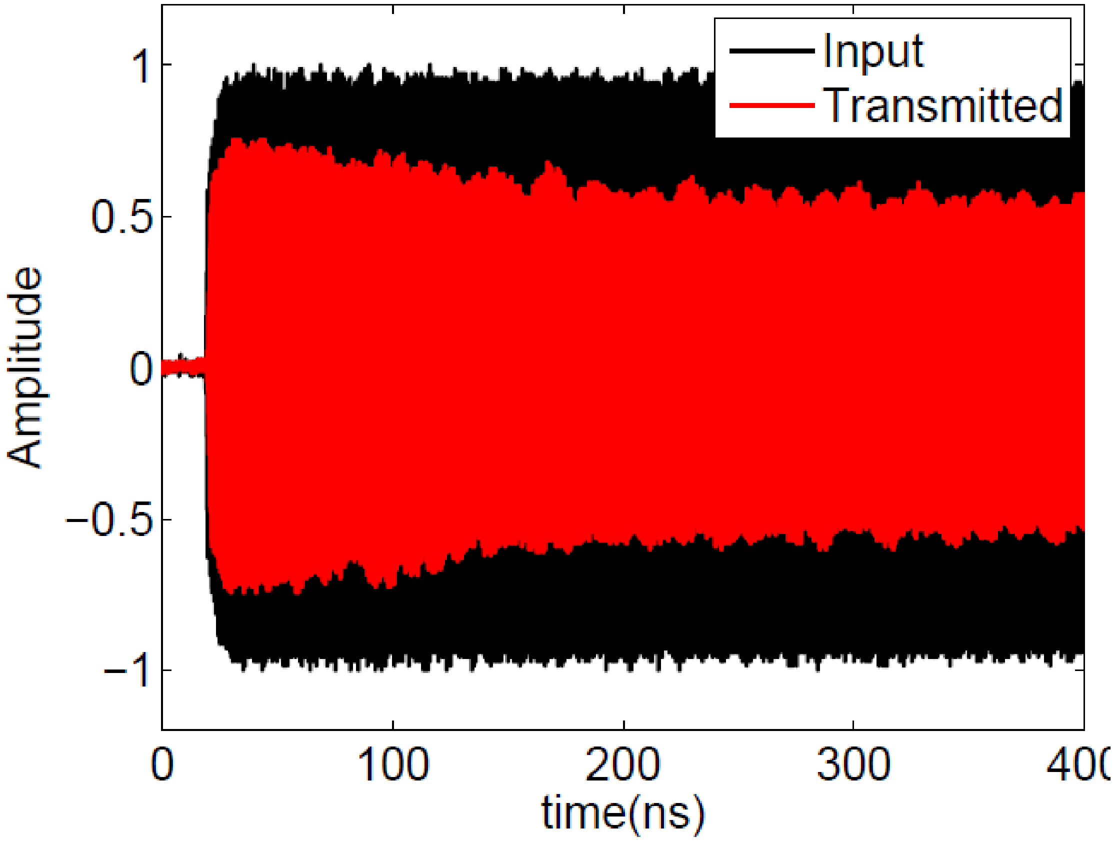

Figure 4.14- Measured time domain response of varactor loaded broadband switching metamaterial in WR-284 waveguide. A transmitted (red) signal for a 3.4 GHz input (black) signal at 43.6 dBm is shown. Both input and transmitted waveforms are normalized to the peak input voltage.

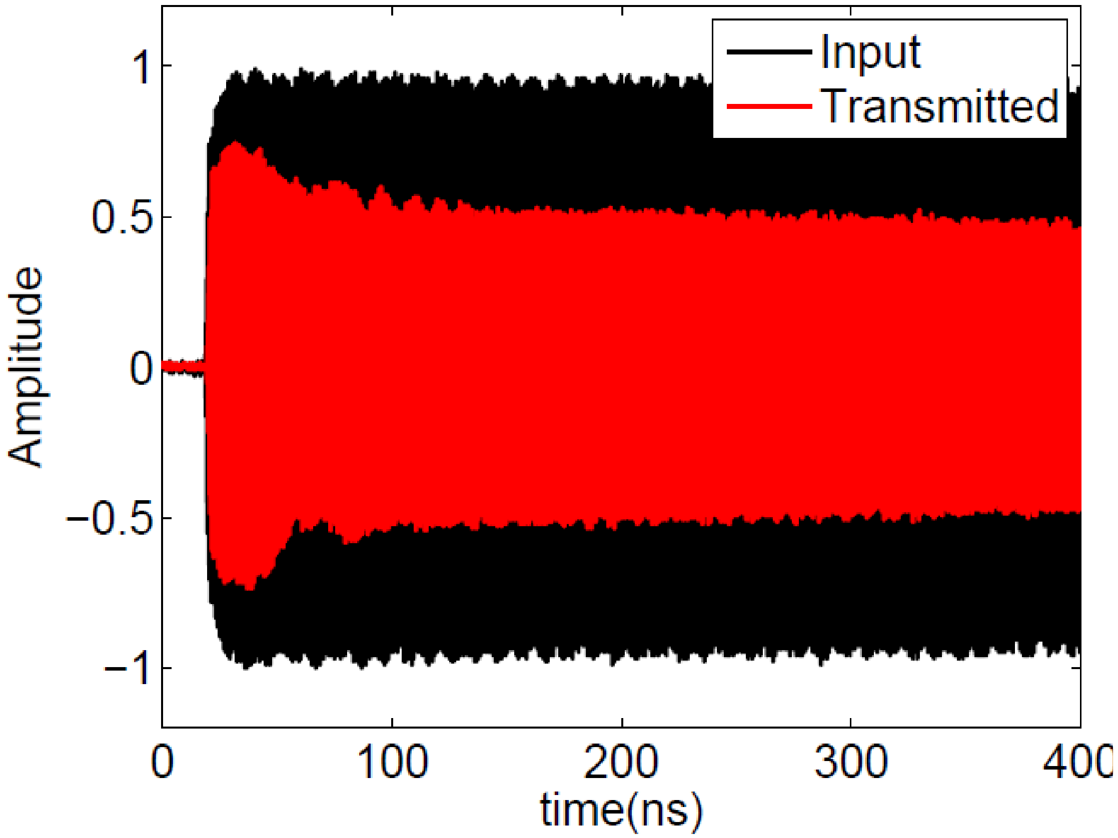

Figure 4.15- Measured time domain response of varactor loaded broadband switching metamaterial in WR-284 waveguide. A transmitted (red) signal for a 3.4 GHz input (black) signal at 46 dBm is shown. Both input and transmitted waveforms are normalized to the peak input voltage.

Once enough power has been applied to this structure over a sufficient period of time the reverse bias built up across the varactors will reach steady state. Frequency dependent transmission and reflection measurements of this structure at steady state were made by replacing the pulsed RF source and oscilloscope in Fig. 4.8 with a vector network analyzer and external amplifier operating with an output power of 43 dBm and a sweep time of 5.5 ms (Fig.4.16). Due to the large reflected power in this experiment a high power circulator was required, thus limiting the frequency range in these experiments to 2.9 GHz-3.7 GHz. In comparison with Fig.4.11, these measurements demonstrate a 3 dB drop in transmission from 3.05 GHz to 3.7 GHz with a maximum decrease in transmission of 8.5 dB at 3.47 GHz. Furthermore these measurements show good agreement with simulations performed in CST.

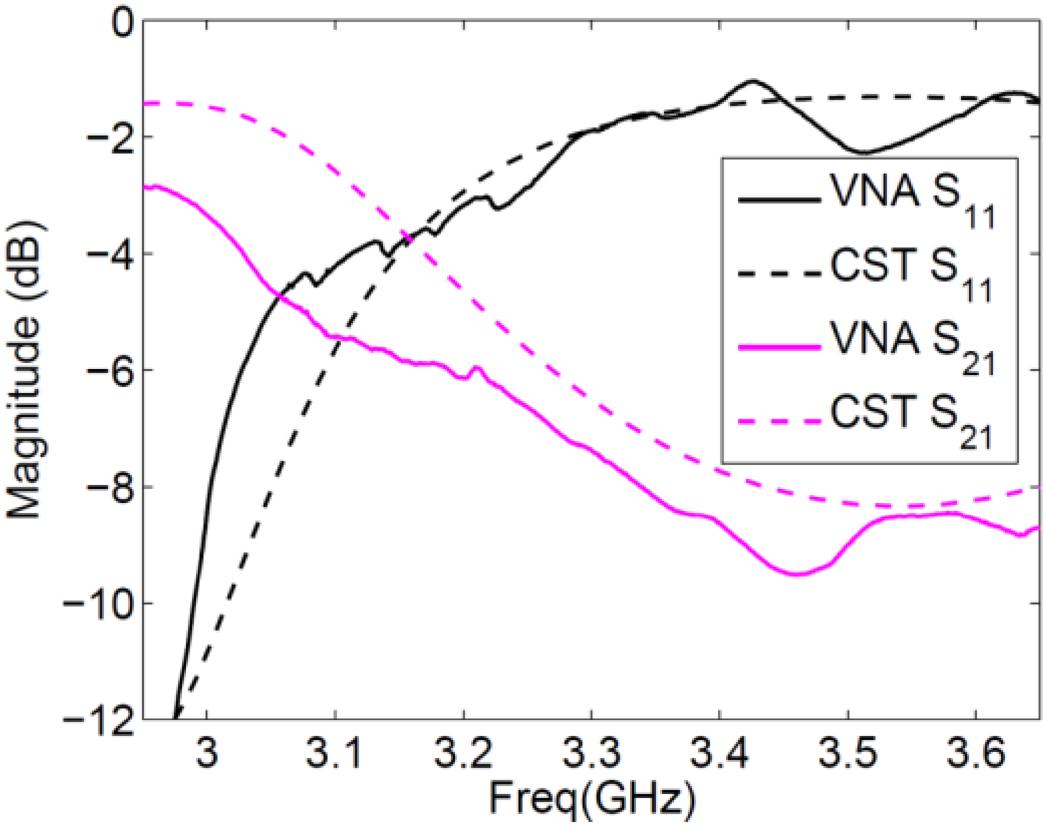

Figure 4.16- Reflection (black) and transmission (magenta) measurements of varactor loaded broadband switching metamaterial measured using vector network analyzer with an input power of 43 dBm. These experiments (solid) show good agreement with simulations (dashed) performed in CST.

Chapter 5 -Improved Time-Reversal Based Beamforming Using a Self-Biasing Switch

Distributed self-biasing structures such as those discussed in the previous chapters are particularly useful in applications where the properties of an electromagnetic wave need to be altered in space before it is received or converted into a confined mode in a transmission line. For applications such as high power limiting and field confinement this is especially true, as these self-biasing metamaterials allow processing of high power electromagnetic signals in space where the power density is lower. While the self-biasing metamaterial structures discussed in the previous chapters attempt to massively array nonlinear devices on a scale that is far less than the incident wavelength, this same concept can be useful even if the spacing between the nonlinear devices is quite large. In this chapter, the application of discrete self-biasing switches to improve the performance of a beamforming system will be discussed. Unlike traditional ultra-wideband beamformers, this system uses a single input channel fed into a reverberant cavity to control the delay and amplitude of pulses at various output channels inside the cavity.

This functionality is achieved using a technique known as time-reversal and in this chapter we demonstrate that the artifacts associated with this time-reversal process can be mitigated by implementing simple, passive, and compact self-biasing switches at the output ports of this cavity.

Ultra-wideband Beamforming

Wireless ultra-wideband (UWB) systems utilize short pulses to transmit and receive data for communications, radar, and imaging [60, 61, 62, 63, 64, 65]. Because energy is highly localized in time these systems can achieve higher data rates and better isolation than their narrowband counterparts. In many applications these systems operate with a preferred direction of propagation which requires beamforming. Unlike narrowband systems which use phase shifting to achieve this effect, UWB short pulse arrays use true time delay (TTD) beamforming.

To illustrate the TTD beamforming concept, consider the antenna array shown in Fig. 5.1 [66]. For a planar wavefront incident at an angle θ and consisting of a single frequency (f), the received signal $y(t)$ at the summation port is given by Eq. 5.1 [66],

$$y(t) = \sum_{i=1}^{K} sin\left(2\pi f\left[t + \frac{d_i}{v_1} + \frac{l_i}{v_2}\right]\right) = \sum_{i=1}^{K} sin(2\pi f[t + (T_1)_i + (T_2)_i sin\theta]) \quad (5.1)$$

where d_i is the distance between the i-th element and the summation port and v_1& v_2 are the propagation speeds in transmission medium between the elements and the summation point and free space respectively. By reciprocity Eq. 5.1 guarantees that by transmitting a continuous wave signal from the summation point with an appropriate phase satisfying the condition $(T_1)_i + (T_2)_i sin\theta =$ constant, a planar wavefront can be generated at the output of the array propagating with an angle θ. In this way signals can be received and transmitted by an array of radiating elements with a preferred direction of propagation.

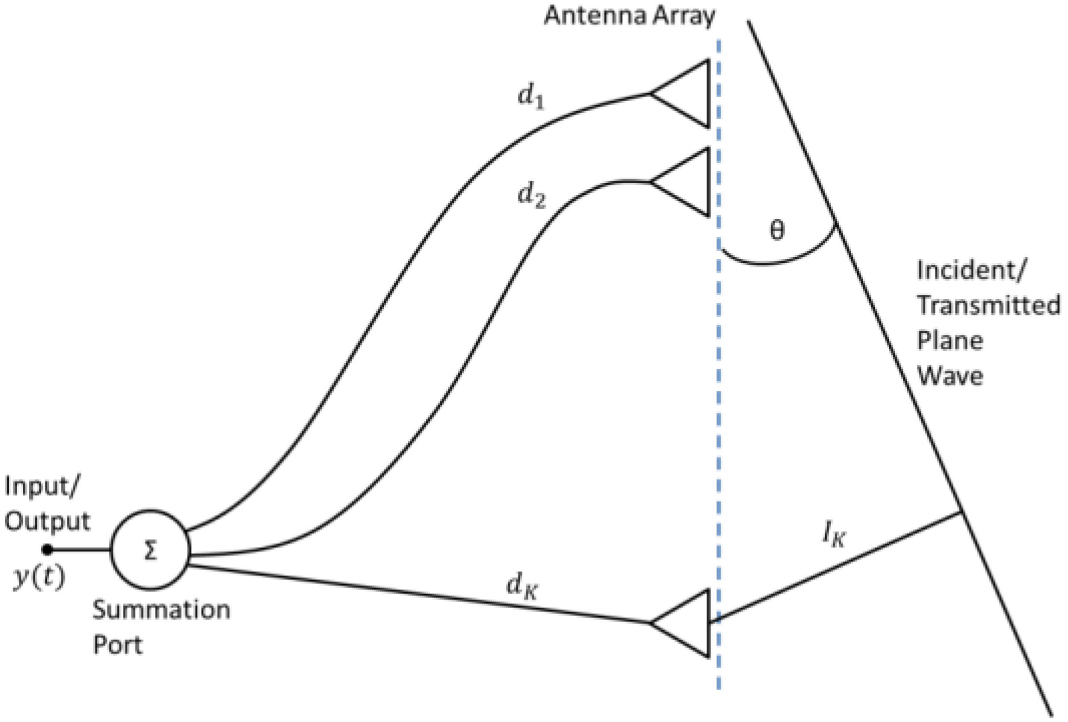

Figure 5.1- Illustration showing typical geometry for TTD beamforming array.

In the case where multiple frequencies are received or transmitted simultaneously through the array, $y(t)$ can be written as a summation over both the elements in the array and the received/transmitted frequencies,

$$y(t) = \sum_{j=1}^{M} \sum_{i=1}^{K} A_j sin\left(2\pi f_j [t + (T_1)_i + (T_2)_i sin\theta]\right) \tag{5.2}$$

$$y(t) = \sum_{j=1}^{M} \sum_{i=1}^{K} A_j sin\left(2\pi f_j [t - \tau_i]\right) \tag{5.3}$$

where A_j is the amplitude of the j-th frequency. By inspection it can be seen that $y(t)$ consists of the sum of K identical signals each represented as a Fourier series. In the limit where these frequencies are closely spaced and cover a sufficiently broad bandwidth, each of these signals can be represented by an arbitrary function $f(t)$ convolved with a time shift operator $\delta(t+\tau_i)$.

$$y(t) = \sum_{i=1}^{K} f(t) * \delta(t+\tau_i) \tag{5.4}$$

Therefore for ultra-wideband phased arrays efficient transmission of an arbitrary function at some angle θ can be achieved by supplying the arbitrary function at the input and subsequently applying an appropriate time-delay to each channel.

Time-Reversal Based Beamforming

One of the primary limitations associated with TTD beamformers such as the one illustrated in Fig. 5.1, is the associated complexity of such networks. In particular these networks require several splitters and variable delay lines to achieve the performance discussed in the previous section. Several authors have proposed that the complexity of such networks can be significantly reduced through a technique known as time-reversal [67, 68, 69]. The basic concept behind this technique is that the convolution of a function and its time-reversed counterpart yields an autocorrelation which is close to a delta-function. Therefore if the channel response *h(t)* between two ports connected by an arbitrary dispersive medium is measured, time-reversed, and retransmitted at either of the ports then an auto-correlated signal $h(t) * h(-t)$ will be received at the opposing port [69]. Furthermore by convolving an arbitrary signal f(t) onto this transmitted time-reversed channel response the dispersive effects of the channel can be mitigated improving the delivery of the arbitrary signal [70].

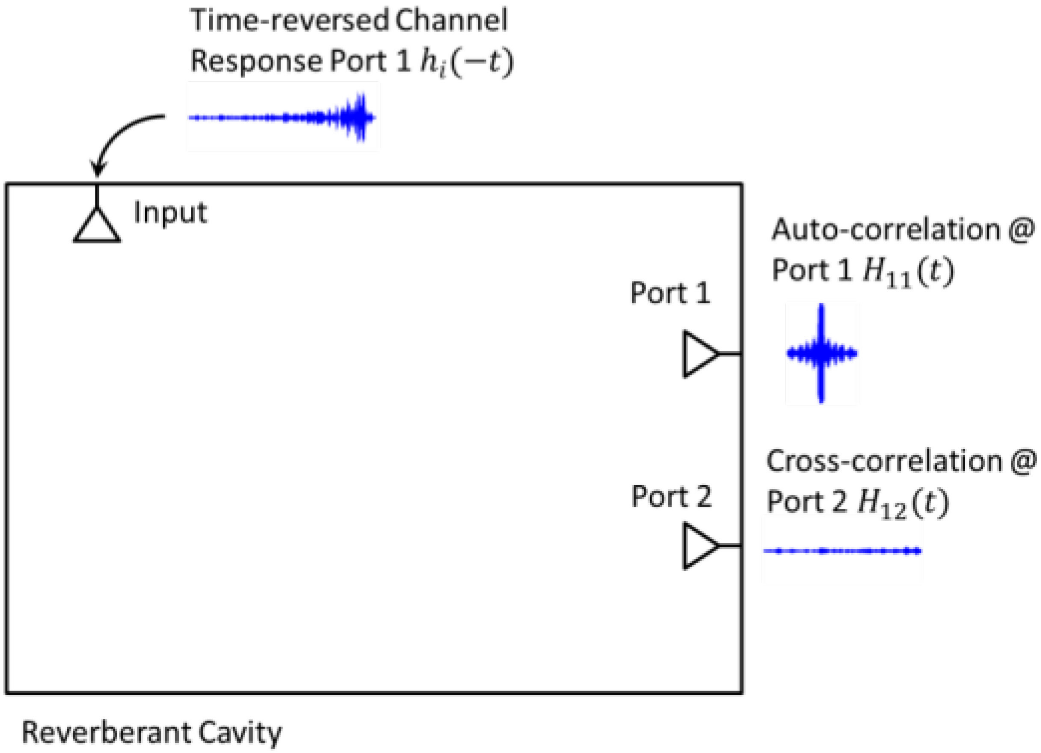

Figure 5.2- Illustration showing time-reversal process inside a reverberant cavity.

To illustrate the use of this technique for TTD beamforming consider the reverberant cavity shown in Fig. 5.2. This cavity consists a single input channel and multiple output channels. The channel response between this input channel and ith outputs can be represented by the time-domain channel response $h_i(t)$. Therefore by time-reversing this channel response and retransmitting it from the input an autocorrelated pulse can be formed at the ith output $H_{ii}(t) = h_i(t) * h_i(-t)$. Furthermore by applying a time-delay τ this autocorrelated pulse can be delayed in time and when summed at the input with appropriately delayed and time-reversed channel responses from the other channels in the cavity, short pulses can be formed at each of the output ports of the cavity in succession yielding a transmitted wavefront propagating at an angle θ. However due to the nature of the reverberant cavity the ith channel response does not exclusively couple to the ith channel but rather couples to all of the channels in the cavity. Therefore the total signal transmitted from the ith channel in the cavity can be written as the sum of autocorrelated $H_{ii}(t,\tau_i)$ and cross-correlated $H_{ij}(t,\tau_j)$ terms,

$$y_i(t) = H_{ii}(t,\tau_i) + \sum_{\substack{j=1 \\ j\neq i}}^{K} H_{ij}(t,\tau_j) \tag{5.5}$$

where $H_{ii}(t,\tau_i) = h_i(t) * h_i(-t-\tau_i)$ and $H_{ij}(t,\tau_i) = h_i(t) * h_j(-t-\tau_j)$. Assuming the cavity is sufficiently reverberant the second term in Eq. 5.5 is generally much lower in amplitude than the autocorrelation peak. However achieving such highly reverberant cavities generally requires increased volume which is often undesirable for many applications. Furthermore any source of loss inside the cavity can degrade the quality of the autocorrelation adding noise to the first term in Eq. 5.5 even in the absence of cross-correlation terms. Therefore in the proceeding sections of this chapter, a simple and compact self-biasing switch is proposed to reduce such artifacts and improve the quality of time-reversal based beamforming systems.

Design of a Broadband Self-Biasing Switch

Previous demonstrations have shown that passive UWB beamforming from a single input can be achieved using time reversal [67, 68, 69]. This technique employs a reverberant cavity to act as a passive delay line between a single input and multiple output ports. Due to the loss mechanisms inside this cavity, artifacts are generated by the time reversal process known as time sidelobes which degrade the beamforming. These artifacts appear as random low amplitude signals before and after the desired output pulse. By loading the output ports of a reverberant cavity with broadband self-biasing switches a significant reduction in these time sidelobes can be realized [71]. Each switch consists of a 50-Ω microstrip printed on RO4003 containing multiple Schottky diodes in series (Fig. 5.3). Due to the capacitance of this diode combination, these devices act like high pass filters for low voltage signals, strongly reflecting low power transients below the cutoff frequency. For transients exceeding the activation voltage of the diodes, this capacitance is shorted allowing signals to pass with significantly less attenuation. This effect creates a nonlinear channel response at the output of the cavity that suppresses low voltage signals, while passing high voltage signals with less attenuation.

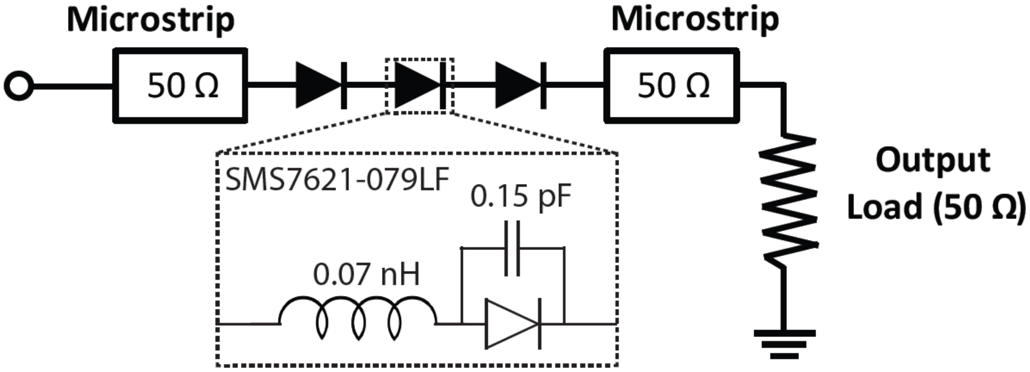

Figure 5.3- Equivalent circuit diagram of the self-biasing switch used in the time reversal beamforming process. The equivalent circuit of the SMS7621-079LF Schottky diodes used in the switch is shown in the inset.

Transient simulations of these devices were performed in Agilent's Advanced Design System (ADS). Each switch consists of three SMS7621-079LF Schottky diodes mounted in series on a 50-Ω microstrip line and oriented cathode to anode (Fig. 5.3). At low power each of these diodes possesses a total capacitance of 0.25 pF and a package inductance of 0.7 nH. This inductance and capacitance creates a pass band near 12 GHz.

By adjusting the number of elements in the switch the rolloff of this feature can be increased, widening the bandwidth of the reject band. Thus to create a high pass filter with a 3-dB rolloff above 8 GHz, three diodes were placed in series in the switch. Above the activation voltage, this 0.08 pF of capacitance is shorted out, rendering the impedance of the device primarily resistive with each diode possessing around 12 Ω of series resistance. At high power the combined resistance of these three devices as well as the characteristic impedance of the microstrip causes this device to act like a voltage divider. The amount of attenuation generated in the high power state can be reduced by decreasing the number of diodes in this device. Since the primary source of capacitance in the SMS7621-079LF diode is the SC79 package, a smaller number of unpackaged diodes could be used thus also reducing the attenuation in the high power state.

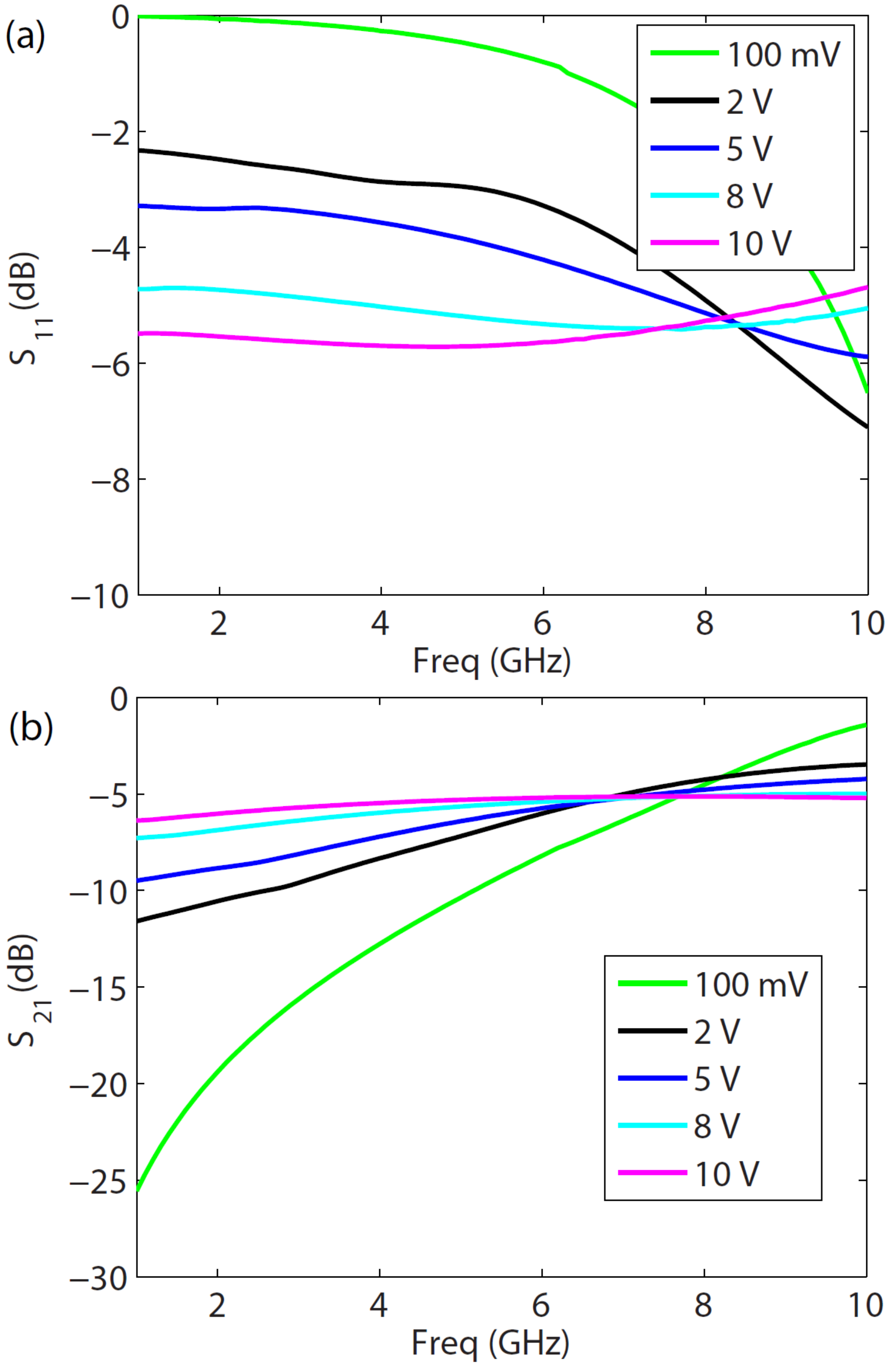

Figure 5.4- Simulated (a) S11 and (b) S21 for the self-biasing switch at various input voltage levels.

Voltage dependent reflection and transmission coefficients for this device were obtained in Agilent's Advanced Design System (ADS) through a series of transient simulations. Equivalent circuits for the diodes were generated from the manufacturer's specification sheet [55]. Each of these simulations monitored reflected and transmitted signals relative to a narrowband input at various voltage levels. Over the frequency range of interest (2-8 GHz) an average increase in transmission of 5.47 dB is observed between 100 mV and 10 V with a maximum increase of 13.3 dB at 2 GHz (Fig. 5.4). By correctly adjusting the amplitude of the input signal to the cavity, this difference in transmission between high and low voltages signals can be used to reshape the outputs of the cavity, preferentially passing signals which are focused at the output ports while rejecting those which are not. Due to the finite series resistance of the diodes there is a significant attenuation through the SBS at high power. While this attenuation will decrease the peak amplitude of the output signals, the reduction of the temporal artifacts or time sidelobes created by the TR process can be large enough to result in a net improvement in signal quality.

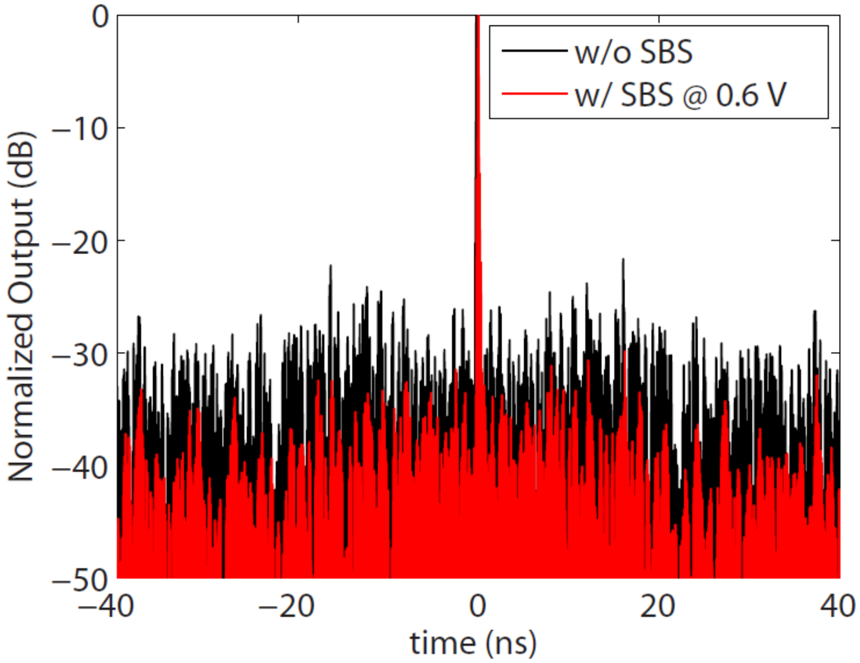

Figure 5.6- Simulated output of reverberant transmission line network with (red) and without (black) self-biasing switch.

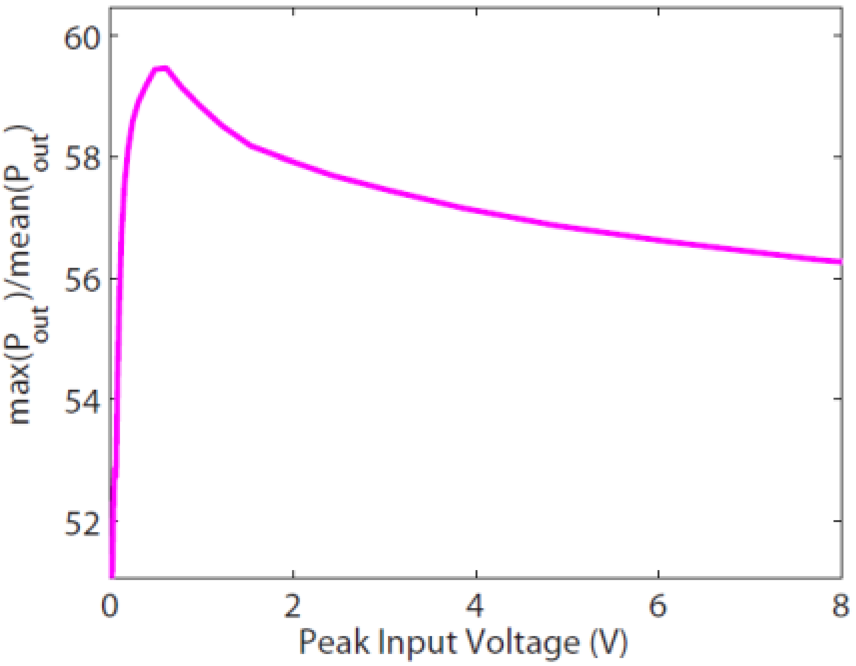

Figure 5.5- Peak to average ratio of output signal after SBS for various peak input voltages. The maximum peak to average ratio occurs around 0.6 V.

To determine the effect of these self-biasing switches on the time reversal process a reverberant two-port network was modeled using 25 parallel transmission lines [71]. Each transmission line had a characteristic impedance of 377 Ω and a length between from 1.2 m to 2.4 m. Using a 166-ps Gaussian modulated RF pulse, the impulse response of this network was measured, time-reversed and used as an input waveform in a second simulation. Comparing the normalized output of this network with and without the self-biasing switch, a reduction of approximately 6 dB in the time sidelobes was observed (Fig. 5.5). These artifacts can be further reduced by incorporating more series diodes into the switch but at a cost of increased attenuation. Furthermore, because the diodes in the switch are all oriented in the same direction the focused pulse is rectified creating a monopolar pulse. For applications which require a bipolar pulse an antiparallel diode pair can be used instead.

The impact of the SBS can be optimized for a particular configuration by adjusting the input power to the reverberant system and monitoring the peak to average ratio of the output (Fig. 5.6). In the case of a single UWB pulse generated by the time reversal process, the peak to average ratio of the signal will be highest when the artifacts surrounding this pulse are minimized. At voltages well below the activation voltage of the diodes, both the reconstructed pulse and the time-sidelobes experience large and equal attenuation, thus no appreciable improvement in the peak to average ratio occurs. As the input voltage increases, the peak voltage in the output experiences increasingly less attenuation than the sidelobes, thus increasing the difference between these two features and improving signal quality. Increasing the input voltage beyond this point will degrade signal quality by pushing components of the time-sidelobes above the activation voltage of the diodes.

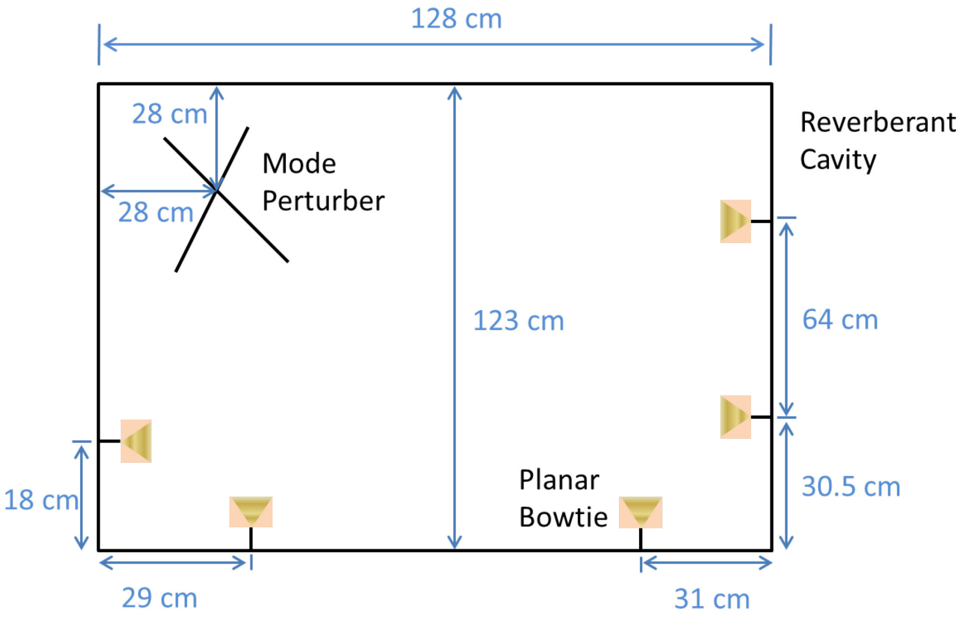

Figure 5.7- Schematic illustration of reverberating cavity used in beamforming experiments. The height of the cavity was 66 cm.

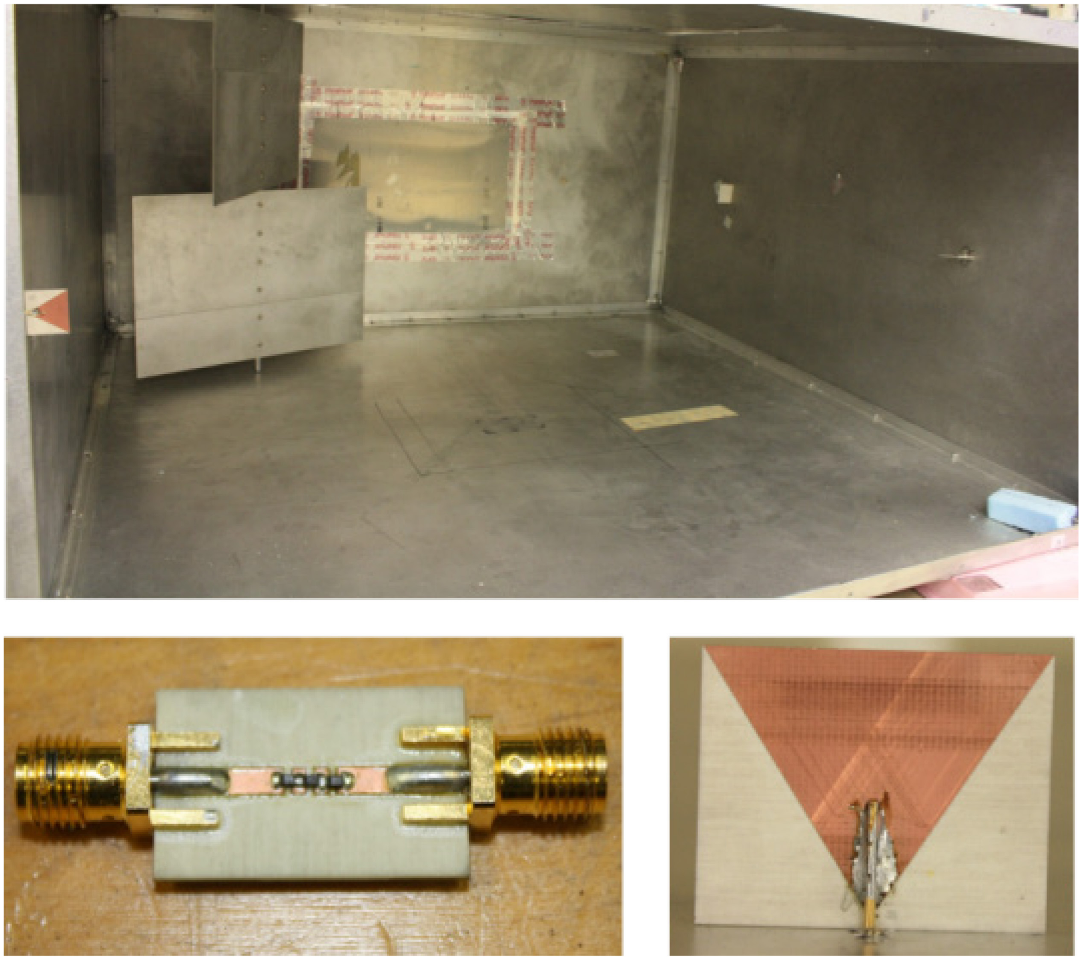

Figure 5.8- (Top) Photograph showing inside of reverberating cavity used in beamforming experiments. Photograph of self-biasing switch (bottom-left) and planar bowtie antenna (bottom-right).

Beaforming Demonstration

To demonstrate the utility of these self-biasing switches for the time reversal based beam forming process, experiments were performed in a 1.27 m x 1.22 m x 0.6 m aluminum box (Fig. 5.7). This cavity was loaded with five planar bowtie antennas four of which were designated as output ports and loaded with self-biasing switches (Fig. 5.8). Using a process similar to that first proposed by Carsenat et. al [67], the impulse response between each unloaded output port and the input was measured from 1-10 GHz using an Agilent N5230A vector network analyzer and then filtered from 2-8 GHz with a Gaussian window, yielding a 166-ps Gaussian pulsed RF signal in the time domain. Each signal was then phase conjugated and inverse Fourier transformed to generate the time-reversed impulse response for each channel.

Using a 25-GS/s Tektronix 70002 arbitrary waveform generator connected to a 40-dBm amplifier, the sum of the impulse responses of the cavity were fed into the input port and the resulting signals were measured at the four output ports using a Tektronix DPO70604 25-GS/s oscilloscope. These measurements were performed with and without the self-biasing switches to observe the improvement in the output pulse generated by these devices. Figure 5.9 shows the measured signal at one of the output ports with and without the self-biasing switch. A significant reduction of 10-15 dB in artifacts surrounding the main pulse can be observed between these two cases. This level of sidelobe suppression was larger than that observed in the simulation shown in Fig. 5.5, for two primary reasons. First the capacitance and inductance of the Schottky diodes has some inherent frequency dependence which causes the low power state of the switch to exhibit slightly broader bandwidth than predicted from the manufacturer's specified values. Second the reverberation environment in the experiment and simulation were different creating different sidelobe levels at the input of the switch.

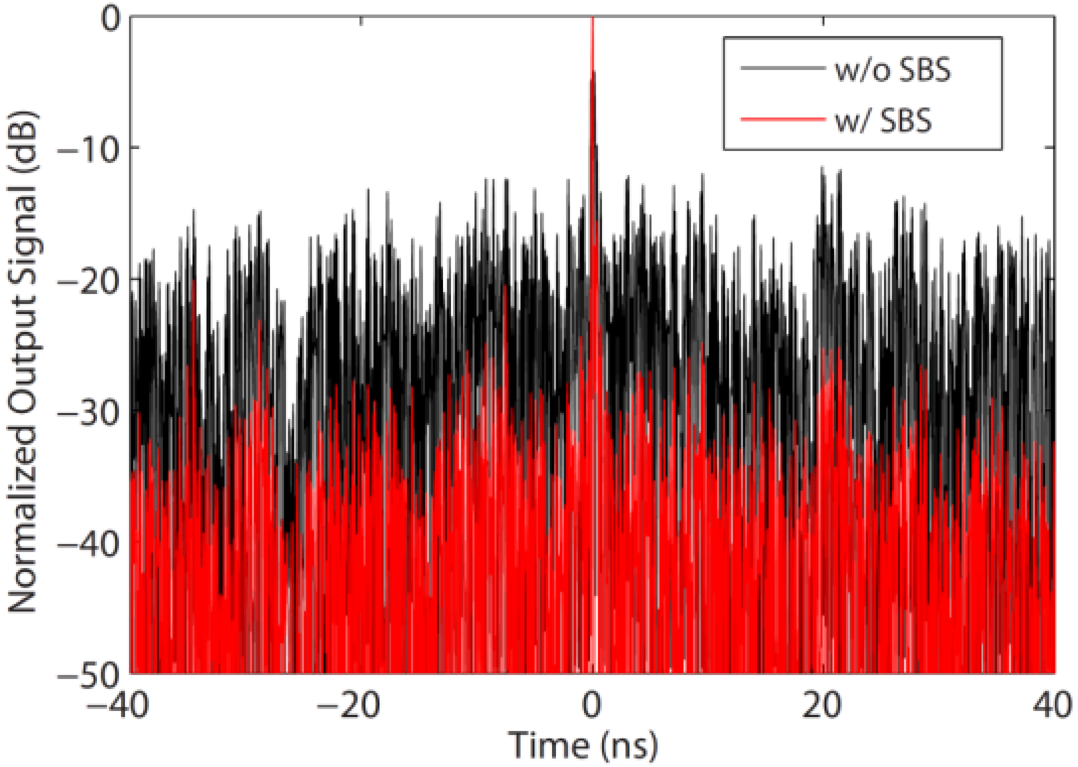

Figure 5.9- Measured output of reverberant cavity with (red) and without (black) self-biasing switches (SBS).

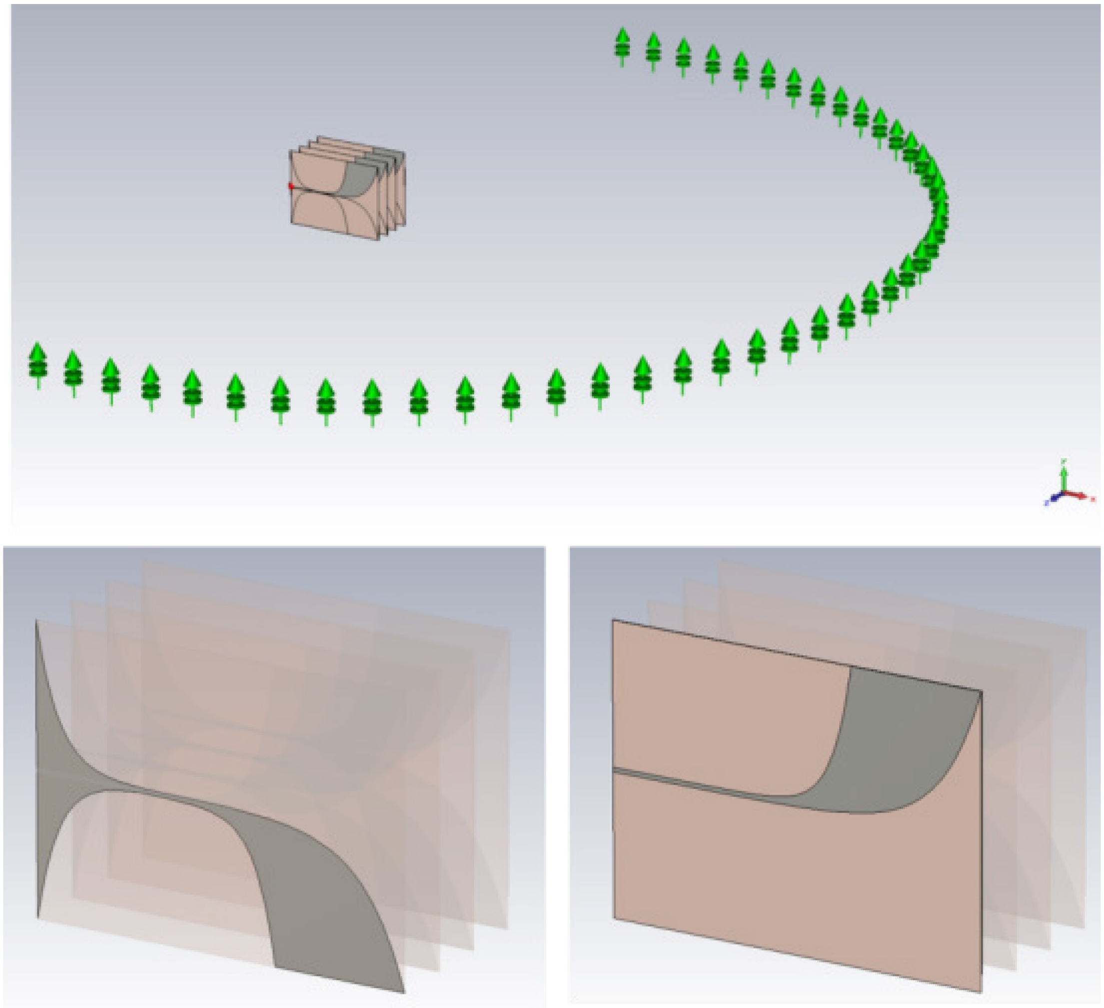

Figure 5.10- Screenshot in CST showing configuration of antenna array used in beamforming simulation and arrangement of far-field probes (top). The front (bottom-right) and back (bottom-left) of a single planar Vivaldi element are also shown.

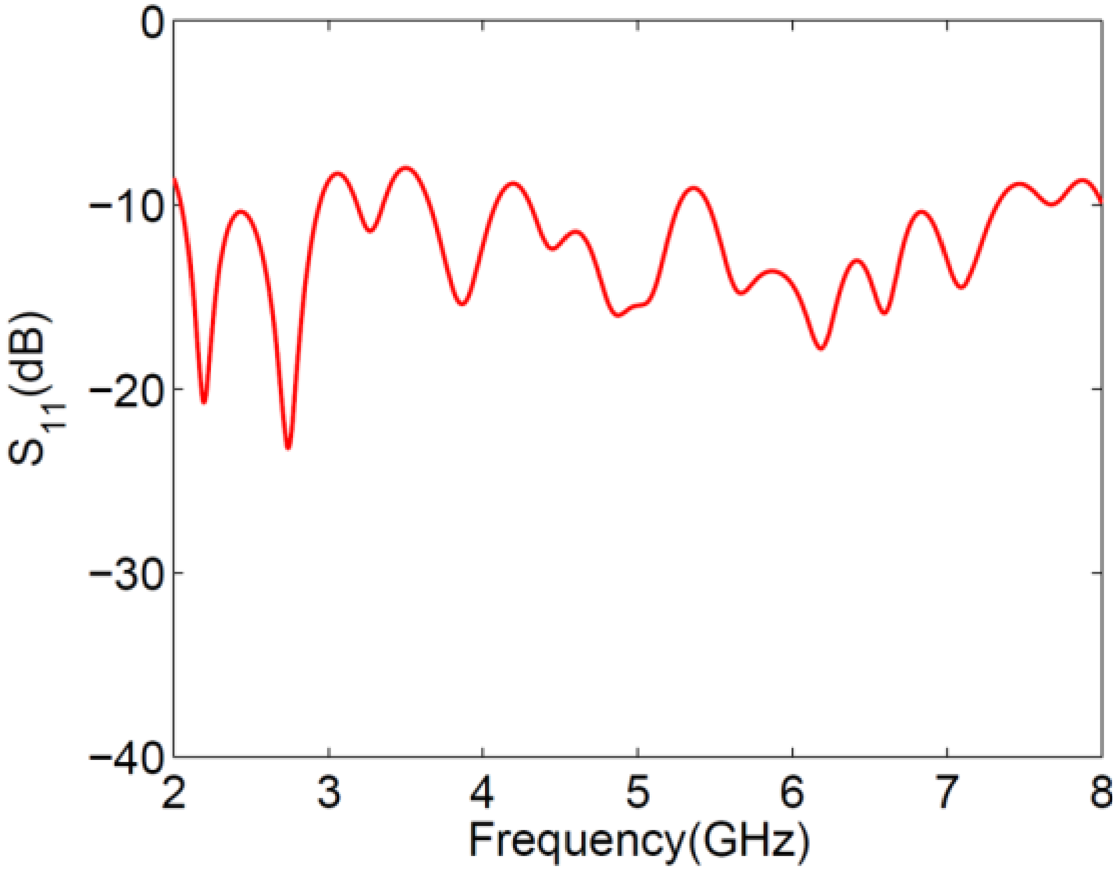

Figure 5.11- Simulated S_{11} of a single Vivaldi element in the four element array configuration shown in Fig. 5.10. In general the reflected power is less than -10 dB over the 2-8 GHz band of interest.

To investigate the effect of these devices on the beamforming process, signals measured from the output ports of the cavity, both with and without the self-biasing switches, were used as inputs to a four element array simulated in CST Microwave Studio. Each of these signals was normalized in amplitude to its respective maximum. This array consisted of four Vivaldi antennas covering the 2-8 GHz band of interest. In general the reflected power at the input of these elements was less than -10 dB over the 2-8 GHz band of interest (Fig. 5.11). The time-domain far-fields of this array were computed at 45 discrete angles. Due to the temporal sidelobes generated during the time reversal process, considerable artifacts are created in the beamforming process. This effect is evident in comparing the resulting pattern from the Vivaldi array fed directly with four separate 6-GHz Gaussian pulses (Fig 5.12) and the pattern generated using the measured data from the cavity (Fig 5.13). Using the self-biasing switches (Fig 5.14) a significant reduction in these artifacts (~10 dB) is observed in the range profile of the resulting pattern, although due to the loss present in the switch the effective gain of the array is reduced by 6 dB. Furthermore, because the diodes in the SBS rectify the output of the cavity, the resulting waveform at each element of the array is much closer to a monopolar pulse. This creates additional features in azimuth which appear as diagonal arcs in Figure 5.14. This effect can also be seen in Figure 5.15, where an 88-ps Gaussian monopulse is input into the array. In the case of the self-biasing switch, these features can be mitigated by using an anti-parallel diode combination which responds equally to the positive and negative portions of the pulse.

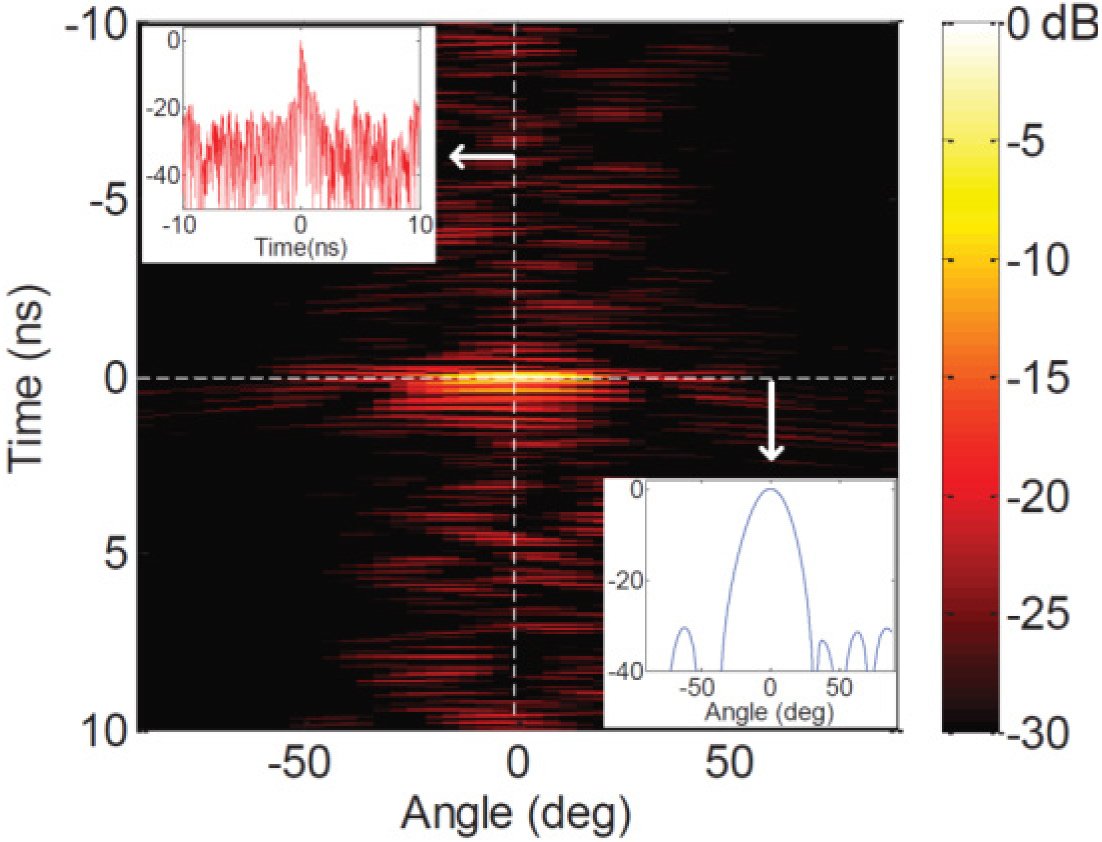

Figure 5.13- Simulated beamforming from a four element Vivaldi array, computed using measured output of the reverberant cavity without SBS. The inset in each figure shows the cut plane at 0 ns (top-left) and 0° (bottom-right).

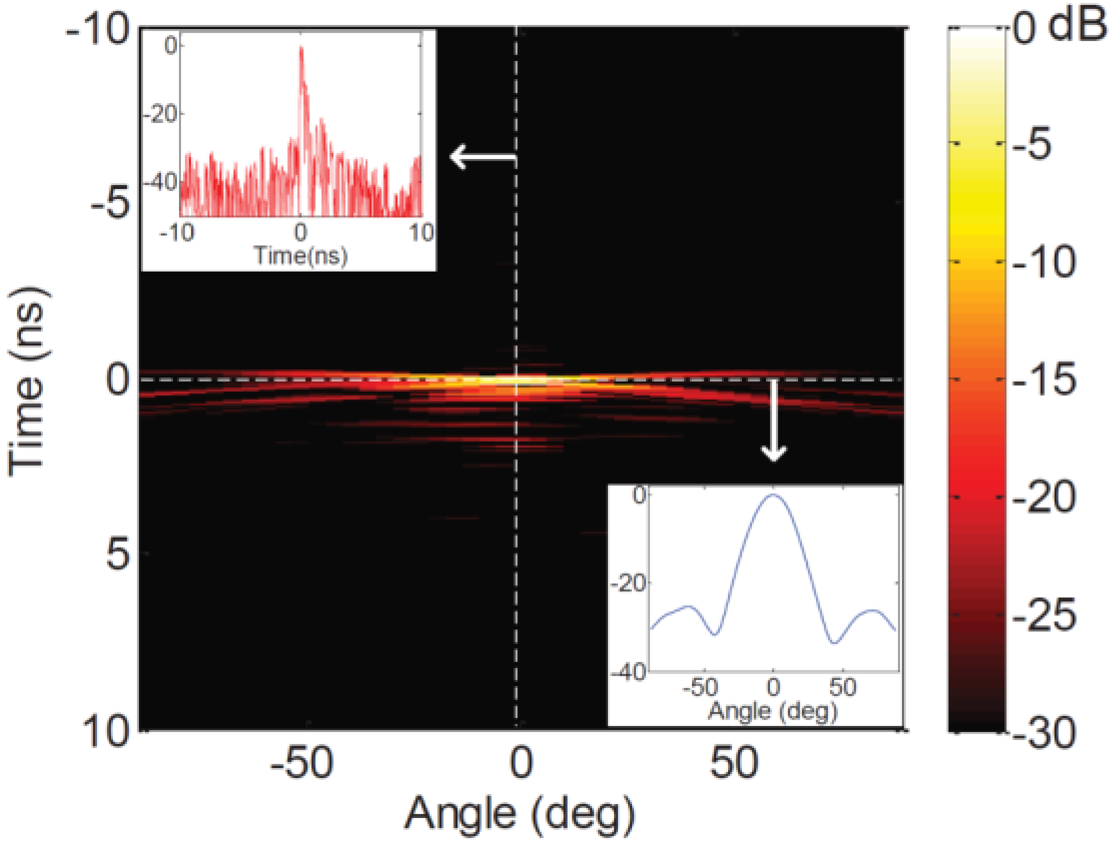

Figure 5.14- Simulated beamforming from a four element Vivaldi array, computed using measured output of the reverberant cavity with SBS. The inset in each figure shows the cut plane at 0 ns (top-left) and 0° (bottom-right).

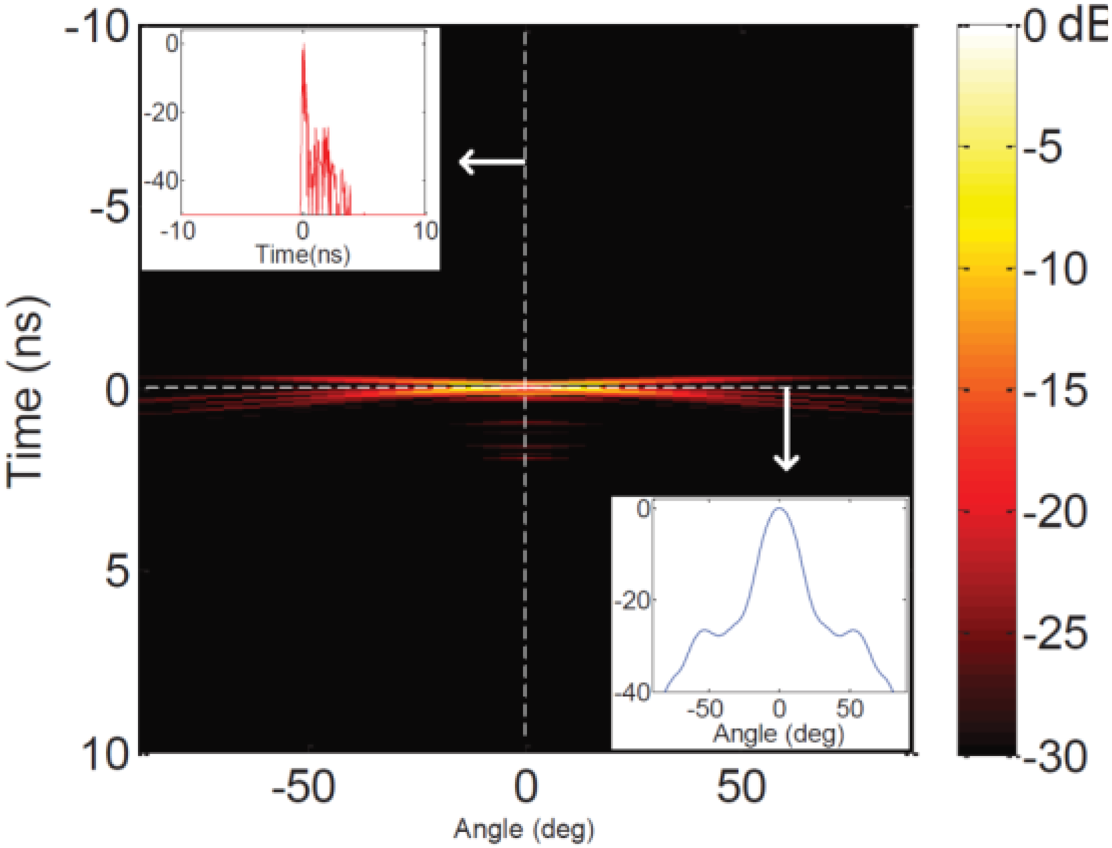

Figure 5.15- Simulated beamforming from a four element Vivaldi array, computed using 88-ps monopolar Gaussian pulse. The inset in each figure shows the cut plane at 0 ns (top-left) and 0° (bottom-right).

Chapter 6 –Conclusions

Summary of Achievements

The focus of this dissertation has been the development of distributed broadband self-biasing structures for microwave applications. Such devices interact with electromagnetic waves differently depending on the power in the incident wave, and in doing so allow nonlinear functions typically performed in a single transmission line to be performed in free-space or among multiple transmission lines. Because the power density in the free space wave is typically lower than that of the fields contained in a transmission line, low power yet faster and more broadband devices can be employed in these structures. This functionality is particularly useful for applications in high power limiting and field confinement. Furthermore these structures can be used to improve the fidelity of complex UWB beamformers by suppressing low amplitude noise, without additional processing.

In the second chapter of this dissertation a broadband switching metamaterial concept was introduced. Using a hybrid thin wire and split ring resonator unit cell it was shown that non-overlapping regions of negative permittivity and permeability could be generated creating a broadband imaginary index. Due to the imaginary propagation constant present in this medium, incident waves are unable to propagate inside the medium creating large reflection coefficients even for electrically thin slabs. It was then shown that by shorting the gaps or capacitive elements of the split ring resonators that this broadband reflection could be reduced allowing the structure to be well impedance matched. By adjusting the length of this structure, such that a quarter wave or Fabry-Perot resonance, was created close in frequency to the impedance matched frequency, broadband transmissive characteristics could be generated between these two features. Therefore by introducing a suitable diode into the gaps of the split ring resonators it was proposed that this structure could be transitioned from a broadband reflective state at low incident power to a broadband transparent state at high power. Simulations performed in Ansoft's HFSS were used to demonstrate this concept.

Due to the presence of a nonlinear impedance in the magnetic elements of this structure, evaluation of transient behavior requires modeling both the coupling between the structure and the incident free space wave as well as the nonlinear impedance of the diodes. Therefore a multiconductor transmission line analysis was developed to model the transient behavior of this structure for various nonlinear loads. First a two-conductor transmission line model was proposed and used to investigate the transient switching behavior of this structure for symmetric nonlinearities such as the dual anti-parallel Schottky diode combination. For this particular diode it was shown that the response time of the structure was primarily limited by the inherent frequency characteristics of the metamaterial and not by the transient time of the diode. Following this analysis a four-conductor transmission line model was proposed to model non-symmetric nonlinearities such as single diodes. Using this model the transient behavior of this structure was investigated for the case where the top and bottom gaps of the magnetic elements were loaded with opposing varactor diodes. For this configuration, this structure was observed to exhibit the opposite response to incident power, creating broadband transmissive characteristics at low power and broadband reflective characteristics at high power.

Furthermore it was observed that the range in power over which this device switched states was considerably shorter, although the response time was seen to be considerably longer due to the fact that the switching mechanism relies on an accumulation of DC bias across the diodes in the top and bottom of the ring.

Experimental demonstrations of both the Schottky and varactor loaded broadband switching metamaterials were performed in WR-284 waveguide. The former of these structures demonstrated a 10 dB reduction in reflected amplitude over an 18% bandwidth, a 3 dB reduction over a >30% bandwidth, and a maximum difference in reflection of nearly 42 dB. Furthermore based on transient measurements also performed in rectangular waveguide, it was observed that the response time of this structure was approximately 3-4 ns which was in good agreement with values predicted in the multiconductor transmission line analysis. Transient measurements of the varactor loaded broadband switching metamaterial were also performed in rectangular waveguide and showed similar behavior as that predicted in the multiconductor transmission line analysis. As expected this structure exhibited the opposite response to incident power, exhibiting broadband transmissive characteristics at low incident powers and broadband reflective characteristics at high incident powers. Furthermore it was observed that the power tuning range of this structure was significantly more abrupt than the Schottky loaded structure occurring over a less than 3 dB range, although the response time was observed to be significantly longer on the order of several hundred nanoseconds.

In the final chapter of this dissertation a broadband self-biasing switch was proposed to reduce the artifacts associated with time reversal based beamforming. This device consists of multiple diodes placed in series on a 50-Ω microstrip. At low incident voltages this device behaves like a high pass filter, rejecting low power transients over a broad bandwidth. Once the activation voltage of these diodes is exceeded, the capacitive elements of this filter are shorted allowing energy to pass with significantly less attenuation. By preferentially attenuating low power transients this device can suppress the temporal artifacts associated with the time reversal process. An experimental demonstration of this device was performed using a reverberant cavity as a passive delay line network. Measured outputs from this cavity were then used as inputs to a simulated array of Vivaldi antennas to demonstrate the proposed improvement in beamforming. From these measurements a 10-15 dB reduction in artifacts associated with the time-reversal process were observed.

Future Work

In this thesis broadband self-biasing structures have been discussed for various microwave applications. While these demonstrations showcase the capability of these devices to improve upon specific microwave techniques, these devices have the potential to improve a wide array of existing technology.

The broadband switching metamaterial structures discussed in Chapters 2, 3, & 4, were primarily designed to operate at the S-band frequency range, however many applications in wireless communications and radar demand devices which operate at significantly higher frequences. In principle this transition to higher frequencies is easily achieved by scaling the unit cell however the nonlinearities loading the structure possess properties which do not scale with the geometry. The Schottky diodes used in the experiment shown in Chapter 5 possess a transient time on the order of 10 ps, suggesting that the junction should be able to efficiently operate well into the mm-wave region. However the capacitance and inductance of these elements are generally not suited for operation much above S-band in the proposed structure. Therefore in order to achieve similar performance at higher frequencies diodes significantly lower junction capacitance and package parasitics should be utilized.

For many applications the orientation of an incident wave is unknown or may vary and therefore electromagnetic structures intended to interact with this wave must be able to respond equally to any orientation. For the broadband switching metamaterial structures discussed in this thesis, this concept is also true, however achieving full isotropy with this structure presents several unique challenges. Isotropic designs for similar traveling wave metamaterial structures were previously demonstrated by Rudolph et. al. [72]. These designs replace inductive elements with vias and thin wires allowing a 2-dimensionally isotropic version of the previously discussed structure to be realized. Future work should explore the use of such isotropic designs with the broadband switching metamaterials discussed in this dissertation.

In Chapter 3 it was observed that when loaded with opposing varactor diodes that the broadband switching metamaterial structure transitioned from its low power to high power state in response to an accumulated DC bias between the diodes and not to the instantaneous current induced in the ring. Due to the high resistance of these diodes in reverse bias this DC voltage persists in the rings for a long period of time after the incident radiation has been turned off [49]. This residual bias causes the structure to maintain its high power material properties for a long period of time after the incident radiation has ceased creating a sort of "memory" in the structure. By introducing an additional switching element in the unit cell which connects the vertical inductor in the magnetic element to the electric elements this residual bias can potentially be shorted in response to some stimuli. In this way the material properties of this structure can be "programmed" allowing a single bit of logic to be stored and then erased. In the future with higher levels of integration it is conceivable that more complex logic could be programmed into such structures allowing the material properties to be remotely specified at will.

In Chapter 5 a broadband self-biasing switch was proposed to reduce artifacts associated with the time-reversal based beamforming process. These switches consisted of multiple Schottky diodes placed in series on microstrips. While this techniques was effective, it is currently limited to applications where the output of a reverberant cavity is to be terminated with a transmission line. Recently, it has been demonstrated that similar time-reversal based beamforming can be achieved using a reverberating cavity with several apertures cut into the sidewall of the cavity [69]. These apertures replace the antennas used in the demonstration in Chapter 5, but prevent the use of the self-biasing switches. One potential way to reduce the time-sidelobes in this beamforming configuration, is to load the apertures at the output of the cavity with broadband switching metamaterials. At low power these structures would block leakage exiting the cavity but become transparent once the autocorrelation pulse formed at the output, thus suppressing the time-sidelobes.

List of Publications

Journal Articles

W. S. Wall, S. M. Rudolph, S. K. Hong and K. L. Morgan, "Broadband Switching Nonlinear Metamaterial," IEEE Antenna and Wireless Propagation Letters, vol. 13, pp. 427-430, 2014.

W. S. Wall and S. K. Hong, "Improved Time-Reversal Based Beamforming Using a Self-Biasing Switch" IEEE Antenna and Wireless Propagation Letters, vol. 13, pp. 1337-1340, 2014

W. S. Wall and S. M. Rudolph, " Nonlinear Multiconductor Transmission Line Analysis of Broadband Switching Metamaterials" IEEE Transactions on Antennas and Propragation, *In Preparation,* 2014.

S. K. Hong, V. M. Mendez, W. S. Wall and R. Liao, "Single-Feed Beam-Steering of Short Pulses," IEEE Antennas and Wireless Propagation Letters, vol. 13, 2014.

Conference Proceedings

W. S. Wall, S. K. Hong, S. M. Rudolph, K. M. Morgan, V. M. Mendez, and T. D. Andreadis, "Nonlinear Metamaterials for Protection of High Gain Receivers" 2013 DEPS Directed Energy Systems Symposium, Monterey CA, 2013.

W. S. Wall, S. K. Hong, S. M. Rudolph, K. L. Morgan, T. D. Andreadis, and T. Warren "Experimental Results of a Broadband Nonlinear Metamaterial for Counter HPM Applications" 2014 DEPS Directed Energy Symposium, Huntsville AL, 2014.

S. M. Rudolph, W. S. Wall, S. K. Hong, and K. L. Morgan, "Broadband Switching Nonlinear Metamaterial" 2014 IEEE Symposium on Antennas and Propagation, Memphis TN, 2014.

Other Publications

W. S. Wall, S. M. Rudolph, S. K. Hong, K. L. Morgan, and V. M. Mendez "Broadband Nonlinear Metamaterial," 2014 NRL Review.

Patents

S. M. Rudolph, W. S. Wall, and S. K. Hong "Broadband Nonlinear Reflector" *Provisional Patent Filed.*

Bibliography

[1] D. M. Pozar, Microwave Engineering 3rd Ed., John Wiley & Sons Inc., 2005.

[2] T. S. Rappaport, Wireless Communications, Principles and Practice, 2nd Ed., Prentice-Hall Inc., 2002.

[3] J. L. Prince and J. M. Links, Medical Imaging Signals and Systems, Pearson Prentice Hall, 2006.

[4] A. J. Fenn, Breast Cancer Treatment by Focused Microwave Thermotherapy, Sudbury, MA: Jones and Barlett Publishers, 2007.

[5] M. L. Skolnik, Introduction to Radar Systems, 3rd Ed., New York: McGraw-Hill Companies, 2001.

[6] D. Doody, Deep Space Craft, An Overview of Interplanetary Flight, Chichester, UK: Praxis Publishing Ltd, 2009.

[7] B. A. Campbell, Radar Remote Sensing of Planetary Surfaces, Cambridge, UK: Cambridge University Press, 2002.

[8] B. F. Burke and F. Graham-Smith, An Introduction to Radio Astronomy 3rd Ed., Cambridge, UK: Cambridge University Press, 2010.

[9] R. W. Chabay and B. A. Sherwood, Matter and Interactions, 3rd Ed., John Wiley & Sons Inc., 2011.

[10] A. V. Vorst, A. Rosen and Y. Kotsuka, RF/Microwave Interaction with Biological Tissues, John Wiley & Sons, Inc., 2006.

[11] A. V. Vorst, Electromagnetisme. Champs et Circuits, Brussels: De Boeck, 1994.

[12] L. Rayleigh, "On the Influence of Obstacles Arranged in Rectangular Order Upon the Properties of a Medium," *Philosophical Magazine Series 5,* vol. 34, no. 211, 1892.

[13] W. E. Kock, *Bell System Technical Journal,* vol. 27, no. 58, 1948.

[14] F. Capolino, Theory and Phenomena of Metamaterials, Boca Raton, FL: CRC Press, 2009.

[15] L. Solymar and E. Shamonina, Waves in Metamaterials, Oxford University Press, 2009.

[16] D. R. Smith, W. J. Padilla, D. C. Vier, S. C. Nemat-Nasser and S. Schultz, "Composite Medium with Simultaneously Negative Permeability and Permittivity," *Physical Review Letters,* vol. 84, no. 18, pp. 4184-4187, 2000.

[17] J. B. Pendry, A. J. Holden, D. J. Robbins and W. J. Stewart, "Magnetism from Conductors and Enhanced Nonlinear Phenomena," *IEEE Transactions on Microwave Theory and Techniques,* vol. 47, no. 11, pp. 2075-2084, 1999.

[18] Y. Liu and X. Zhang, "Metamaterials: a New Frontier of Science and Technology," *Chem. Soc. Rev.,* vol. 40, pp. 2494-2507, 2011.

[19] V. G. Veselago, "The Electrodynamics of Substances with Simultaneously Negative Values of Epsilon and Mu," *Soviet Physics,* vol. 10, no. 4, pp. 509-514, 1968.

[20] J. B. Pendry, "Negative Refraction Makes a Perfect Lens," *Physical Review Letters,* vol. 85, no. 18, pp. 3966-3969, 2000.

[21] F. Capolino, Applications of Metamaterials, Boca Raton, Fl: CRC Press, 2009.

[22] X. Zhang and Z. Liu, "Superlenses to Overcome the Diffraction Limit," *Nature Materials,* vol. 7, pp. 435-441, 2008.

[23] H. Chen, C. T. Chan and P. Sheng, "Transformation Optics and Metamaterials," *Nature Materials,* vol. 9, pp. 387-396, 2010.

[24] W. Withayachumnankul and D. Abbot, "Metamaterials in the Terahertz Regime," *IEEE Photonics Journal,* vol. 1, no. 2, pp. 99-118, 2009.

[25] M. Iwanaga, "Photonic Metamaterials: A New Class of Materials for Manipulating Light Waves," *Science and Technology of Advanced Materials,* vol. 13, no. 5, pp. 1-17, 2012.

[26] R. V. Craster and S. Guenneau, Acoustic Metamaterials: Negative Refraction, Imaging, Lensing and Cloaking, Springer Science+Business Media Dordrecht, 2013.

[27] J. P. Turpin, J. A. Bossard, K. L. Morgan, D. H. Werner and P. L. Werner, "Reconfigurable and Tunable Metamaterials: A Review of the Theory and Applications," *International Journal of Antennas and Propagation,* 2014.

[28] M. Gil, C. Damm, A. Giere, M. Sazegar, J. Bonache, R. Jakoby and F. Martin, "Electrically

tunable split-ring resonators at microwave frequencies based on barium-strontium-titanate thick films," *Electronics letters ,* vol. 45, no. 8, pp. 417-418, 2009.

[29] Q. Zhao, L. Kang, B. Du, B. Li, J. Zhou, H. Tang, X. Liang and B. Zhang, "Electrically Tunabel Negative Permeability Metamaterials Based on Nematic Liquid Crystals," *Applied Physics Letters,* vol. 90, no. 1, 2007.

[30] P. E. Sieber and D. H. Werner, "Reconfigurable broadband infrared circularly polarizing reflectors based on phase changing birefringent metasurfaces," *Optics Express,* vol. 21, no. 1, pp. 1087-1100, 2013.

[31] L. Kang, Q. Zhao, H. Zhao and J. Zhou, "Magnetically tunable negative permeability metamaterial composed by split ring resonators and ferrite rods," *Optics Express,* vol. 16, no. 12, pp. 8825-8834, 2008.

[32] C. Hou-Tong, W. J. Padilla, J. M. Zide, A. C. Gossard, A. J. Taylor and R. D. Averitt, "Active Terahertz Metamaterial Devices," *Nature,* vol. 444, no. 7119, pp. 597-600, 2006.

[33] T. Hand and S. Cummer , "Characterization of tunable metamaterial elements using MEMS switches," *Antenna and Wireless Propagation Letters,* vol. 6, pp. 401-404, 2007.

[34] J.-Y. Ou, E. Plum, J. Zhang and N. I. Zheludev, "An electromechanically reconfigurable plasmonic metamaterial operating in the near-infrared," *Nature Nanotechnology,* vol. 8, no. 4, pp. 252-255, 2013.

[35] A. B. Golovin and O. D. Lavrentovich, "Electrically reconfigurable optical metamaterial based on colloidal dispersion of metal nanorods in dielectric fluid," *Applied Physics Letters,* vol. 95, no. 25, 2009.

[36] Q. Liu, Y. Cui, D. Gardner, X. Li, S. He and I. I. Smalyukh, "Self-alignment of plasmonic gold nanorods in reconfigurable anisotropic fluids for tunable bulk metamaterial applications," *Nano Letters,* vol. 10, no. 4, pp. 1347-1353, 2010.

[37] I. V. Shadrivov, A. B. Kozyrev, D. W. van der Weide and Y. S. Kivshar, "Tunable transmission and harmonic generation in nonlinear metamaterials," *Applied Physics Letters,* vol. 93, no. 16, 2008.

[38] A. R. Katko, A. M. Hawkes, J. P. Barrett and S. A. Cummer, "Rf limiter metamaterial using pin diodes," *IEEE Antennas and Wireless Propagation Letters,* vol. 10, pp. 1571-1574, 2011.

[39] L. A. Marcos, M. J. Freire, J. M. Algarin, V. C. Behr, P. M. Jakob and R. Marques, "Nonlinear split-ring metamaterial slabs for magnetic resonance imaging," *Applied Physics Letters ,* vol. 98, no. 13, 2011.

[40] W. S. Wall, S. M. Rudolph, S. K. Hong and K. L. Morgan, "Broadband Switching Nonlinear Metamaterial," *IEEE Antenna and Wireless Propagation Letters,* vol. 13, pp. 427-430, 2014.

[41] D. F. Sievenpiper, "Nonlinear grounded metasurfaces for suppression of high-power pulsed RF currents," *IEEE Antennas and Wireless Propagation Letters,* vol. 10, pp. 1516-1519, 2011.

[42] W. Hiroki, S. Kim, J. J. Rushton and D. F. Sievenpiper, "Waveform-Dependent Absorbing Metasurfaces," *Physical Review Letters,* vol. 111, no. 24, 2013.

[43] A. R. Katko, J. P. Barrett and S. A. Cummer, "Time-varying transistor-based metamaterial for tunability, mixing, and efficient phase conjugation," *Journal of Applied Physics,* vol. 115, no. 14, 2014.

[44] C. Kurter, P. Tassin, A. P. Zhuravel, L. Zhang, T. Koschny, A. V. Ustinov, C. M. Soukoulis and S. M. Anlage, "Switching nonlinearity in a superconductor-enhanced metamaterial," *Applied Physics Letters,* vol. 100, no. 12, 2012.

[45] J.-P. Colinge and C. A. Colinge, Physics of Semiconductor Devices, Dordrecht: Kluwer Academic Publishers, 2002.

[46] S. M. Sze and K. K. NG, Physics of Semiconductor Devices, 3rd Ed., Hoboken, New Jersey: John Wiley & Sons, Inc., 2007.

[47] S. S. Inc., "Varactor Diodes: Application Note," 2008.

[48] Skyworks Solutions, Inc., "Application Note: Varactor Diodes," Skyworks Solutions, Inc., 2008.

[49] B. Wang, J. Zhou, T. Koschny and C. M. Soukoulis, "Nonlinear properties of split-ring resonators," *Optics Express,* vol. 16, no. 20, pp. 16058-16063, 2008.

[50] E. Poutrina, D. Huang and D. R. Smith, "Analysis of Nonlinear Electromagnetic Metamaterials," *New Journal of Physics,* vol. 12, no. 9, 2010.

[51] Z. Popovic and B. D. Popovic, Introductory Electromagnetics, Prentice-Hall, Inc.: Upper Saddle River, New Jersey, 2000.

[52] S. J. Orfandis, Electromagnetic Waves and Antennas, 1999.

[53] S. M. Rudolph, "Broadband, Volumetric Negative-Refractive-Index Media," University of Michigan, Ann Arbor, Ann Arbor, Michigan, 2011.

[54] S. M. Rudolph and A. Grbic, "Super-Resolution Focusing Using Volumetric Broadband NRI media," *IEEE Transactions on Antennas and Propagation,* vol. 56, pp. 2963-2969, 2008.

[55] Skyworks 2013, "Surface Mount Mixer and Detector Schottky Diodes".

[56] J. A. Brandao Faria, Multiconductor Transmission-Line Structures: Modal Analysis Techniques, New York, NY: John Wiley & Sons Inc., 1993.

[57] S. M. Rudolph and A. Grbic, "The Design of Broadband, Volumetric NRI Media Using Multiconductor Transmission-Line Analysis," *IEEE Transactions on Antennas and Propagation,* vol. 58, no. 4, pp. 1144-1154, 2000.

[58] Skyworks, Inc., "SMV123x Series: Hyperabrupt Junction Tuning Varactors," Skyworks.

[59] D. Huang, A. Rose, E. Poutrina, S. Larouche and D. R. Smith, "Wave Mixing in Nonlinear Magnetic Metacrystal," *Applied Physics Letters,* vol. 98, no. 20, p. 204102, 2011.

[60] M. Ghavami, L. B. Michael and R. Kohno, Ultra Wideband Signals and Systems in Communication Engineering, 2nd ed., Hoboken, NJ: Wiley, 2007.

[61] C. -H. Liao, P. Hsu and D. -C. Chang, "Energy Patterns of UWB Antenna Arrays with Scan Capability," *IEEE Transactions on Antennas and Propagation,* vol. 59, no. 4, pp. 1140-1147, 2011.

[62] M. A. Panduro and H. Foltz, "Energy Patterns of UWB Antenna Arrays with Low Side Lobe Level During Beam-Scanning," in *IEEE Antennas and Propagation Society International Symposium*, 2013.

[63] M. Lalande, J. C. Diot, S. Vauchamp and J. Andrieu, "An Ultra Wideband Impulse Optoelectronic Radar: RUGBI," *Progress in Electromagnetics Research B,* vol. 11, pp. 205-222, 2009.

[64] L. Wang, Y. X. Guo, Y. Lian and C. H. Heng, "3-TO-5GHz 4-channel UWB Beamforming Transmitter with 1 phase resolution through calibrated vernier delay line in 0.13um CMOS," in *2012 IEEE International Solid-State Circuits Conference Digest of Technical Papers*, 2012.

[65] J. Roderick, H. Krishnaswamy, K. Newton and H. Hashemi, "Silicon-Based Ultra-Wideband Beam-Forming," *IEEE Journal of Solid-State Circuits,* vol. 41, no. 8, pp. 1726-1739, 2006.

[66] H. Zmuda and E. N. Toughlian, Photonic Aspects of Modern Radar, Norwood, MA: Artech House, Inc, 1994.

[67] D. Carsenat and C. Decroze, "UWB Antennas Beamforming Using Passive Time-Reversal Device," *IEEE Antennas and Wireless Propagation Letters,* vol. 11, pp. 779-782, 2012.

[68] M. Davy, J. de Rosny and M. Fink, "Focusing and Amplification of Electromagnetic Waves by Time Reversal in a Leaky Reverberation Chamber," *Comptes Rendus Physique,* vol. 11,

no. 1, pp. 37-43, 2010.

[69] S. K. Hong, V. M. Mendez, W. S. Wall and R. Liao, "Single-Feed Beam-Steering of Short Pulses," *IEEE Antennas and Wireless Propagation Letters,* vol. 13, 2014.

[70] S. K. Hong, B. T. Taddese, Z. B. Drikas, S. M. Anlage and T. D. Andreadis, "Focusing an Arbitrary RF Pulse at a Distance Using Time-Reversal Techniques," *Journal of Electromagnetic Waves and Applications,* 2013.

[71] B. T. Taddese, T. M. Antonsen, E. Ott and S. M. Anlage, "Iterative Time Reversal with Tunable Convergence," *Electronics Letters,* vol. 47, no. 21, pp. 1165-1167, 2011.

[72] S. M. Rudolph, C. Pfeiffer and A. Grbic, "Design and Free-Space Measurements of Broadband, Low-Loss Negative Permeability and Negative-Index Media," *IEEE Transactions on Antennas and Propagation,* vol. 59, no. 8, pp. 2989-2997, 2011.

[73] S. M. Rudolph and A. Grbic, "Volumetric Negative-Refractive-Index Medium Exhibiting Broadband Negative Permeability," *Journal of Applied Physics,* vol. 102, 2007.

Curriculum Vitae

Walter Scott Wall was born February 11, 1988 in Baltimore Maryland to Geraldine Elaine Wall and Walter Thomas Wall. He received a B.S. in Physics from the University of Maryland Baltimore County in 2009 and a M.S.E. and Ph.D. in Electrical and Computer Engineering from The Johns Hopkins University in 2011 and 2014 respectively. Since 2007 he has worked in the Tactical Electronic Warfare Division of the US Naval Research Laboratory as an electronics engineer. From 2010 to 2012 he was a research assistant in the Ultrafast and Nonlinear Photonics group at Johns Hopkins University, where he researched four-wave mixing in microwave photonics systems. From 2009 to 2010 he was a teaching assistant in the Department of Physics and Astronomy. To date he has authored /co-authored nine peer-reviewed papers and conference proceedings. In 2012 he was awarded 2nd place in the IEEE Capital Region Student Poster Competition in Optics and Photonics.